

Measurement of the Neutral Current in the Standard Model  
Using the Tau Polarization Asymmetries  
Determined from the Decay  $\tau^- \rightarrow \rho^- \nu_\tau$

by

Myron R. Rosvick  
B.Sc., University of Alberta, 1988  
M.Sc., University of Victoria, 1990

A Dissertation Submitted in Partial Fulfillment of the  
Requirements for the Degree of

DOCTOR OF PHILOSOPHY

in the Department of Physics and Astronomy

We accept this dissertation as conforming  
to the required standard

---

Dr. R.K. Keeler, Supervisor (Department of Physics and Astronomy)

---

Dr. A. Astbury, Departmental Member (Department of Physics and Astronomy)

---

Dr. L.P. Robertson, Departmental Member (Department of Physics and Astronomy)

---

Dr. P. Wan, Outside Member (Department of Chemistry)

---

Dr. D. Harrington, Outside Member (Department of Chemistry)

---

Dr. M. Corden, External Examiner (Supercomputing Computations Research Institute,  
Florida State University)

© Myron Richard Rosvick, 1995  
University of Victoria

All rights reserved. This dissertation may not be reproduced in whole or in part, by  
photocopying or other means, without the permission of the author.

Supervisor: Dr. Richard K. Keeler

### ABSTRACT

The decay  $\tau^- \rightarrow \rho^- \nu_\tau$  is studied to examine parity violation and lepton universality in neutral currents within the Standard Model. The average tau polarization asymmetry and the forward-backward tau polarization asymmetry are measured to be

$$\begin{aligned}\langle P_\tau \rangle &= (-15.5 \pm 2.8(\text{stat}) \pm 1.4(\text{syst}))\% \\ A_{\text{FB}}^{\text{Pol}} &= (-7.6 \pm 3.3(\text{stat}) \pm 1.5(\text{syst}))\%.\end{aligned}$$

The effective coupling strengths derived from  $\langle P_\tau \rangle$  and  $A_{\text{FB}}^{\text{Pol}}$  are

$$\begin{aligned}\frac{\hat{v}_\tau}{\hat{a}_\tau} &= 0.078 \pm 0.014 \pm 0.007 \\ \frac{\hat{v}_e}{\hat{a}_e} &= 0.050 \pm 0.022 \pm 0.010\end{aligned}$$

and the ratio of these strengths is

$$R_{e\tau} \equiv \frac{(\hat{v}_e/\hat{a}_e)}{(\hat{v}_\tau/\hat{a}_\tau)} = 0.65 \pm 0.31(\text{stat}).$$

These results are consistent with the hypothesis of lepton universality and confirm parity violation in weak neutral current interactions. When evaluated under this hypothesis, the value for the effective mixing angle for leptons in the Standard Model is determined to be

$$\sin^2 \hat{\theta}_W^\ell = 0.2326 \pm 0.0031(\text{stat}) \pm 0.0015(\text{syst}),$$

in excellent agreement with other recent measurements.

Examiners:

---

Dr. R.K. Keeler, Supervisor (Department of Physics and Astronomy)

---

Dr. A. Astbury, Departmental Member (Department of Physics and Astronomy)

---

Dr. L.P. Robertson, Departmental Member (Department of Physics and Astronomy)

---

Dr. P. Wan, Outside Member (Department of Chemistry)

---

Dr. D. Harrington, Outside Member (Department of Chemistry)

---

Dr. M. Corden, External Examiner (Supercomputing Computations Research Institute, Florida State University)

# Contents

<b>Abstract</b>	<b>ii</b>
<b>Acknowledgements</b>	<b>xiv</b>
<b>1 Introduction</b>	<b>1</b>
<b>2 Theory</b>	<b>9</b>
2.1 The Standard Model and Neutral Currents . . . . .	9
2.2 Cross Section and Asymmetries . . . . .	13
2.2.1 Born Level Approximation . . . . .	13
2.2.2 Radiative Corrections . . . . .	19
2.3 Tau Polarization Measurement . . . . .	25
<b>3 The Experimental Facility</b>	<b>29</b>
3.1 The LEP Collider . . . . .	29
3.1.1 LEP Injector Chain . . . . .	29
3.1.2 LEP Main Ring . . . . .	31
3.2 The OPAL Experiment . . . . .	31
3.2.1 The Inner Tracking Chamber . . . . .	35
3.2.2 Solenoidal Magnet and Time Of Flight . . . . .	37
3.2.3 Calorimeters . . . . .	37
3.2.4 Muon Chambers . . . . .	39
3.2.5 Trigger System . . . . .	40
3.2.6 Filtering and Online Data Processing . . . . .	42

<b>4</b>	<b>Data Selection</b>	<b>43</b>
4.1	Event Samples . . . . .	43
4.1.1	OPAL Event Sample . . . . .	43
4.1.2	Monte Carlo Event Samples . . . . .	44
4.2	Tau Selection Criteria . . . . .	46
4.2.1	Final Tau Pair Sample . . . . .	50
4.3	$\tau^- \rightarrow \rho^- \nu_\tau$ Selection . . . . .	50
4.3.1	Cluster definition . . . . .	51
4.3.2	$\tau^- \rightarrow \rho^- \nu_\tau$ Selection Criteria . . . . .	51
<b>5</b>	<b>Polarization Analysis</b>	<b>56</b>
5.1	Polarization as a Function of $\cos \theta$ . . . . .	56
5.1.1	Data and Theoretical Distributions . . . . .	56
5.1.2	Corrections to the Theoretical Distributions . . . . .	58
5.1.3	Fit for Polarization in each $\cos \theta$ Bin . . . . .	64
5.2	Average Tau Polarization and Forward-Backward Tau Polarization Asymmetry . . . . .	65
5.2.1	Fit to $P_\tau$ vs. $\cos \theta$ . . . . .	65
5.2.2	Polarization and Asymmetry Results . . . . .	66
5.2.3	Additional Checks on the Fitting Method . . . . .	71
<b>6</b>	<b>Discussion</b>	<b>73</b>
6.1	Asymmetry Results . . . . .	73
6.2	The Effective Electroweak Mixing Angle . . . . .	74
<b>7</b>	<b>Conclusion</b>	<b>82</b>
<b>A</b>	<b><math>\tau^- \rightarrow h^- \pi^0 \nu_\tau</math> Branching Ratio</b>	<b>85</b>
A.1	Branching Ratio Determination . . . . .	86
A.2	Branching Ratio Results . . . . .	88
A.3	Discussion . . . . .	92

<b>B</b>	<b>Derivation of <math>\chi^2_{\cos\theta}(P_\tau)</math> Fit Parameters</b>	<b>95</b>
B.1	Derivation of Fit Function . . . . .	95
B.2	Monte Carlo Statistical Errors . . . . .	97

# List of Tables

2.1	Standard Model particles and some relevant quantum numbers. Each of the fermions has an antiparticle equivalent for which the quantum numbers have opposite sign. . . . .	10
2.2	This table shows the coupling constants, $v_f$ , $a_f$ , $c_L$ , and $c_R$ , in the weak neutral current interaction. . . . .	12
4.1	Detector and trigger status levels required for the tau selection. Appropriate levels were developed by the working groups responsible for each detector subsystem. . . . .	44
4.2	This table shows the generators used to generate the Monte Carlo event samples. . . . .	44
4.3	This table shows the branching ratios that were used as input to the Monte Carlo tau pair simulation and the current world average branching ratios. The symbol $h^-$ represents $\pi^-$ 's and $K^-$ 's. . . . .	46
4.4	This table shows the non-tau background contributions after the tau pair selection requirements are applied. . . . .	50
5.1	This table shows the values of the tau polarization as a function of the central values of the $\cos \theta$ bins. The third and fourth column present $P_\tau$ and $\chi^2_{\cos \theta}$ for the fits which include the Monte Carlo statistical uncertainty, $\sigma_{ij}^{\text{fit}}$ , in the definition of $\chi^2_{\cos \theta}$ . These $P_\tau$ values will be used to determine the values of $\langle P_\tau \rangle$ and $A_{\text{FB}}^{\text{Pol}}$ . The last two columns list $P_\tau$ and $\chi^2_{\cos \theta}$ for the fits which do not include $\sigma_{ij}^{\text{fit}}$ , and these values of $P_\tau$ will be used to determine the statistical uncertainty on $\langle P_\tau \rangle$ and $A_{\text{FB}}^{\text{Pol}}$ . . . . .	65

5.2	This table lists the contributions to the systematic errors on the quantities measured in this analysis. The average $\tau$ polarization, $\langle P_\tau \rangle$ , and the forward-backward tau polarization asymmetry, $A_{\text{FB}}^{\text{Pol}}$ , do not assume lepton universality. The lepton asymmetry, $A_{e\tau}$ , is determined assuming lepton universality. . . . .	68
5.3	Contributions to the Monte Carlo statistical error from the correction factors, $C_{ij}^\pm$ , and the Monte Carlo generated theoretical function, $I_{ij}^\pm$ . . . .	68
5.4	Individual systematic error contributions from uncertainties in the measured branching ratios of the background channels. . . . .	70
5.5	Details of the systematic error due to uncertainty in the $a_1$ resonance shape.	71
6.1	This table lists the values of $\sin^2 \hat{\theta}_W^\ell$ derived from several measurements by the four LEP experiments, and a recent measurement of the left-right asymmetry, $A_{\text{LR}}$ , by the SLD collaboration at SLAC. . . . .	80
A.1	This table lists the values used to determine the $\tau^- \rightarrow h^- \pi^0 \nu_\tau$ branching ratio. . . . .	88
A.2	Relative backgrounds in the final sample as estimated from the Monte Carlo. . . . .	89
A.3	Contributions to the systematic error of the $\tau^- \rightarrow h^- \pi^0 \nu_\tau$ branching ratio.	89

# List of Figures

1.1	The theories of beta decay. Figure (a) represents the theory proposed by Fermi, where the interaction is at a point. Figure (b) shows the Standard Model, where the neutron decays into a proton and a $W^-$ . The $W^-$ subsequently decays via $W^- \rightarrow e^- \bar{\nu}_e$ . . . . .	3
1.2	Diagram (a) shows the reaction which violates unitarity if only two charged vector bosons are included in the theory of weak interactions. Diagram (b) shows the equivalent reaction which modifies the total cross-section for the interaction and satisfies the unitarity condition. . . . .	3
1.3	Neutral current interactions observed by the Gargamelle bubble chamber.	5
1.4	Total cross section for $e^+e^- \rightarrow \tau^+\tau^-$ calculated at the Born level. . . . .	6
1.5	The $Z^0$ interacts with each of the fermion-antifermion pairs shown. Consequently it decays to all the pairs which are lighter than the $Z^0$ mass. . . . .	7
2.1	This figure shows the helicity configurations which contribute to the cross-section for the process $e^+e^- \rightarrow Z^0 \rightarrow \tau^+\tau^-$ . The thin arrows show the momentum vector of the particle, and the thick arrows show the helicity of the particle. Events like diagrams (a) and (b) vary as $(1 + \cos \theta)^2$ , where $\theta$ is the angle of the $\tau^-$ in the lab frame. Events like (c) and (d) vary as $(1 - \cos \theta)^2$ . . . . .	15

2.2	This figure shows the variation of the forward-backward asymmetry and the average tau polarization asymmetry as a function of $\sin^2 \theta_W$ . The vertical dotted line shows the current world average value for the weak mixing angle. We can see that the polarization is much more sensitive to the value of $\sin^2 \theta_W$ . . . . .	18
2.3	Feynman diagrams showing the first order photonic radiative corrections.	19
2.4	Total $e^+e^- \rightarrow \tau^+\tau^-$ cross-section without photonic corrections (solid line) and with photonic corrections (dashed line). . . . .	21
2.5	This figure shows the forward-backward asymmetry and the tau polarization as a function of centre-of-mass energy without photonic corrections (solid line) and with photonic corrections (dashed line). . . . .	22
2.6	This figure shows the Feynman diagrams corresponding to the propagator corrections. The shaded area includes all possible one-loop diagrams involving $f\bar{f}$ pairs in the loop. . . . .	23
2.7	This figure shows the Feynman diagrams corresponding to the vertex corrections as well as the box diagrams where neither vector boson is a photon. . . . .	24
2.8	This figure shows the two possible spin orientations of the $\rho^-$ . The sum of the spins of the $\nu_\tau$ and the $\rho^-$ must equal the spin of the $\tau^-$ . Diagram (a) represents the spin combination $ \frac{1}{2}, \frac{1}{2}\rangle_\tau =  \frac{1}{2}, -\frac{1}{2}\rangle_{\nu_\tau}  1, 1\rangle_\rho$ , and diagram (b) represents the spin combination $ \frac{1}{2}, \frac{1}{2}\rangle_\tau =  \frac{1}{2}, \frac{1}{2}\rangle_{\nu_\tau}  1, 0\rangle_\rho$ . . . . .	26
2.9	This figure shows the angular distribution of $\tau^- \rightarrow \rho^- \nu_\tau$ events in $\cos \theta^*$ for three values of the polarization, $\langle P_\tau \rangle$ . The maximum slope (ie. for $\langle P_\tau \rangle = \pm 1$ ) is less than one due to the dilution from the two allowed spin orientations of the $\rho^-$ . The Standard Model value for the polarization is $\langle P_\tau \rangle = -0.14$ . . . . .	27

2.10	This figure shows the angular distribution of $\tau^- \rightarrow \rho^- \nu_\tau$ events in $(\cos \theta^*, \cos \psi)$ for three values of the polarization, $\langle P_\tau \rangle$ . The sensitivity to the value of the polarization is improved over the one-dimensional distribution with the addition of the information from the $\rho^- \rightarrow \pi^- \pi^0$ decay. . . . .	28
3.1	This figure shows a schematic of the injection scheme for LEP. . . . .	30
3.2	This figure shows a schematic of the LEP main ring with the locations of the four experimental arcs indicated. . . . .	32
3.3	This figure shows the LEP delivered luminosity up to the end of the 1993 running period. . . . .	33
3.4	Cutaway view of the OPAL detector showing the major subdetector components. . . . .	34
3.5	This figure shows a schematic of the central tracking detectors (the silicon detector is not shown here). The vertex chamber, jet chamber, and $z$ -chamber are contained within the pressure vessel which maintains a constant 4 bar pressure. . . . .	35
3.6	This figure shows a schematic of the vertex drift chamber. The inner wire planes return information on the axial position ( $r$ - $\phi$ position) of particles as they traverse the detector, and the outer wire planes return stereo information ( $z$ position) for the particles. . . . .	36
3.7	This figure shows the orientation of the lead glass blocks in the electromagnetic calorimeter. (a) shows that the lead glass blocks point slightly away from the $z$ -coordinate of the interaction point; (b) shows that the blocks also point away from the $r$ - $\phi$ vertex position. . . . .	39
3.8	This figure shows the principle of the track finding in the $r$ - $z$ plane of the jet chamber. Histogram (a) shows the variable $z/r$ would look like for a track originating at the origin. Histogram (b) shows this variable for a track not originating at the origin. The values of $z/r$ at each jet chamber ring would be different for this track. . . . .	41

4.1	This figure shows the distribution of events in $E/p$ after all other selection requirements are applied. The $E/p = 0$ bin has been plotted separately with a different scale. . . . .	52
4.2	This figure shows $x \equiv p_{\text{trk}}/E_{\text{beam}}$ after all other selection requirements are applied. . . . .	53
4.3	This figure shows the reconstructed mass of the neutral clusters in events which contain two neutral clusters, after applying all selection requirements other than the two cluster mass requirement. . . . .	54
4.4	This figure shows the distribution of the reconstructed mass of the events after all other selection criteria are applied. The data and the Monte Carlo are in good agreement. . . . .	55
5.1	This figure shows the detector resolution correction factors, where the positive and negative helicity states have been averaged together. Each plot shows the variation of $R_{ij}$ with $\cos \theta^*$ . The plots are arranged in increasing $\cos \theta$ (from $-0.68$ to $+0.68$ ) across the page, and increasing $\cos \psi$ (from $-1$ to $+1$ ) up the page. The dotted line in each plot shows the value 1, for which the reconstructed $\cos \theta^*$ - $\cos \psi$ bin contents would equal the four-vector bin contents. . . . .	60
5.2	This figure shows the correction factors for the backgrounds, where the positive and negative helicity states have been averaged together. Each plot shows the variation of $f_{(\text{bg}) ij}$ with $\cos \theta^*$ . The plots are arranged in increasing $\cos \theta$ (from $-0.68$ to $+0.68$ ) across the page, and increasing $\cos \psi$ (from $-1$ to $+1$ ) up the page. . . . .	61
5.3	This figure shows the selection efficiency correction factors, where the positive and negative helicity states have been averaged together. Each plot shows the variation of $\epsilon_{ij}$ with $\cos \theta^*$ , and the plots are arranged in increasing $\cos \theta$ (from $-0.68$ to $+0.68$ ) across the page, and increasing $\cos \psi$ (from $-1$ to $+1$ ) up the page. . . . .	63

- 5.4 This figure shows the measured polarization as a function of  $\cos \theta$ . The data points are the values determined with  $\sigma_{ij}^{\text{fit}}$  included in the definition of  $\chi_{\cos \theta}^2$ . The error bars are the data statistical errors only. The dotted curve represents the fitted theoretical model without assuming lepton universality, and the solid curve represents the fitted model assuming lepton universality. . . . . 67
- 6.1 Figure (a) shows the value of  $\langle P_\tau \rangle$  measured in this thesis compared against the LEP measurements using only the  $\tau^- \rightarrow \rho^- \nu_\tau$  decay channel. The L3 result only shows the statistical error, since they do a global fit to all measured channels before evaluating systematic uncertainties. Figure (b) shows the value of  $\langle P_\tau \rangle$  measured in this thesis compared against OPAL results for the dominant  $\tau^-$  decay channels. . . . . 75
- 6.2 This figure shows the variation of (a)  $A_\tau$ , (b)  $A_e$ , and (c)  $A_\ell \equiv A_{e\tau}$  as a function of the mass of the top quark. The hatched area shows the variation of the Standard Model prediction for Higgs masses between 50 GeV/c<sup>2</sup> and 1000 GeV/c<sup>2</sup>. The vertical bands represent the measurements made in this analysis. . . . . 76
- 6.3 Figure (a) shows the values of  $\sin^2 \hat{\theta}_W^\ell$  derived from  $\langle P_\tau \rangle$  by the LEP collaborations. Figure (b) shows the OPAL results for  $\sin^2 \hat{\theta}_W^\ell$  derived using several different methods. . . . . 79
- 6.4 This figure shows the variations, at the Born level, of the asymmetries measured by the LEP collaborations as a function of  $\sin^2 \theta_W$ . The sign of  $\langle P_\tau \rangle$  has been changed so that a direct comparison of the slopes of the functions can be made. The tau polarization asymmetry,  $\langle P_\tau \rangle$ , is the most sensitive quantity to the value of  $\sin^2 \theta_W$ . . . . . 81

- 7.1 This figure shows the variation of  $\sin^2 \hat{\theta}_W$  as a function of the mass of the top quark. The hatched area shows the variation of the Standard Model prediction for Higgs masses between 50 GeV/c<sup>2</sup> and 1000 GeV/c<sup>2</sup>. The vertical band represents the value measured in this analysis. . . . . 83
- A.1 This figure shows the branching ratio measured in this analysis in comparison with previous measurements. The Particle Data Group (PDG) results are evaluated using the results referenced in this diagram (excluding the Mark II and Mark III results). . . . . 93

# Acknowledgements

I wish to thank many people for their generous contributions to this analysis. I thank the members of the OPAL collaboration for their efforts and ingenuity in operating the experiment and producing the data used here. I would like to express my most sincere gratitude to M. Roney for his enormous effort and patience in helping me to understand the intricacies of tau decays. I would also like to thank to Richard Keeler and Randy Sobie for conversations too numerous to count in which I was enlightened about some of the more complicated concepts in Standard Model physics. I also wish to thank them for their critical reading of this thesis. Finally, I would like to thank Joanne for her infinite patience and support during the course of my studies.

# Chapter 1

## Introduction

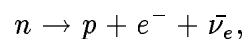
The neutral weak interaction is the focus of the investigation presented in this thesis. We will present a brief historical overview of weak interactions, beginning with the proposal and discovery of the neutrino and its important role in weak interaction physics, leading to the formulation of the Standard Model of electroweak physics, a theory which unifies the weak and electromagnetic interactions. We will see how this theory was used to predict the existence of heavy mediators of the weak interaction, the  $W^+$ ,  $W^-$ , and  $Z^0$ . The predictions of the Standard Model can be tested through the many decay modes of the  $Z^0$ . In particular, we will show how the decay of the  $Z^0$  to  $\tau^+\tau^-$  pairs provides a unique method for probing the Standard Model.

During the first 25 years of this century, scientists studied the radioactive decay of nuclei. In the process known as beta decay, a radioactive nucleus is transformed into a lighter nucleus with the emission of an electron. In such a two-body decay, the electron should be emitted at a single, well-defined energy due to the conservation of momentum. However, Ellis and Wooster [1] determined that the energy spectrum of the electrons emitted in beta decay was, in fact, continuous. Numerous proposals were made to explain this discrepancy, and in 1930 Wolfgang Pauli suggested that perhaps there might be another particle emitted with the electron which carries off the missing energy. This particle would have no net charge and would be difficult to detect, which would explain why nobody had seen one. When Enrico Fermi developed a theory of beta decay four years later, he included Pauli's hypothetical particle, which he called the neutrino, and was able to

successfully describe the energy spectrum of the beta decay electrons. Fermi's treatment was so successful at describing the available experimental data that even without direct evidence, the existence of neutrinos was generally accepted. A direct observation of neutrinos was eventually made in 1953 by F. Reines and C.L. Cowan, Jr.[2] by studying inverse beta decay. The neutrino was found only to interact by the weak force and to be unaffected by the electromagnetic and strong forces, and therefore provided a key tool in the study of weak interactions for the next 30 years.

One of the first discoveries made after the detection of neutrinos was the surprising find that parity is not conserved in weak interactions. In 1956, Lee and Yang [3] examined the experimental data available at the time and realized that while there was strong evidence for parity conservation in strong and electromagnetic interactions, there was no such evidence for weak interactions. They proposed several experiments that could be performed which would test for parity violation in weak decays, and a year later C.S. Wu and her collaborators [4] determined that parity was indeed violated in weak decays. Further experiments [5, 6, 7] showed that, within experimental errors, the neutrinos were completely left-handed and thus parity was not partly violated in weak interactions, but violated maximally.

Fermi's theory of beta decay had assumed that the decaying neutron produced the proton, electron, and electron-antineutrino at a point,



requiring no mediating particle for the interaction (see figure 1.1a). It was understood that when the interaction was taken to higher energies the theory would begin to break down because the predicted cross-sections would increase to infinity and violate unitarity. Fermi's theory was replaced by one that used a charged, spin one particle to mediate the weak interaction (see figure 1.1b). The charged current nature of the weak interaction, where charge is transferred from one particle to the other (ie. from the neutron with zero charge to the proton with positive charge), implied the existence of at least two of these mediators with opposite charge. The addition of the charged mediators still left a problem with unitarity in the reaction  $\nu\bar{\nu} \rightarrow W^+W^-$  (see figure 1.2(a)). The cross-section of this

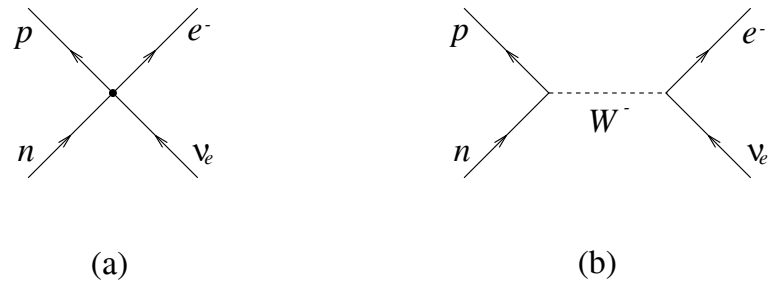


Figure 1.1: The theories of beta decay. Figure (a) represents the theory proposed by Fermi, where the interaction is at a point. Figure (b) shows the Standard Model, where the neutron decays into a proton and a  $W^-$ . The  $W^-$  subsequently decays via  $W^- \rightarrow e^- \bar{\nu}_e$ .

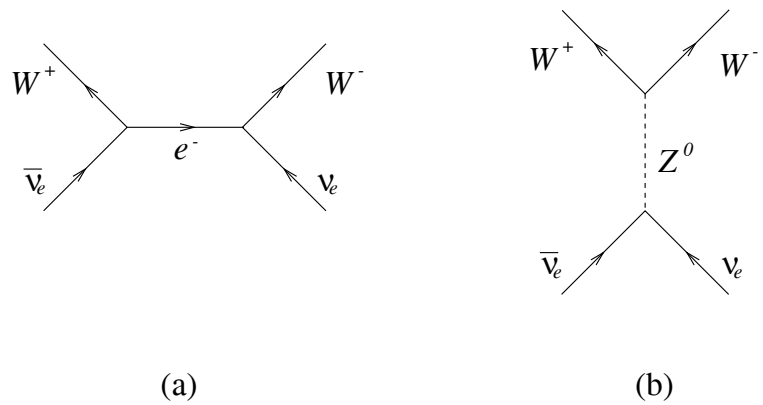


Figure 1.2: Diagram (a) shows the reaction which violates unitarity if only two charged vector bosons are included in the theory of weak interactions. Diagram (b) shows the equivalent reaction which modifies the total cross-section for the interaction and satisfies the unitarity condition.

process also increased with the square of the energy of the neutrinos, and a third, neutral mediator of the weak interaction was required to cancel this effect (see figure 1.2(b)). These three intermediate vector bosons would form a triplet of weak bosons in contrast to the singlet of the electromagnetic interaction, the photon. The only difficulty was that a neutral weak boson implied the existence of neutral currents, where there was no charge exchange in the interactions. Such weak neutral currents had not yet been observed.

In the 1960s, a theory [8] emerged that was able to explain why weak neutral current interaction had not yet been seen. This theory combined the electromagnetic and weak interactions, a possibility suggested by the many similarities between the two interactions and the observation that leptons were involved in both processes. Electromagnetism had been successfully described by the Yang-Mills gauge theory and it was thought that perhaps an extension of this gauge theory would be appropriate for describing weak interactions. In 1961, Sheldon Glashow showed how a left-handed  $SU(2)$  gauge group could be combined with the  $U(1)$  gauge group of electromagnetism to produce a theory that could describe both the observed electromagnetic and weak interactions, where the strengths of the interactions would be related to a *weak mixing angle*,

$$\sin \theta_W = \frac{e}{g}, \quad (1.1)$$

where  $e$  is the coupling strength in electromagnetic interactions and  $g$  is the coupling strength in weak interactions. This idea was expanded by Steven Weinberg and Abdus Salam who formulated Glashow's model as a 'spontaneously broken gauge theory,' where the large difference between the masses of the photon (zero mass) and the weak mediators (very massive) could be explained as a consequence of the broken symmetry of a scalar field. This symmetry breaking would also produce a *Higgs* particle, which has not yet been observed. The ideas put forth by Glashow, Salam, and Weinberg are known today as the *GSW model* or the *Standard Model* of electroweak interactions.

The Standard Model predicted that weak neutral currents should exist. The difficulty with observing weak neutral currents was that they were overwhelmed by the electromagnetic neutral current interactions. The only way to unequivocally prove that weak neutral currents existed was to look for interactions involving neutrinos, as they have no

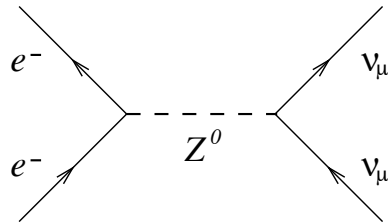


Figure 1.3: Neutral current interactions observed by the Gargamelle bubble chamber.

electromagnetic component. Neutrinos had so far only been observed in charged current events where an incident neutrino induces the creation of a lepton (electron or muon) and thus changes the charge on the target nucleon (as in inverse beta decay). Finally, in 1973, the Gargamelle bubble chamber experiment at CERN [10] found events of the type

$$\bar{\nu}_\mu + e^- \rightarrow \bar{\nu}_\mu + e^-$$

and

$$\bar{\nu}_\mu + N \rightarrow \bar{\nu}_\mu + X,$$

(see figure 1.3) thus proving that weak neutral currents do exist.

Following these exciting discoveries, the remainder of the 1970s were spent trying to experimentally test the predictions from the Standard Model. Much of this work was performed at  $e^+e^-$  collider facilities such as SPEAR, PETRA, PEP, and TRISTAN, which investigated interactions that took place at intermediate energies,  $\sqrt{s} < M_Z$ , where the interference effects between the electromagnetic and weak interactions could be studied. It wasn't until the early 1980's, however, that the existence of the intermediate vector bosons was confirmed and their masses measured by the UA1 [11] and UA2 [12] collaborations.

The discovery of the mediators of the weak interaction provided strong support for the Standard Model. It had been suggested that precise tests of the Standard Model could be performed if a laboratory could be built which would produce large numbers (several millions) of  $Z^0$ 's. This is possible due to the large total cross-section for  $Z^0$  production at the  $Z^0$  mass resonance (see figure 1.4). Two such facilities now exist, the Large Electron Positron collider (LEP) at CERN and the Stanford Linear Collider (SLC) at Stanford,

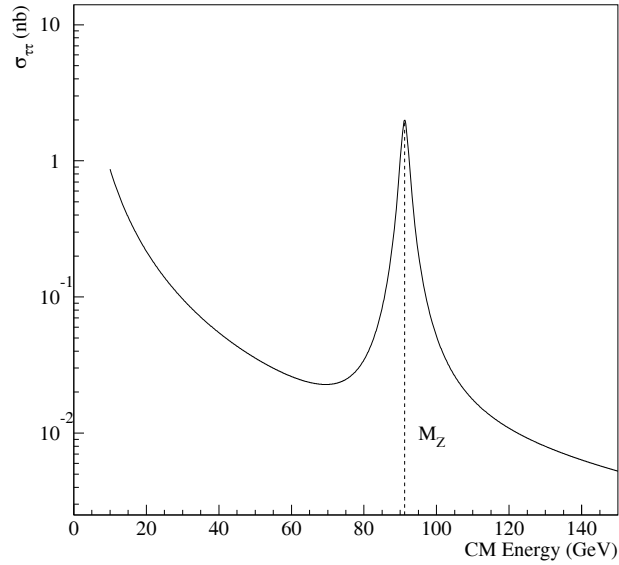


Figure 1.4: Total cross section for  $e^+e^- \rightarrow \tau^+\tau^-$  calculated at the Born level.

where electrons and positrons are collided at energies around the  $Z^0$  mass resonance, annihilating each other and producing copious quantities of  $Z^0$  particles. A  $Z^0$  decays into any of the fermion-antifermion pairs shown in figure 1.5, with the exception of top, which is apparently too massive [13].

This thesis concentrates on parity violation and lepton universality. Interactions which are invariant under parity are the same when mirror reversed (co-ordinate inversion). The coupling of the initial state leptons ( $e^+e^-$  at LEP) produces a polarized  $Z^0$  due to parity violation, and the decay of this polarized  $Z^0$  into a fermion-antifermion pair results in an asymmetric angular distribution of the final state particles. Finally, the coupling of the  $Z^0$  to the final state induces a polarization of the final state fermions which can also be measured.

Lepton universality is the idea that the coupling strengths of the intermediate vector bosons to each of the three lepton generations or families (ie. the electron, muon, and tau)

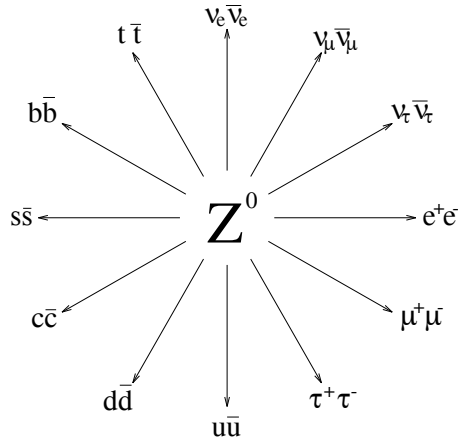


Figure 1.5: The  $Z^0$  interacts with each of the fermion-antifermion pairs shown. Consequently it decays to all the pairs which are lighter than the  $Z^0$  mass.

should be equal. In this thesis, we will measure the couplings of the  $e$  and  $\tau$  to the  $Z^0$ . These couplings can be separated by measuring the angular variation in the polarization of the taus.

In this thesis, we will use the reaction  $e^+e^- \rightarrow Z^0 \rightarrow \tau^+\tau^-$  to test lepton universality and parity violation and then, assuming lepton universality, make a measurement of  $\sin^2 \theta_W$ . The Standard Model makes no prediction for  $\sin^2 \theta_W$ . It must be measured before it can be used to calculate other observables of the Standard Model. If the Standard Model is correct, then the value of the weak mixing angle measured here should be consistent with other measurements that have been made using different techniques. Finally, the value of  $\sin^2 \theta_W$  can be used to place restrictions on the types of extensions (ie. new physics) that can be made to the Standard Model.

In chapter 2 of this thesis, we will show that polarization studies are feasible at LEP with  $\tau$ 's. The details of the relationship between the angular distributions of the final state  $\tau$  leptons, the  $\tau$  polarization, and the weak mixing angle will be discussed. The analysis presented here measures the angular distributions of the decay  $\tau^- \rightarrow \rho^- \nu_\tau$ , since this decay has a high sensitivity to the tau polarization and a high branching ratio. The angular distributions will also be used to describe the couplings of the incident electron/positron

pair in the production of the neutral vector boson via  $e^+e^- \rightarrow Z^0$  at the LEP collider. The forward-backward tau polarization asymmetry will be defined and its relationship to the weak mixing angle discussed. Chapter 2 will also discuss the radiative corrections that must be made when determining  $\sin^2 \theta_W$ .

Chapter 3 begins with an overview of the LEP collider. A brief description of the OPAL detector follows, discussing the detector subcomponents as well as the data processing chain. In chapter 4, the data and Monte Carlo samples are described. The selection requirements are divided into two stages where the tau pair events are first identified and then the  $\tau^- \rightarrow \rho^- \nu_\tau$  events are selected for the final analysis. Chapter 5 presents the results on the average tau polarization and the forward-backward tau polarization asymmetry. In chapter 6, these results are discussed and compared to previous measurements. The weak mixing angle is evaluated using both of these quantities and the two values compared to test lepton universality. Under the assumption of lepton universality, a final value of  $\sin^2 \theta_W$  is derived and compared with other recent measurements of this quantity using alternate techniques. Chapter 7 concludes with a final discussion of the results presented here.

# Chapter 2

## Theory

This chapter will describe how we can use the measurement of the tau polarization asymmetries to investigate the left-right asymmetry of the weak interaction. We introduce the fundamental particles of nature and the Standard Model description of the electroweak interaction, focusing on the relationship between the neutral current interaction and the weak mixing angle. The second section shows how we define the average tau polarization asymmetry and the forward-backward tau polarization asymmetry and how they can be used to determine the weak mixing angle. This section also describes the higher order radiative corrections to these asymmetries. Finally, the last section shows how the asymmetries will be determined based on energy and momentum measurements in the detector.

### 2.1 The Standard Model and Neutral Currents

All known matter is composed of fermions (particles with half-integer spin) and can be divided into two types: leptons and quarks. The electron, muon, tau, and their associated neutrinos are leptons. Baryons such as protons and neutrons are composed of quark triplets, and mesons such as  $\pi$ 's and  $\rho$ 's, are composed of quark-antiquark pairs. Fermions interact through the exchange of bosons (particles with integer spin) which act as the mediators of the interaction. Table 2.1 lists the fundamental fermions and bosons, along with some of the quantum numbers that are important in the Standard Model.

The weak interactions of the quarks and leptons depend on whether the particle's

Fermions			$Q_f$	$T_f$	$T_f^3$	$Y_f$
$\begin{pmatrix} u \\ d \end{pmatrix}_L$	$\begin{pmatrix} c \\ s \end{pmatrix}_L$	$\begin{pmatrix} t \\ b \end{pmatrix}_L$	2/3 -1/3	1/2 1/2	1/2 -1/2	1/3 1/3
$\begin{pmatrix} \nu_e \\ e \end{pmatrix}_L$	$\begin{pmatrix} \nu_\mu \\ \mu \end{pmatrix}_L$	$\begin{pmatrix} \nu_\tau \\ \tau \end{pmatrix}_L$	0 -1	1/2 1/2	1/2 -1/2	-1 -1
$u_R$	$c_R$	$t_R$	2/3	0	0	4/3
$d_R$	$s_R$	$b_R$	-1/3	0	0	-2/3
$e_R$	$\mu_R$	$\tau_R$	-1	0	0	-2
Bosons						
	$\gamma$		0			
	$Z^0$		0			
	$W^\pm$		$\pm 1$			

Table 2.1: Standard Model particles and some relevant quantum numbers. Each of the fermions has an antiparticle equivalent for which the quantum numbers have opposite sign.

spin is aligned with its momentum (right-handed helicity) or opposite to its momentum (left-handed helicity). The underlying symmetry of the Standard Model is given by the group  $SU_L(2) \times U(1)$  [14], where the subscript  $L$  refers to left-handed particles. The two components of this group,  $SU_L(2)$  and  $U(1)$  represent symmetries that are associated with two of the quantum numbers assigned to each fermion. By analogy with nuclear isospin, a *weak isospin* ( $T_f$  in table 2.1) is associated with each of the fermions. Weak isospin is a representation of the symmetry in the group  $SU_L(2)$ . As with the proton and neutron of nuclear isospin, weak doublets of left-handed fermions are formed with isospin  $\frac{1}{2}$  and the projections of  $T_f^3 = \pm\frac{1}{2}$  assigned to the fermions as shown in the table. The group  $U(1)$  is identified with the neutral interaction, and the quantum number associated with this symmetry is the *weak hypercharge*,  $Y_f$ , which satisfies the relation

$$Q_f = T_f^3 + \frac{Y_f}{2}, \quad (2.1)$$

where  $Q_f$  is the fermion charge.

The Standard Model describes the electromagnetic and weak interactions as resulting from fundamental interactions depending on the weak isospin and weak hypercharge. The isotriplet vector fields  $W_\mu^i$  couple with strength  $g$  to the weak isospin current  $J_\mu^i$ , and the

singlet vector field  $B_\mu$  couples to the weak hypercharge current  $j_\mu^Y$  with strength  $g'/2$ . The full electroweak Lagrangian is given by

$$\mathcal{L} = -igJ_\mu^i(W^i)^\mu - i\frac{g'}{2}j_\mu^Y B^\mu. \quad (2.2)$$

The physical charged intermediate vector bosons are given as linear combinations of the first two fields of the weak triplet,

$$W_\mu^\pm = \frac{1}{\sqrt{2}}(W_\mu^1 \mp iW_\mu^2), \quad (2.3)$$

and the photon and neutral weak particle are identified with linear combinations of the singlet field and the third component of the triplet field,

$$\begin{aligned} A_\mu &= B_\mu \cos \theta_W + W_\mu^3 \sin \theta_W \\ Z_\mu &= -B_\mu \sin \theta_W + W_\mu^3 \cos \theta_W. \end{aligned} \quad (2.4)$$

The  $W^\pm$  and  $Z^0$  acquire mass through spontaneous symmetry breaking by the *Higgs mechanism*. The masses are related at the Born level to the weak mixing angle through the relation

$$\sin^2 \theta_W = 1 - \frac{M_W^2}{M_Z^2}. \quad (2.5)$$

The interaction amplitudes for an  $f\bar{f}$  pair are given in the Standard Model by

The diagrams and their corresponding amplitudes are:

- Photon ( $\gamma$ ):** A wavy line representing the photon connects to a fermion line ( $f$ ) and an antifermion line ( $\bar{f}$ ). The amplitude is  $Q_f \bar{f} \gamma^\mu f A_\mu$ .
- Charged W boson ( $W^\pm$ ):** A dashed line representing the  $W^\pm$  boson connects to a fermion line ( $f$ ) and an antifermion line ( $\bar{f}'$ ). The amplitude is  $\frac{g}{\sqrt{2}} \bar{f}' \gamma^\mu (1 - \gamma^5) f W_\mu$ .
- Neutral Z boson ( $Z^0$ ):** A dashed line representing the  $Z^0$  boson connects to a fermion line ( $f$ ) and an antifermion line ( $\bar{f}$ ). The amplitude is  $\frac{g}{2 \cos \theta_W} \bar{f} \gamma^\mu (v_f - a_f \gamma^5) f Z_\mu$ .

Fermion	$v_f$	$a_f$	$c_L$	$c_R$
$\nu_e, \nu_\mu, \nu_\tau$	$\frac{1}{2}$	$\frac{1}{2}$	1	0
$e, \mu, \tau$	$-\frac{1}{2} + 2 \sin^2 \theta_W$	$-\frac{1}{2}$	$-1 + 2 \sin^2 \theta_W$	$2 \sin^2 \theta_W$
$u, c, t$	$\frac{1}{2} - \frac{4}{3} \sin^2 \theta_W$	$\frac{1}{2}$	$1 - \frac{4}{3} \sin^2 \theta_W$	$-\frac{4}{3} \sin^2 \theta_W$
$d, s, b$	$-\frac{1}{2} + \frac{2}{3} \sin^2 \theta_W$	$-\frac{1}{2}$	$-1 + \frac{2}{3} \sin^2 \theta_W$	$\frac{2}{3} \sin^2 \theta_W$

Table 2.2: This table shows the coupling constants,  $v_f$ ,  $a_f$ ,  $c_L$ , and  $c_R$ , in the weak neutral current interaction.

where  $\gamma^\mu$  are the Dirac matrices and  $\gamma^5 = -i\gamma^0\gamma^1\gamma^2\gamma^3$ . The term  $(1 - \gamma^5)$  in the charged weak interaction represents the fact that this interaction is purely left-handed. The neutral weak interaction contains vector ( $v_f$ ) and axial-vector ( $a_f$ ) factors which indicate that there are both left-handed and right-handed components in this interaction. These factors are related to the relative coupling strengths of the left-handed ( $c_L$ ) and right-handed ( $c_R$ ) components of the interaction by

$$\begin{aligned} v_f &= \frac{1}{2}(c_L + c_R) \\ a_f &= \frac{1}{2}(c_L - c_R), \end{aligned} \quad (2.6)$$

and are defined in the Standard Model in terms of  $\sin^2 \theta_W$ , the charge and the weak isospin by

$$\begin{aligned} v_f &= T_f^3 - 2 Q_f \sin^2 \theta_W \\ \text{and} \quad a_f &= T_f^3. \end{aligned} \quad (2.7)$$

The Standard Model predictions of these constants are listed in table 2.2. The Standard Model assumes that the couplings for electrons, muons, and taus should be identical, an assumption known as *lepton universality*. In this analysis, we will test this by measuring the  $e$  and  $\tau$  couplings to the  $Z^0$ .

Only the ratio of the vector coupling to the axial-vector coupling will be determined in this analysis, so by using equation 2.7 a value of the weak mixing angle can be determined from

$$\sin^2 \theta_W^\ell = \frac{T_f^3}{2 Q_f} \left( 1 - \frac{v_f}{a_f} \right). \quad (2.8)$$

For leptons, this becomes

$$\sin^2 \theta_W^\ell = \frac{1}{4} \left( 1 - \frac{v_\ell}{a_\ell} \right). \quad (2.9)$$

Note that if  $\sin^2 \theta_W = \frac{1}{4}$ , the neutral weak interaction would be purely axial vector ( $v_f = 0$ ) and there would be no parity violation.

## 2.2 Cross Section and Asymmetries

In this section, we will introduce the Born level approximation of the cross-section for the process  $e^+e^- \rightarrow \tau^+\tau^-$ . We will define the asymmetries and show how these are related to the neutral current couplings. The radiative corrections, which must be accounted for at LEP energies, will be presented. We will show how these corrections can be included without changing the form of the Born cross-section.

### 2.2.1 Born Level Approximation

The matrix element for the Born-level differential cross-section for  $e^+e^- \rightarrow \tau^+\tau^-$  is the sum of the two contributions from the electromagnetic and neutral weak interactions [15],

$$\begin{aligned} \mathcal{M} &= \mathcal{M}_\gamma + \mathcal{M}_Z \\ &= -\frac{4\pi\alpha}{s} (\bar{\tau}\gamma^\nu\tau)(\bar{e}\gamma_\nu e) \\ &\quad -\sqrt{2}G_\mu M_Z^2 \frac{[\bar{\tau}\gamma^\nu(v_\tau - a_\tau\gamma^5)\tau][\bar{e}\gamma_\nu(v_e - a_e\gamma^5)e]}{s - M_Z^2 + iM_Z\Gamma_Z}, \end{aligned} \quad (2.10)$$

where

$$e^2 = 4\pi\alpha \quad (2.11)$$

$$\frac{g^2}{4\cos^2\theta_W} = \sqrt{2}G_\mu M_Z^2, \quad (2.12)$$

and  $G_\mu$  is the Fermi coupling constant. The differential cross-section can then be calculated from the square of the matrix element as a function of the  $\tau^-$  helicity  $h_{\tau^-}$ , the centre-of-mass energy  $\sqrt{s}$ , and the production angle  $\theta$  of the  $\tau^-$  [16]

$$\begin{aligned} \frac{d\sigma_{\text{Born}}}{d\cos\theta}(s, \cos\theta; h_{\tau^-}) &= \frac{\pi\alpha^2}{4s} \left\{ (1 + \cos^2\theta)[F_0(s) - h_{\tau^-}F_2(s)] \right. \\ &\quad \left. + 2\cos\theta[F_1(s) - h_{\tau^-}F_3(s)] \right\} \end{aligned} \quad (2.13)$$

where the form factors  $F_i(s)$  are given by

$$\begin{aligned}
F_0(s) &= 1 + 2\text{Re}[\chi(s)]v_e v_\tau + |\chi(s)|^2(v_e^2 + a_e^2)(v_\tau^2 + a_\tau^2), \\
F_1(s) &= 2\text{Re}[\chi(s)]a_e a_\tau + |\chi(s)|^2 2v_e a_e 2v_\tau a_\tau, \\
F_2(s) &= 2\text{Re}[\chi(s)]v_e a_\tau + |\chi(s)|^2(v_e^2 + a_e^2) 2v_\tau a_\tau, \\
F_3(s) &= 2\text{Re}[\chi(s)]a_e v_\tau + |\chi(s)|^2 2v_e a_e (v_\tau^2 + a_\tau^2),
\end{aligned} \tag{2.14}$$

and

$$\chi(s) = \frac{\sqrt{2}G_\mu M_Z^2}{4\pi\alpha} \frac{s}{s - M_Z^2 + iM_Z\Gamma_Z}. \tag{2.15}$$

The total spin-averaged tree-level  $e^+e^- \rightarrow \tau^+\tau^-$  cross-section is the integral of equation 2.13 over  $\cos\theta$  and summed over  $h_{\tau^\pm} = \pm 1$ , which gives

$$\sigma_{\tau\tau} = \frac{4\pi\alpha^2}{3s} F_0, \tag{2.16}$$

shown in figure 1.4.

High energy electrons and positrons annihilating to a spin one state like the  $Z^0$  have two possible helicity combinations. Consequently, the cross-section for the process  $e^+e^- \rightarrow Z^0 \rightarrow \tau^+\tau^-$  will only have contributions from the four helicity states shown in figure 2.1. The four processes in this figure display the effects of parity violation and lepton universality. Diagrams (a) and (b) show the cases when the spins of the  $e^-$  and  $\tau^-$  are either both right-handed or both left-handed, respectively. Parity violation in the weak neutral current favours left-handed (negative helicity) states over right-handed (positive helicity) states, and so in a random event sample there will be more (b)-type events than (a)-type events. Diagrams (c) and (d) will have approximately equal numbers of events in a random event sample, since the difference in coupling to left-handed and right-handed states is cancelled by having one left-handed and one right-handed fermion state (eg.  $e_L^-$  and  $\tau_R^-$  in (d)) in each diagram. If lepton universality does not hold, however, this will not be a perfect cancellation.

The differential cross-section for each of these four processes can be written as, for example,

$$\frac{d\sigma}{d\Omega}(e_L^- e_R^+ \rightarrow \tau_L^- \tau_R^+) = \frac{\alpha^2}{4s} (1 + \cos\theta)^2 |1 + \chi(s)(v + a)_e(v + a)_\tau|^2. \tag{2.17}$$

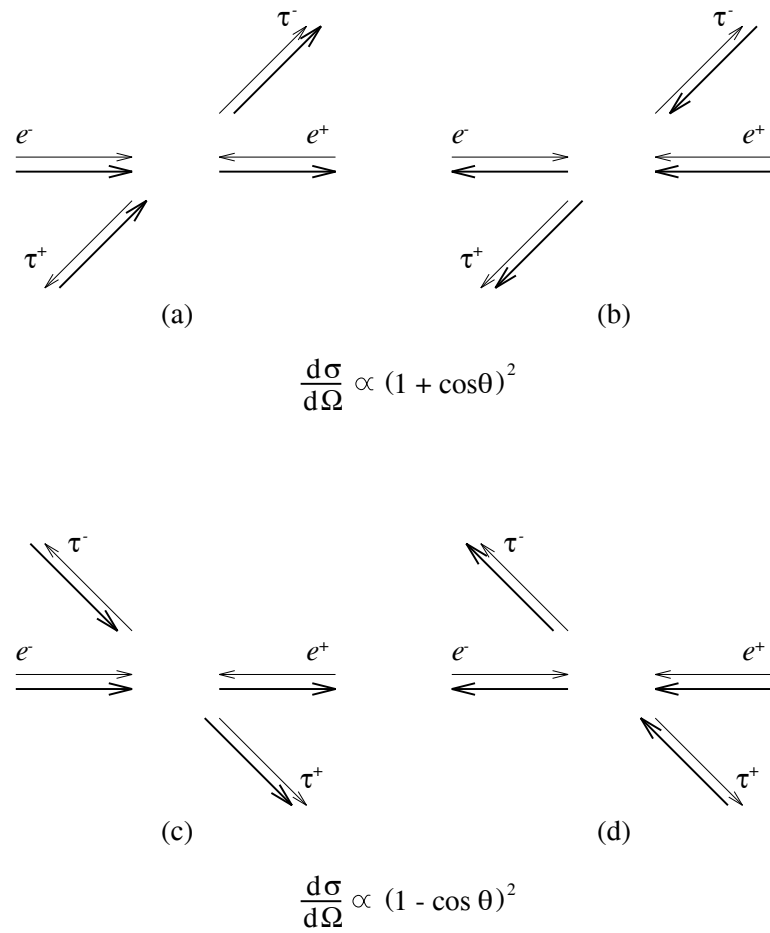


Figure 2.1: This figure shows the helicity configurations which contribute to the cross-section for the process  $e^+e^- \rightarrow Z^0 \rightarrow \tau^+\tau^-$ . The thin arrows show the momentum vector of the particle, and the thick arrows show the helicity of the particle. Events like diagrams (a) and (b) vary as  $(1 + \cos\theta)^2$ , where  $\theta$  is the angle of the  $\tau^-$  in the lab frame. Events like (c) and (d) vary as  $(1 - \cos\theta)^2$ .

Thus, if we could measure each of the four processes separately, we would be able to measure the  $v$  and  $a$  couplings directly. Since we are unable to separate these four states, we must derive the couplings from observables which are related to the angular distributions.

The observables of interest in this thesis are the asymmetries in the helicity states induced by parity violation. For unpolarized  $e^+e^-$  beams, there are three asymmetries: the average tau polarization,  $\langle P_\tau \rangle$ , the forward-backward tau polarization asymmetry,  $A_{\text{FB}}^{\text{Pol}}$ , and the forward-backward tau asymmetry,  $A_{\text{FB}}$ .

The average tau polarization represents the relative number of positive and negative helicity  $\tau^-$  events, and is defined by

$$\langle P_{\tau^-} \rangle = \frac{\sigma^+ - \sigma^-}{\sigma^{\text{tot}}} \quad (2.18)$$

where  $\sigma^\pm$  is the total cross-section for positive (negative) helicity  $\tau^-$  events from the  $Z^0$  decay. Note that since the  $Z^0$  is a spin 1 particle, the helicities of the  $\tau^-$  and  $\tau^+$  will be opposite, and  $\langle P_{\tau^-} \rangle = -\langle P_{\tau^+} \rangle \equiv \langle P_\tau \rangle$ . Integrating the Born cross-section (equation 2.13) over  $\cos \theta$  for the appropriate helicity states leads to

$$\langle P_\tau \rangle = -\frac{F_2}{F_0} \approx -\frac{2v_\tau/a_\tau}{1 + (v_\tau/a_\tau)^2}, \quad (2.19)$$

where the approximation is valid at energies near the  $Z^0$  mass resonance. We can see that with this approximation the polarization is a function of only the tau coupling constants. If we define the ratio

$$A_\ell \equiv \frac{2v_\ell/a_\ell}{1 + (v_\ell/a_\ell)^2}, \quad (2.20)$$

the average tau polarization is given by

$$\langle P_\tau \rangle = -A_\tau. \quad (2.21)$$

The forward-backward tau polarization asymmetry represents the difference between the average tau polarization in the forward hemisphere ( $\cos \theta > 0$ ) and the backward hemisphere ( $\cos \theta < 0$ ). This quantity is defined by

$$A_{\text{FB}}^{\text{Pol}} = \frac{[\sigma^+(\cos \theta > 0) - \sigma^-(\cos \theta > 0)] - [\sigma^+(\cos \theta < 0) - \sigma^-(\cos \theta < 0)]}{\sigma^{\text{tot}}} \quad (2.22)$$

which reduces to

$$A_{\text{FB}}^{\text{Pol}} = -\frac{3}{4} \frac{F_3}{F_0} \approx -\frac{3}{4} \frac{2v_e/a_e}{1 + (v_e/a_e)^2} \quad (2.23)$$

which, in the approximation  $\sqrt{s} \approx M_Z$ , is a function of only the electron couplings to the  $Z^0$ . The forward-backward tau polarization asymmetry can be written as

$$A_{\text{FB}}^{\text{Pol}} = -\frac{3}{4} A_e. \quad (2.24)$$

Finally, the forward-backward tau asymmetry describes the angular distribution of the events without regard to the helicities. It is defined by

$$A_{\text{FB}} = \frac{\sigma(\cos \theta > 0) - \sigma(\cos \theta < 0)}{\sigma^{\text{tot}}}. \quad (2.25)$$

which, for  $\sqrt{s} \approx M_Z$ , reduces to

$$A_{\text{FB}} = \frac{3}{4} \frac{F_1}{F_0} \approx \frac{3}{4} \frac{2(v_e/a_e)}{1 + (v_e/a_e)^2} \frac{2(v_\tau/a_\tau)}{1 + (v_\tau/a_\tau)^2}. \quad (2.26)$$

Again, this can be rewritten as

$$A_{\text{FB}} = \frac{3}{4} A_e A_\tau. \quad (2.27)$$

Note that  $A_{\text{FB}}$  is quadratic in the asymmetries, and therefore depends only on the absolute value of  $v/a$ .

These three asymmetries can be related in one equation if we examine the angular variation of the tau polarization by applying the Born differential cross-section to equation 2.18 without integrating over  $\cos \theta$ . This gives

$$P_\tau(\cos \theta) = \frac{\frac{d\sigma^+}{d\cos\theta} - \frac{d\sigma^-}{d\cos\theta}}{\frac{d\sigma^+}{d\cos\theta} + \frac{d\sigma^-}{d\cos\theta}}. \quad (2.28)$$

which leads to

$$P_\tau(\cos \theta) = -\frac{(1 + \cos^2 \theta)F_2 + 2 \cos \theta F_3}{(1 + \cos^2 \theta)F_0 + 2 \cos \theta F_1}. \quad (2.29)$$

Note that the average polarization is the ratio of the total cross-sections, not the average of  $P_\tau(\cos \theta)$  over  $\cos \theta$ . Using equations 2.19, 2.23, and 2.26, we can reduce this to an expression in terms of the observables,

$$P_\tau = \frac{\langle P_\tau \rangle (1 + \cos^2 \theta) + \frac{8}{3} A_{\text{FB}}^{\text{Pol}} \cos \theta}{(1 + \cos^2 \theta) + \frac{8}{3} A_{\text{FB}} \cos \theta}. \quad (2.30)$$

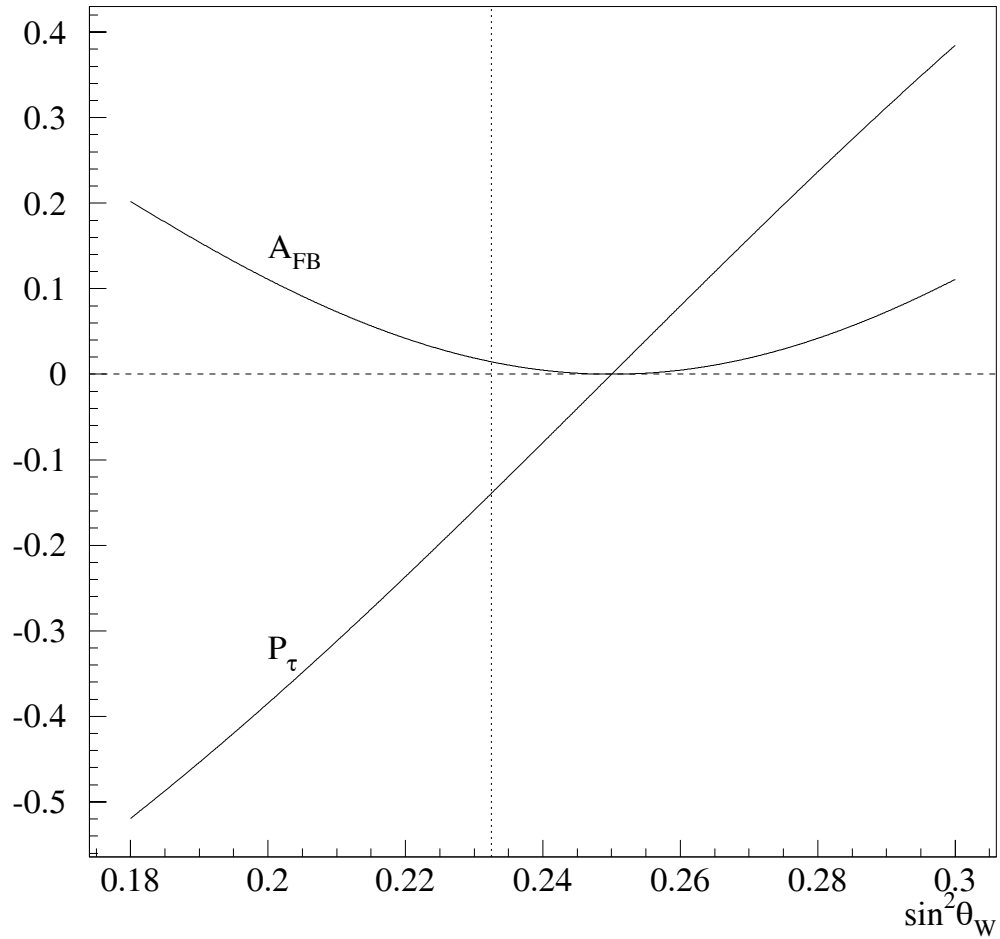


Figure 2.2: This figure shows the variation of the forward-backward asymmetry and the average tau polarization asymmetry as a function of  $\sin^2 \theta_W$ . The vertical dotted line shows the current world average value for the weak mixing angle. We can see that the polarization is much more sensitive to the value of  $\sin^2 \theta_W$ .

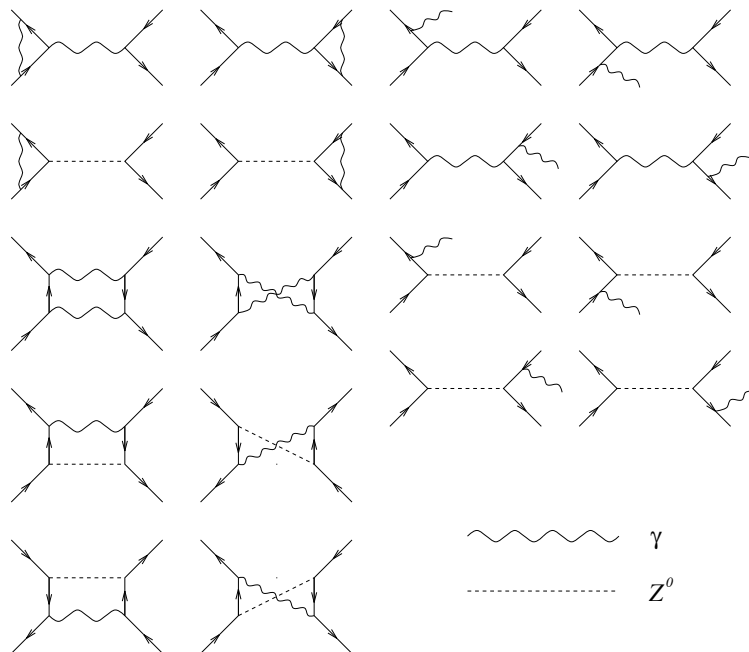


Figure 2.3: Feynman diagrams showing the first order photonic radiative corrections.

Figure 2.2 shows the variations of  $A_{\text{FB}}$  and  $\langle P_\tau \rangle$  about  $\sin^2 \theta_W = \frac{1}{4}$ . Assuming lepton universality to be valid, the variation of  $\langle P_\tau \rangle$  and  $A_{\text{FB}}^{\text{Pol}}$  will be equivalent. We can see that the average tau polarization is much more sensitive to the value of  $\sin^2 \theta_W$  than the forward-backward asymmetry.

## 2.2.2 Radiative Corrections

The tree-level Feynman diagrams are not the only contributions to the cross-section. There are also higher-order diagrams which fall under the general heading of radiative corrections. There are two types of radiative corrections to the  $e^+e^- \rightarrow \tau^+\tau^-$  cross-section which will be discussed below. These are photonic and non-photonic corrections.

Photonic corrections are represented by Feynman diagrams with extra photons added to the tree-level diagram as either a real bremsstrahlung photon or a virtual photon loop. The first order (ie. only one extra photon) diagrams for photonic corrections are shown in figure 2.3. These corrections have a large ( $\sim 30\%$ ) effect on the cross-section, and are

evaluated by convoluting the cross-section with a radiator function which depends on the experimental restrictions of the final state photon. These restrictions include the effects of angular acceptance of these photons (ie. whether they enter the detector, or travel down the beam-pipe) and the energy cutoffs required to reduce electronic noise from the detector. The Born cross-section form (equation 2.13) is unchanged by the photonic corrections, but the form factors  $F_i(s)$  are replaced by the convoluted form factors  $\tilde{F}_i(s)$ . The effect of the photonic corrections (assuming a perfect  $4\pi$  sr acceptance detector) on the total cross-section is shown in figure 2.4. The forward-backward asymmetry and the tau polarization are less sensitive to the photonic corrections (see figure 2.5).

The non-photonic corrections are the other higher order electroweak radiative corrections. In the case of pure QED, the propagator corrections are of the type shown in figure 2.6 but with photon propagators on both sides of the inner loop. Only fermion-antifermion pairs with invariant masses less than the centre-of-mass energy contribute to these corrections. The dominant uncertainty on the calculation is from not knowing the precise masses of the light quarks ( $u, d, s$ ). The QED propagator corrections alter the fine-structure constant,  $\alpha$ , as a function of the centre-of-mass energy by

$$\alpha(s) = \frac{\alpha(0)}{1 - \Delta\alpha(s)}, \quad (2.31)$$

where  $\alpha(M_Z^2)^{-1} = 128.82 \pm 0.12$  [17, 21].

The more general case of the electroweak corrections must take into account the photon and  $Z^0$  propagators. Figure 2.6 shows how the loops allow the photon and  $Z^0$  propagators to mix. Since the  $SU_L(2)$  symmetry is broken, particles more massive than the  $Z^0$  no longer decouple, and the cross-section and asymmetries become dependent on the unknown top quark and Higgs boson masses. Precise measurements at LEP can therefore be used to predict heavy particle masses and are sensitive to new particles not included in the Standard Model.

We will follow Altarelli, et al [18] in our treatment of the electroweak higher order corrections. The mass of the  $Z^0$ , the Fermi constant  $G_\mu$ , and the fine structure constant  $\alpha$  will be taken as inputs since their values are known precisely [19]. The effect of the

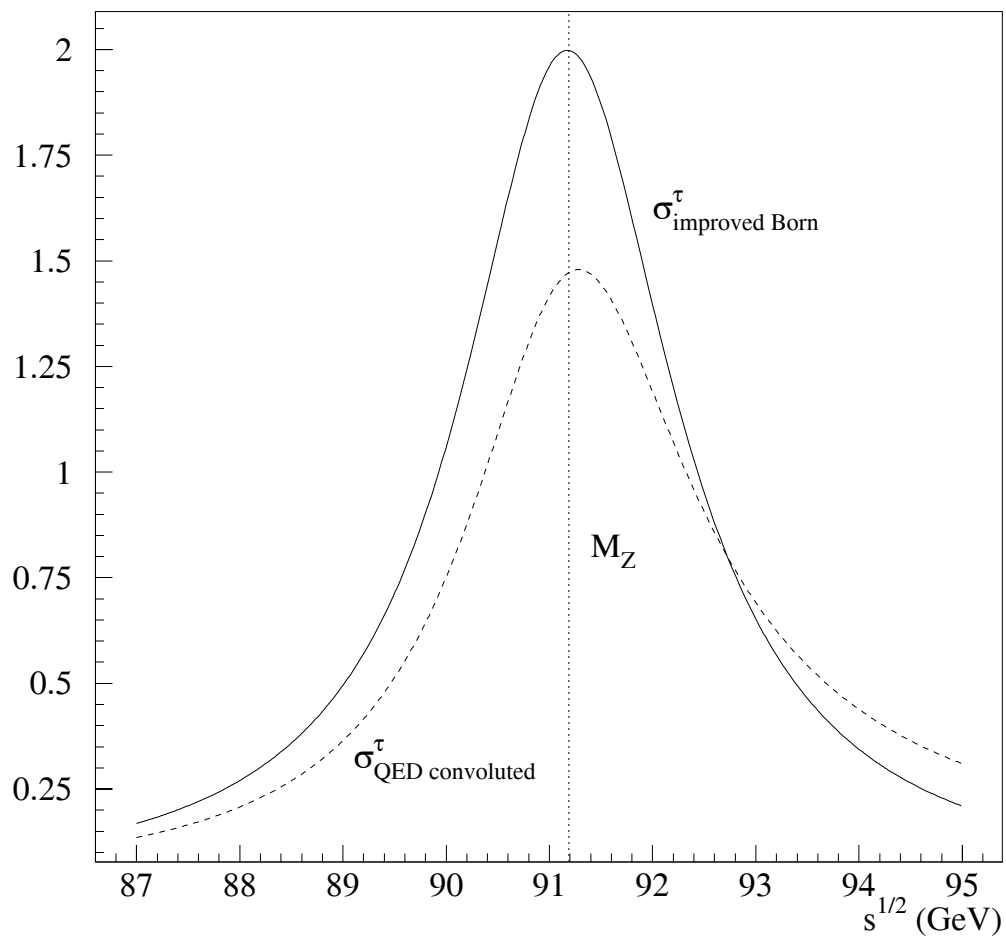


Figure 2.4: Total  $e^+e^- \rightarrow \tau^+\tau^-$  cross-section without photonic corrections (solid line) and with photonic corrections (dashed line).

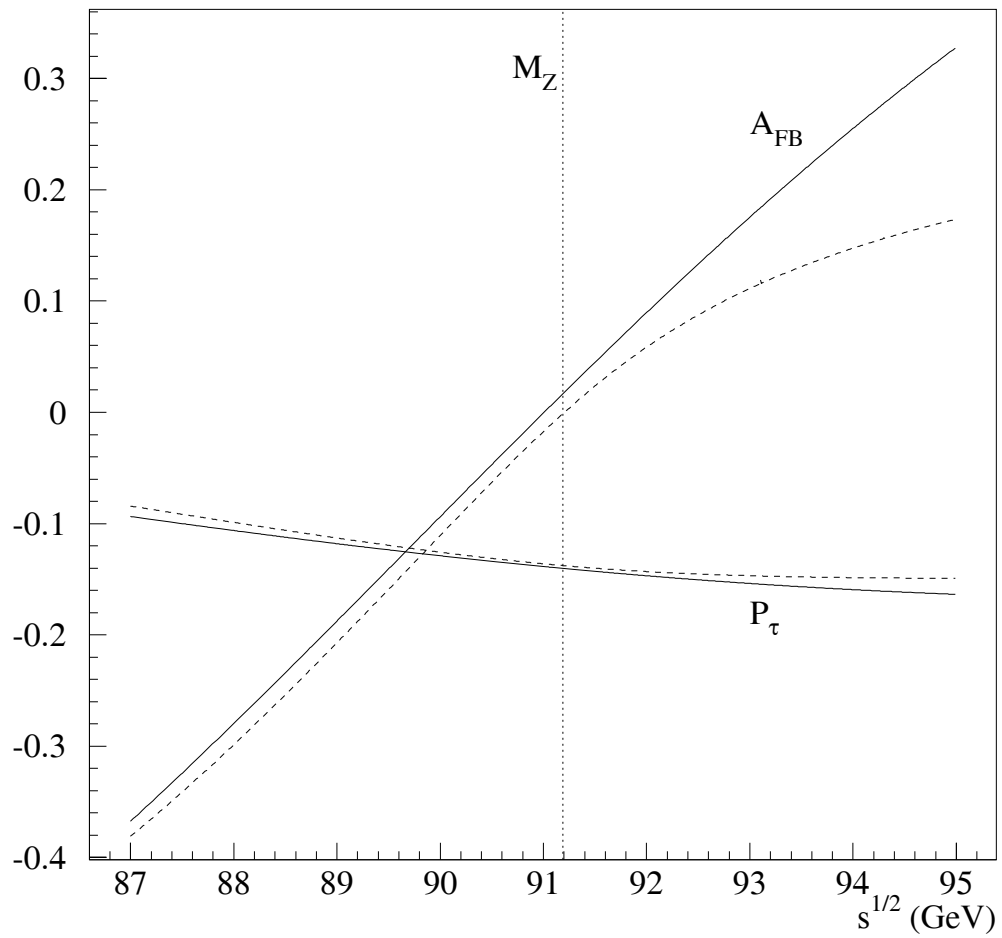


Figure 2.5: This figure shows the forward-backward asymmetry and the tau polarization as a function of centre-of-mass energy without photonic corrections (solid line) and with photonic corrections (dashed line).

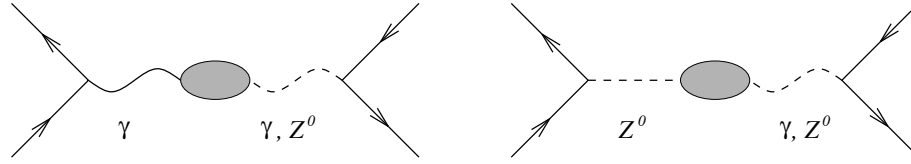


Figure 2.6: This figure shows the Feynman diagrams corresponding to the propagator corrections. The shaded area includes all possible one-loop diagrams involving  $f\bar{f}$  pairs in the loop.

corrections on  $\sin^2 \theta_W$  will be calculated. The discussion will be restricted to leptons and to energies approximately equal to the on-shell mass of the  $Z^0$ .

Combining the Born level equations 1.1, 2.11, 2.12, and 2.5, we can write

$$\cos^2 \theta_W \sin^2 \theta_W = \frac{\pi\alpha}{\sqrt{2}G_\mu M_Z^2 (1 - \Delta r)} \quad (2.32)$$

where the term  $(1 - \Delta r)$  takes into account the higher order corrections. The running of the fine structure constant due only to QED corrections can be factored out,  $(1 - \Delta r) = (1 - \Delta\alpha)(1 - \Delta r_W)$ , where the remaining weak corrections are of order  $\Delta r_W \approx -2 \times 10^{-2}$  [20, 21]. A version of the weak mixing angle, corrected only for pure QED effects, can be defined as

$$\cos^2 \theta_W^0 \sin^2 \theta_W^0 = \frac{\pi\alpha(M_Z^2)}{\sqrt{2}G_\mu M_Z^2}. \quad (2.33)$$

Higher order processes at the vertex modify the point couplings  $v$  and  $a$ . The exchange of photons,  $Z^0$ 's, and  $W$ 's at the vertex is represented in figure 2.7 by the shaded circles. The point couplings can be replaced in the Born approximation by form factors  $\hat{v}$  and  $\hat{a}$  that, near the on-shell mass of the  $Z^0$ , are only weakly energy dependent. The corrections due to the box diagrams are conveniently handled by including them in the vertex corrections. The corrections depend on the type of fermion coupling to the  $Z^0$  but are universal for the charged leptons [20, 22]. When the Born approximation is written with the form factors used as effective couplings and with the overall normalization of  $\chi(s)$  (equation 2.15) corrected for  $\Delta r$ , the new formula is called the Improved Born Approximation. It is sufficiently accurate to describe the results presented in this thesis.

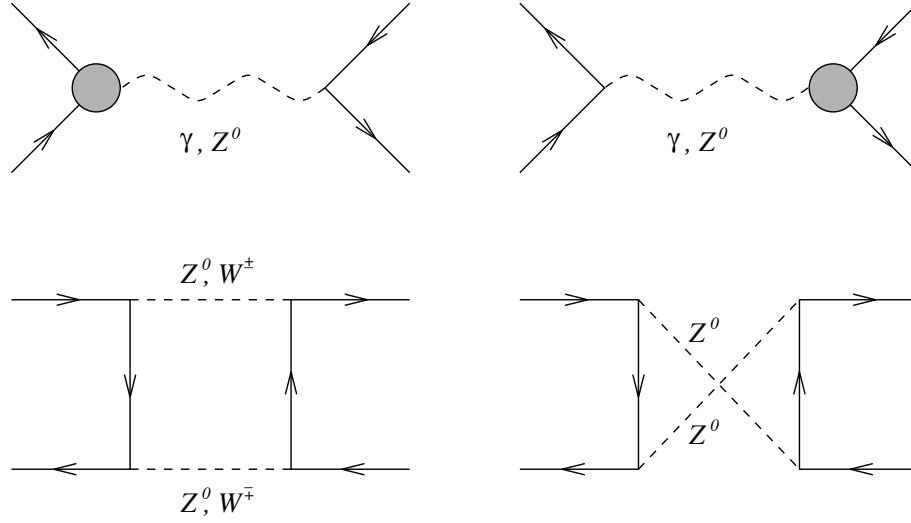


Figure 2.7: This figure shows the Feynman diagrams corresponding to the vertex corrections as well as the box diagrams where neither vector boson is a photon.

The on-shell polarization asymmetry can be written using the effective coupling as

$$A_\ell = \frac{2\hat{v}_\ell/\hat{a}_\ell}{1 + (\hat{v}_\ell/\hat{a}_\ell)^2}. \quad (2.34)$$

The higher order corrections can be put in the form

$$\hat{a}_\ell = \sqrt{\rho} T_f^3 = \left(1 + \frac{\Delta\rho}{2}\right) \left(-\frac{1}{2}\right) \quad (2.35)$$

where the Born level expression 2.7 is modified by  $\sqrt{\rho}$ . At the Born level  $\rho = 1$ , and the radiative corrections are approximated by  $1 + \Delta\rho$ . The ratio of the effective vector and axial couplings is used to define an effective  $\sin^2 \hat{\theta}_W^\ell$ ,

$$\begin{aligned} \frac{\hat{v}_\ell}{\hat{a}_\ell} &= 1 - 4\sin^2 \hat{\theta}_W^\ell \\ \sin^2 \hat{\theta}_W^\ell &= (1 + \Delta\kappa') \sin^2 \theta_W^0. \end{aligned} \quad (2.36)$$

The quantities  $\Delta r_W$ ,  $\Delta\rho$ , and  $\Delta\kappa'$  are dominated by terms depending on  $M_{\text{top}}^2$  and have a logarithmic dependence on  $M_{\text{Higgs}}$ . They are approximately given in the Standard Model by

$$\begin{aligned} \Delta\rho &\approx -\frac{\sin^2 \theta_W^0}{\cos^2 \theta_W^0} \Delta r_W \approx \left(\frac{\cos^2 \theta_W^0 - \sin^2 \theta_W^0}{\cos^2 \theta_W^0}\right) \Delta\kappa' \\ &\approx \frac{3G_\mu M_{\text{top}}^2}{8\pi^2 \sqrt{2}} + \mathcal{O}(10^{-3}). \end{aligned} \quad (2.37)$$

A precise measurement of  $A_\ell$  can thus contribute to fixing the top quark mass. If the top quark mass is known, we can search for inconsistencies in the Standard Model.

All measured asymmetries discussed in the previous section can be written in terms of  $\sin^2 \hat{\theta}_W^\ell$ . Thus, this quantity is an important tool for comparing different measurements.

## 2.3 Tau Polarization Measurement

We have shown that the tau polarization is an effective quantity for testing the neutral current in the Standard Model. This section discusses the method used to measure the tau polarization. As mentioned earlier, the polarization of the tau must be determined from the angular distribution of its decay products. However, the sensitivities of the various final states in the tau decay to the tau polarization are not equal. In this section, we will show how the  $\tau^-$  polarization can be measured using the  $\tau^- \rightarrow \rho^- \nu_\tau$  channel<sup>1</sup>.

The angular distribution of the  $\tau^-$  decay products ( $\rho^-, \nu_\tau$ ) in the tau centre-of-mass frame is given by

$$\frac{1}{N} \frac{dN}{d\cos\theta^*} = \frac{1}{2}(1 + \alpha\langle P_\tau \rangle \cos\theta^*), \quad (2.38)$$

where  $\alpha$  is a kinematic factor. For a spin zero particle,  $\alpha = 1$ , but for a spin 1 particle like the  $\rho^-$ , this factor is given by

$$\begin{aligned} \alpha &= \frac{m_\tau^2 - 2m_\rho^2}{m_\tau^2 + 2m_\rho^2} \\ &= 0.46. \end{aligned} \quad (2.39)$$

The factor alpha arises from the mixture of the different possible  $\rho^-$  helicity states in the data sample. Since the  $\rho^-$  is a spin 1 particle, it has three possible helicity states ( $h_\rho = 0, \pm 1$ ). Conservation of helicity in the  $\tau^- \rightarrow \rho^- \nu_\tau$  decay means that the  $\rho^-$  is either in an  $h_\rho = +1$  or  $h_\rho = 0$  helicity state, as shown in figure 2.8.

The angle  $\cos\theta^*$  in equation 2.38 is the angle between the direction of the  $\rho^-$  in the  $\tau^-$  centre-of-mass and the direction of the  $\tau^-$  in the lab frame. This angle can be calculated

---

<sup>1</sup>Throughout the rest of this thesis, when the decay of the  $\tau^-$  is discussed, the charge-conjugate decay of the  $\tau^+$  is also implied.

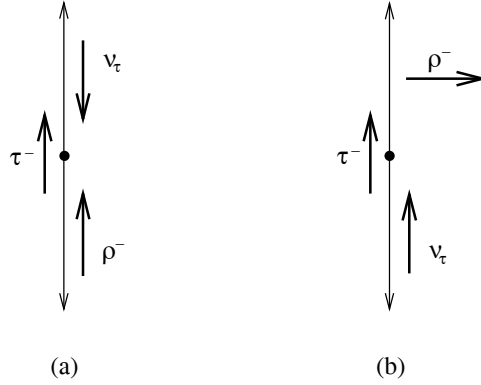


Figure 2.8: This figure shows the two possible spin orientations of the  $\rho^-$ . The sum of the spins of the  $\nu_\tau$  and the  $\rho^-$  must equal the spin of the  $\tau^-$ . Diagram (a) represents the spin combination  $|\frac{1}{2}, \frac{1}{2}\rangle_\tau = |\frac{1}{2}, -\frac{1}{2}\rangle_{\nu_\tau} |1, 1\rangle_\rho$ , and diagram (b) represents the spin combination  $|\frac{1}{2}, \frac{1}{2}\rangle_\tau = |\frac{1}{2}, \frac{1}{2}\rangle_{\nu_\tau} |1, 0\rangle_\rho$ .

in terms of the rest masses and energies of the  $\rho^-$  and  $\tau^-$ , where  $E_\tau$  is approximated by the beam energy, as

$$\cos \theta^* = \frac{(2E_\rho/E_{\text{beam}} - 1)m_\tau^2 - m_\rho^2}{\beta_\tau(m_\tau^2 - m_\rho^2)}. \quad (2.40)$$

Figure 2.9 shows the one-dimensional theoretical distribution for the maximum and minimum values of the polarization ( $\langle P_\tau \rangle = \pm 1$ ) and an estimate for the Standard Model value ( $\langle P_\tau \rangle = -0.14$ ) when one assumes  $\sin^2 \theta_W = 0.2325$  [50].

The sensitivity of the angular distribution to the polarization can be enhanced by examining the subsequent decay of the  $\rho^-$ . If we look at the decay  $\rho^- \rightarrow \pi^- \pi^0$ , we can calculate the angle,  $\psi$ , between the direction of the  $\pi^-$  in the  $\rho^-$  rest frame and the direction of the  $\rho^-$  in the  $\tau^-$  rest frame as

$$\cos \psi = \frac{2m_\rho^2 E_{\pi^-} - (m_\rho^2 + m_{\pi^-}^2 - m_{\pi^0}^2)E_\rho}{p_\rho \{ [m_\rho^2 - (m_{\pi^-} - m_{\pi^0})^2][m_\rho^2 - (m_{\pi^-} + m_{\pi^0})^2] \}^{\frac{1}{2}}}. \quad (2.41)$$

The distribution for the two dimensional space is then given by [23]

$$W(\theta^*, \psi) = \frac{3}{8(m_\tau^2 + 2m_\rho^2)} \times \left\{ (1 + P_\tau)W^+(\theta^*, \psi) + (1 - P_\tau)W^-(\theta^*, \psi) \right\}, \quad (2.42)$$

where

$$W^\pm(\theta^*, \psi) = w_1^\pm(\theta^*)h_1(\psi) + w_0^\pm(\theta^*)h_0(\psi)$$

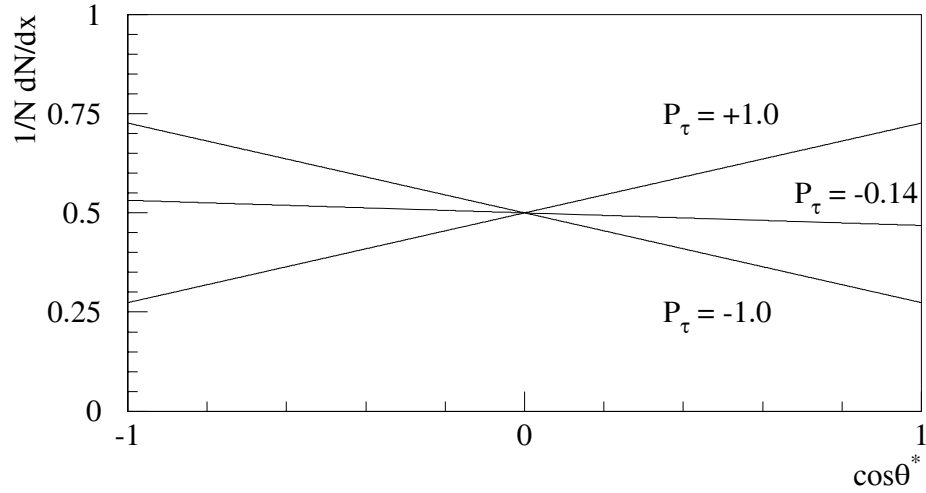


Figure 2.9: This figure shows the angular distribution of  $\tau^- \rightarrow \rho^- \nu_\tau$  events in  $\cos \theta^*$  for three values of the polarization,  $\langle P_\tau \rangle$ . The maximum slope (ie. for  $\langle P_\tau \rangle = \pm 1$ ) is less than one due to the dilution from the two allowed spin orientations of the  $\rho^-$ . The Standard Model value for the polarization is  $\langle P_\tau \rangle = -0.14$ .

$$\begin{aligned}
 w_0^+ &= \left[ m_\tau \cos \eta \cos \frac{\theta^*}{2} + m_\rho \sin \eta \sin \frac{\theta^*}{2} \right]^2 \\
 w_0^- &= \left[ m_\tau \cos \eta \sin \frac{\theta^*}{2} - m_\rho \sin \eta \cos \frac{\theta^*}{2} \right]^2 \\
 w_1^+ &= \left[ m_\tau \cos \eta \cos \frac{\theta^*}{2} - m_\rho \sin \eta \sin \frac{\theta^*}{2} \right]^2 + m_\rho^2 \sin^2 \frac{\theta^*}{2} \\
 w_1^- &= \left[ m_\tau \cos \eta \cos \frac{\theta^*}{2} + m_\rho \sin \eta \sin \frac{\theta^*}{2} \right]^2 + m_\rho^2 \cos^2 \frac{\theta^*}{2} \\
 h_0 &= 2 \cos^2 \psi \\
 h_1 &= \sin^2 \psi,
 \end{aligned}$$

and  $\eta$  is the Wigner rotation angle [24] given by

$$\cos^2 \eta = \frac{[(m_\tau^2 - m_\rho^2) + (m_\tau^2 + m_\rho^2)\beta_\tau \cos \theta^*]^2}{[(m_\tau^2 + m_\rho^2) + (m_\tau^2 - m_\rho^2)\beta_\tau \cos \theta^*]^2 - 4m_\tau^2 m_\rho^2 (1 - \beta_\tau^2)}. \quad (2.43)$$

The two dimensional angular distributions  $(\cos \theta^*, \cos \psi)$  for three values of the polarization are shown in figure 2.10. The additional sensitivity of the distribution to variation in  $\cos \psi$  can clearly be seen.

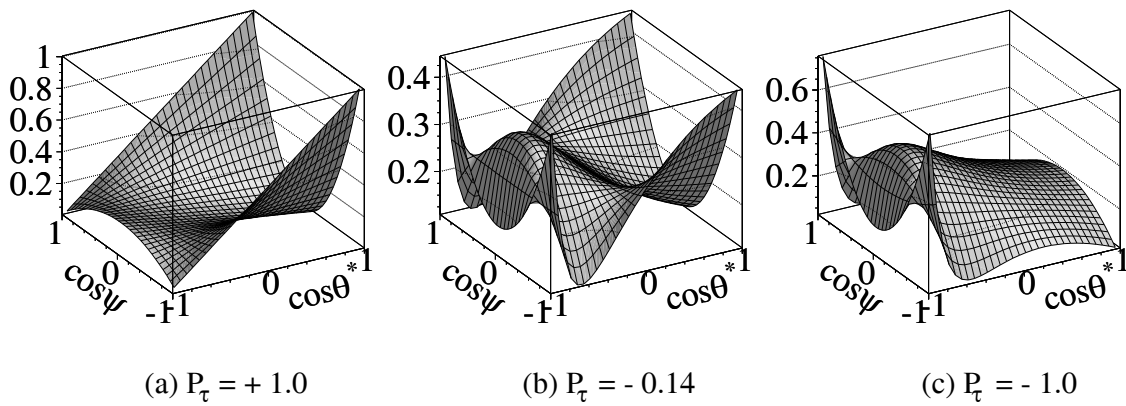


Figure 2.10: This figure shows the angular distribution of  $\tau^- \rightarrow \rho^- \nu_\tau$  events in  $(\cos\theta^*, \cos\psi)$  for three values of the polarization,  $\langle P_\tau \rangle$ . The sensitivity to the value of the polarization is improved over the one-dimensional distribution with the addition of the information from the  $\rho^- \rightarrow \pi^- \pi^0$  decay.

# Chapter 3

## The Experimental Facility

In this chapter, the experimental facility used for this analysis will be described. The  $e^+e^-$  annihilations are produced in the Large Electron Positron (LEP) collider facility at CERN just outside of Geneva, Switzerland. The first section will describe the design and operating parameters of the LEP collider, including an overview of the accelerator complex. The second section will include a general description of the OPAL detector which was used to collect the data for the analysis. The performance characteristics of the detector components relevant to the analysis presented in this thesis will be described in detail.

### 3.1 The LEP Collider

The LEP collider consists of an injector chain, which produces and accelerates the electrons and positrons before injection into the main ring, and the main ring, which accelerates the particles to a centre-of-mass energy suitable for  $Z^0$  physics.

#### 3.1.1 LEP Injector Chain

The LEP injector chain [25] makes use of two of CERN's most famous accelerators: the Proton Synchrotron (PS), which was used in the discovery of neutral weak currents in the early 1970's [10], and the Super Proton Synchrotron (SPS), which was used in the early 1980's in the discovery of the  $W^\pm$  and  $Z^0$  particles. Figure 3.1 shows a schematic diagram of the LEP injector chain. Positrons are produced by directing electrons from a 200 MeV

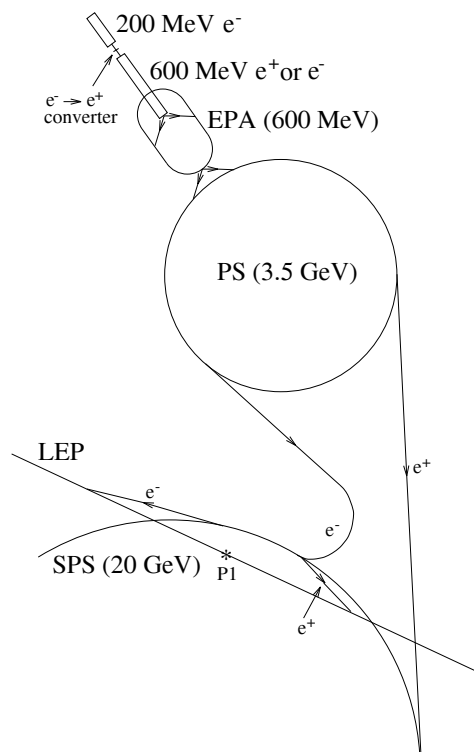


Figure 3.1: This figure shows a schematic of the injection scheme for LEP.

linac onto a converter target. These positrons, and electrons which are produced by a separate low-intensity electron gun near the converter target, are accelerated in a 600 MeV linac and collected in the Electron-Positron Accumulator (EPA). The EPA acts as a buffer between the high frequency linacs and the slower cycling synchrotrons.

After accumulation in the EPA, the electrons and positrons are injected into the PS where they are accelerated to 3.5 GeV and then transferred to the SPS which further accelerates the particles to 20 GeV. Four equally spaced bunches are then injected into the LEP ring, with typically 400  $\mu\text{A}$  accumulated in each bunch. The final acceleration to the working energy (92 GeV for this thesis) is done in the LEP ring.

### 3.1.2 LEP Main Ring

The main LEP ring [26] is 26.66 km in circumference and is in the shape of an octagon with rounded corners (see figure 3.2). The ring is located in a tunnel between 100 m and 150 m underground and is tilted at an angle of 1.42% in order to avoid the geological difficulties of tunneling deep under the Jura mountains west of the site. There are eight beam crossing points, of which only four are instrumented with the ALEPH, OPAL, DELPHI, and L3 detectors.

The collider was designed to provide a peak luminosity of  $1.6 \times 10^{31} \text{ cm}^{-2} \text{ s}^{-1}$  at a current of 3 mA. The original design had four bunches of electrons and four bunches of counter-rotating positrons with  $4 \times 10^{11}$  particles in each bunch circulating within the ring every 88.9  $\mu\text{s}$ .

In 1992, the accelerator was upgraded to operate with eight bunches circulating in each direction using the pretzel scheme [27]. The collider began operation in the fall of 1989, and has provided excellent running conditions for the four experiments. The integrated luminosity delivered to the experiments is shown in figure 3.3 for each year of operation.

## 3.2 The OPAL Experiment

This section contains a description of the components of the OPAL detector required for this analysis. A full description of the OPAL detector is presented in [28] and references

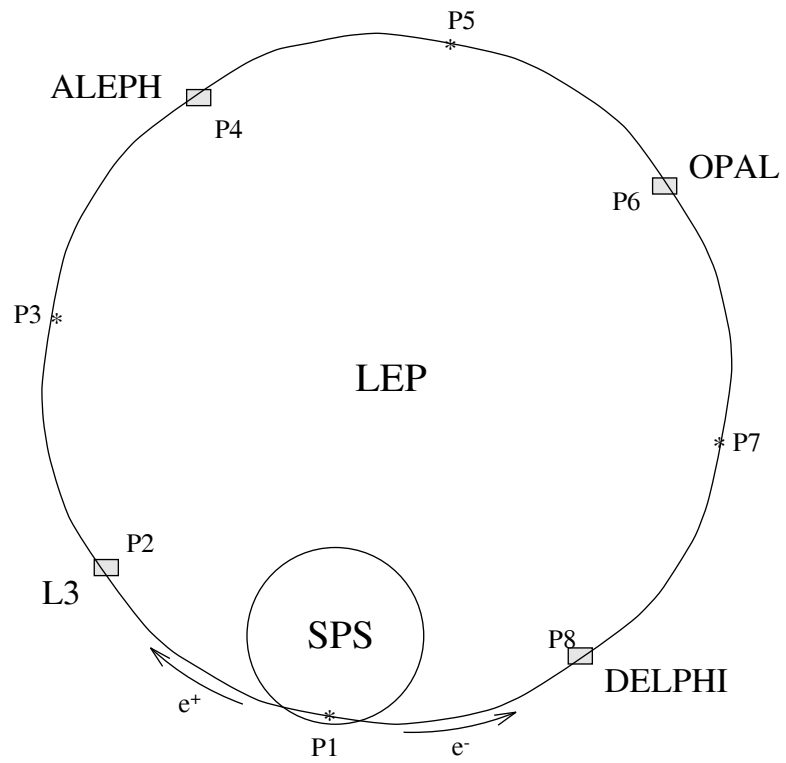


Figure 3.2: This figure shows a schematic of the LEP main ring with the locations of the four experimental areas indicated.

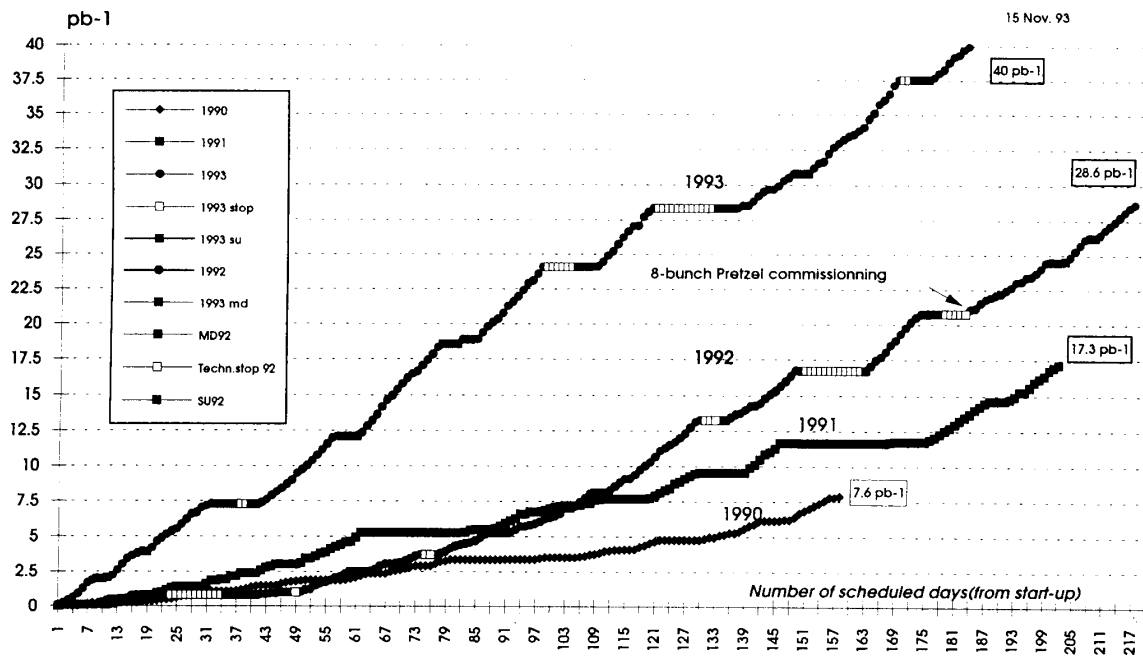


Figure 3.3: This figure shows the LEP delivered luminosity up to the end of the 1993 running period.

therein. The OPAL detector (see figure 3.4) consists of several nested subdetectors, each of which is optimized for one or more specific tasks. There are three basic detector groups. The inner tracking chambers consist of a silicon microvertex detector (SI), a vertex drift chamber (CV), a jet tracking chamber (CJ) and a  $z$ -chamber (CZ). The tracking detectors are situated in a 4.36 m diameter solenoidal magnet which provides a 0.435 T magnetic field oriented along the electron direction of motion in the beam pipe. The curvature of charged tracks in the field is measured in the tracking chambers to determine charged particle momenta. Surrounding the tracking detectors and magnet are the time-of-flight counters (barrel - TB, and endcap - TE) and the calorimeters (total energy absorbing detectors). The calorimeters are composed of an electromagnetic calorimeter (barrel - EB, endcap - EE), and a hadron calorimeter (barrel - HB, endcap - HE, and poletip - HT). The muon detector (barrel - MB, endcap - ME) surrounds the rest of the detector components.

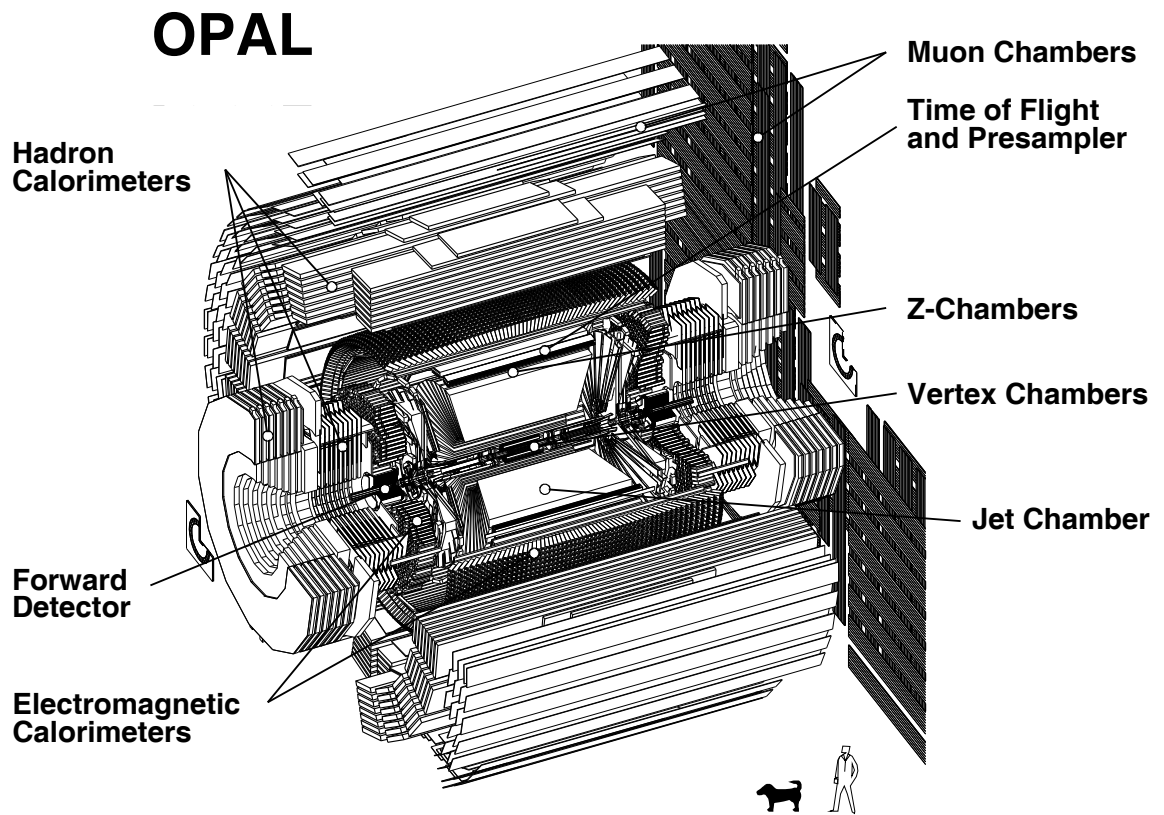


Figure 3.4: Cutaway view of the OPAL detector showing the major subdetector components.

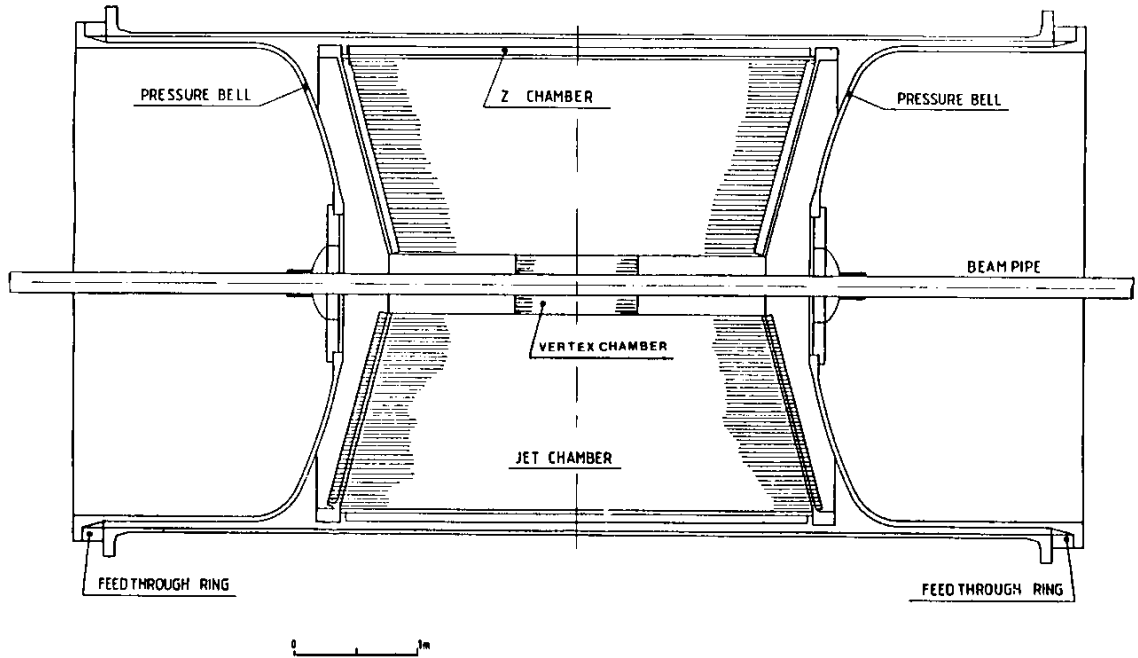


Figure 3.5: This figure shows a schematic of the central tracking detectors (the silicon detector is not shown here). The vertex chamber, jet chamber, and  $z$ -chamber are contained within the pressure vessel which maintains a constant 4 bar pressure.

### 3.2.1 The Inner Tracking Chamber

The inner tracking chamber detectors (figure 3.5) are used for measuring the position and momentum of individual charged particles produced in the  $Z^0$  decay. The innermost detector is a silicon microvertex detector which was installed during the 1991 LEP run. The information from this detector is not used in this analysis to maintain consistency in the data sample. The next three detectors, which perform the tracking measurements, are operated in a common gas mixture (88.2% argon, 9.8% methane, and 2.0% isobutane) which is kept at a constant 4 bar pressure chosen to optimize particle separation using  $dE/dx$  while minimizing multiple scattering and diffusion effects [32].

The first of these three detectors is a 1m long drift chamber [29] (see figure 3.6) which is used to locate decay vertices with high precision in the  $r$ - $\phi$  plane, and to aid in momentum resolution. The detector is a cylinder 47 cm in diameter with an inner layer of thirty six axial wire cells, each composed of twelve anode sense wires, and an outer layer

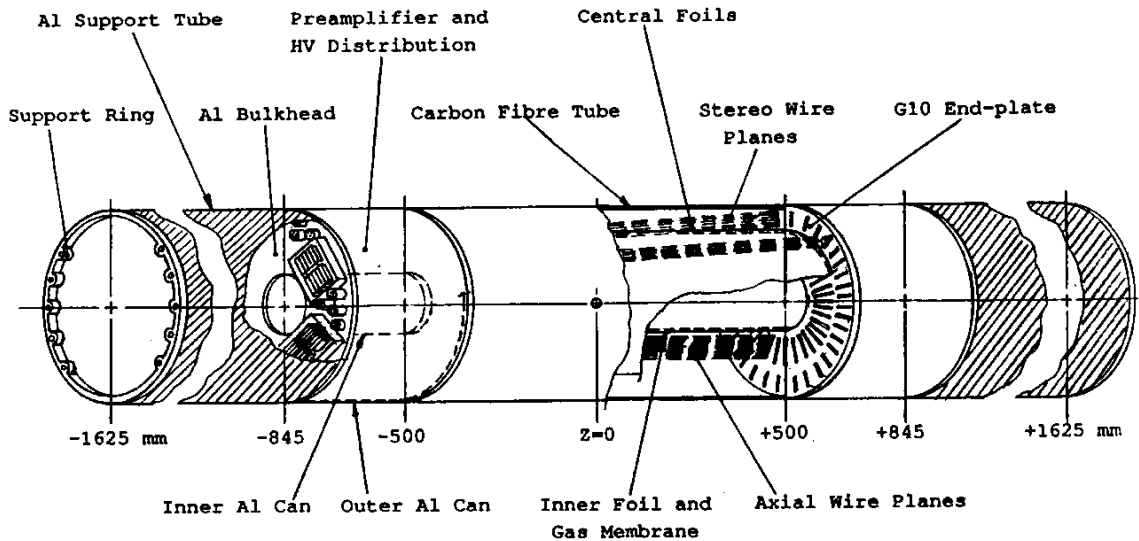


Figure 3.6: This figure shows a schematic of the vertex drift chamber. The inner wire planes return information on the axial position ( $r$ - $\phi$  position) of particles as they traverse the detector, and the outer wire planes return stereo information ( $z$  position) for the particles.

of thirty six stereo cells inclined at  $4^\circ$ , each with six anode wires. The resolution provided by the axial cells is  $50 \mu\text{m}$  in the  $r$ - $\phi$  plane. A coarse determination of the  $z$ -coordinate is made by a measurement of the time difference between signals at either end of the anode wire, and by examining the  $z$  information produced from the stereo wires. The resolution in  $z$  is  $\approx 4 \text{ cm}$ .

The primary tracking measurement is made within a large drift chamber (jet chamber) [30] surrounding the vertex detector. The jet chamber is designed to provide good spatial resolution for identifying individual tracks in a high multiplicity environment. The detector, about 4m long and with inner diameter 0.51 m and outer diameter 3.67 m, is divided into 24 sectors in  $\phi$ , each of which has 159 wires parallel to the beam pipe and forming a radial plane within the sector. True three-dimensional information is produced for each particle as it passes through the jet chamber from the wire position ( $r$ ), the drift time ( $\phi$ ), and charge division along the wires ( $z$ ). In the  $r$ - $\phi$  plane, the jet chamber provides an average resolution of  $135 \mu\text{m}$  over all drift distances. In the  $r$ - $z$

plane, the resolution is  $\sigma_z = 2.5$  cm for  $Z^0 \rightarrow \mu^+ \mu^-$  and 6.2 cm for  $Z^0 \rightarrow$  hadrons. The momentum resolution of the jet chamber is  $\sigma_p/p^2 = 1.5 \times 10^{-3} (\text{GeV}/c)^{-1}$  and  $\sigma_{p_T}/p_T = \sqrt{(0.02)^2 + (0.0015p_T)^2}$  [32].

The final component of the inner tracking chamber is the  $z$ -chamber [31] which is a series of detectors designed to make precise measurements of the  $z$  coordinate of charged particles as they leave the jet chamber. The  $z$ -chamber consists of 24 drift chambers forming a cylinder with a diameter of 3.85 m. Each drift chamber is divided into 8 square ( $50 \text{ cm} \times 50 \text{ cm} \times 59 \text{ mm}$  thick) segments in  $z$ , giving a maximum drift distance of 25 cm in the  $z$  direction. The  $z$ -resolution was measured to be  $175 \mu\text{m}$  for the full 25 cm drift, and the  $r$ - $\phi$  resolution was measured to be 6 mm.

The combined resolution using these three detectors has been measured [28] to be  $\sigma_{r-\phi} = 75 \mu\text{m}$ , and  $\sigma_z = 2$  mm with (2.7 cm without) the stereo wire information of the vertex detector.

### 3.2.2 Solenoidal Magnet and Time Of Flight

The magnet consists of a solenoidal coil and an iron return yoke. The coil is situated around the inner tracking chamber and provides a uniform magnetic field of 0.435 T, sufficient for accurate momentum measurements to be made in the inner chambers. The return yoke forms the basis for the hadron calorimeter and will be described later.

The magnet is surrounded by the barrel time-of-flight detector system. The 160 scintillation counters, at an average radius of 2.36 m, which comprise this detector provide a timing resolution of 460 ps for muons and a  $z$ -resolution of 5.5 cm. In this analysis the time-of-flight detector is used for cosmic ray rejection. A cosmic ray muon entering the detector vertically has an expected flight time across the detector of 7.87 ns, well above the resolution of the detector.

### 3.2.3 Calorimeters

Surrounding the inner chamber and time-of-flight detector is an electromagnetic-shower presampler followed by two calorimeters, the electromagnetic calorimeter (ECAL) and

the hadron calorimeter (HCAL). The electromagnetic calorimeter is optimized to measure the energy deposited by electrons and photons in the form of electromagnetic showers, and the hadron calorimeter is used to measure the energy deposited by hadronic showers which, on average, extend beyond the ECAL.

Most electromagnetic showers start in the material (about 2 radiation lengths,  $X_0$ , mostly from the coil and pressure vessel) in front of the ECAL. The early showering degrades the energy resolution in the calorimeter. A shower presampler detector (PB) was designed to partially compensate for this by sampling the amount of electromagnetic activity in the shower before it reaches the calorimeter [33]. For this analysis, an average energy correction is applied instead of an event by event presampler correction.

The electromagnetic calorimeter [34] is made up of three separate segments: a barrel ( $|\cos \theta| < 0.82$ ) segment and two endcap ( $0.81 < |\cos \theta| < 0.98$ ) segments. For this analysis, only those events in the barrel region are used. Some events may deposit energy near the boundary region between the barrel and one of the endcap detectors. In this case, the endcap detector is examined to see if any energy has spilled over into the endcap region.

The barrel electromagnetic calorimeter consists of 9440 lead glass blocks in a cylindrical array, with 59 blocks in the  $z$  direction and 160 blocks in  $\phi$ . The blocks are  $24.6 X_0$  long with  $10 \text{ cm} \times 10 \text{ cm}$  faces which, at the inner radius of the detector of 2455 mm, corresponds to an angular coverage of approximately  $40 \text{ mr} \times 40 \text{ mr}$ . The blocks are oriented so that they point towards the interaction region to increase the probability that a particle will only pass through one block, and with a slight offset to minimize the probability that a particle will pass through the crack between two blocks (see figure 3.7). The energy resolution of the ECAL was measured to be [35]  $\sigma_E/E = 1.8\% + 23\%/\sqrt{E}$ .

The hadronic calorimeter is made from the iron return yoke of the magnetic coil, instrumented to measure the hadronic energy of particles emerging from the electromagnetic calorimeter. There are five sections which make up the hadron calorimeter: the barrel ( $|\cos \theta| < 0.81$ ), two endcap ( $0.81 < |\cos \theta| < 0.91$ ), and two pole-tip ( $0.91 < |\cos \theta| < 0.99$ ) detectors. In this analysis, only the barrel hadron calorimeter is

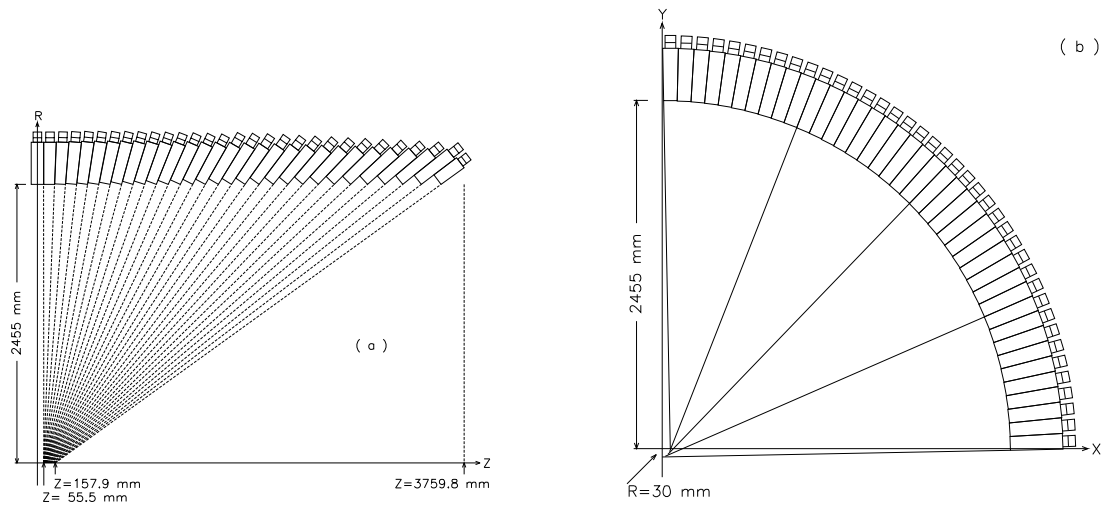


Figure 3.7: This figure shows the orientation of the lead glass blocks in the electromagnetic calorimeter. (a) shows that the lead glass blocks point slightly away from the  $z$ -coordinate of the interaction point; (b) shows that the blocks also point away from the  $r$ - $\phi$  vertex position.

used to help in the rejection of muon events.

The iron of the return yoke is divided into eight 10 cm thick slabs which provides over 4 interaction lengths of absorber material. These slabs are interleaved with nine 25 mm thick streamer tubes which act as the active material of the calorimeter. The energy resolution is estimated to be  $\sigma_E/E = 120\%/\sqrt{E}$ .

### 3.2.4 Muon Chambers

The muon chambers are designed to detect muons emerging from the hadron calorimeters and, in this analysis in particular, to provide muon pair rejection. The inner detectors, with 7 or more interaction lengths of material, prevent most (99.9%) charged pions from entering the muon detectors. Muons with energy above about 3 GeV do not stop in the hadron calorimeter but are detected with essentially 100% efficiency in the muon detector. There are, however, processes in which a hadron could fake a muon: in-flight decay of the hadron to a muon, “sneakthrough”, where the hadron fails to interact strongly in the hadron calorimeter, or “punchthrough”, where the hadron interacts strongly in the hadron

calorimeter but secondary particles emerge into the muon chambers.

The muon chambers are divided into a barrel detector and two endcap detectors with only the barrel detector used in this analysis. The barrel muon detector (MB) covers the region  $|\cos \theta| < 0.72$  with 110 drift chambers, each 1.2 m wide  $\times$  90 mm deep, and with lengths varying between 10.4 m and 6.0 m (the shorter lengths are required to accommodate the magnet support structure). For  $|\cos \theta| < 0.68$ , there are four layers of detector material, while between  $0.68 < |\cos \theta| < 0.72$  there are one or more layers. The  $\phi$ -coordinate of a muon passing through the detector is measured to an accuracy of better than 1.5 mm, and the  $z$ -coordinate to an accuracy of 2 mm.

### 3.2.5 Trigger System

Each subdetector component provides independent signals which are examined for each beam-collision to see if an interesting event is present. The primary event selection was performed by the trigger system [36] which makes use of a high level of redundancy and fine detector segmentation to provide good acceptance for studies of  $Z^0$  decays. Two types of signals are used by the central trigger processor to make a decision on whether the event represents a potentially interesting physics process. Each subdetector provides ‘direct’ trigger signals, representing quantities such as total energy or track counts which require relatively high thresholds before being sent. Also, in order to allow for lower thresholds, the entire detector is subdivided into 144  $\theta$ - $\phi$  cells (6 bins in  $\theta$  and 24 bins in  $\phi$ ) The information from each subdetector in each cell is combined, allowing spatial coincidences between the subdetectors to be identified.

The central trigger logic processor uses signals from the vertex chamber, the jet chamber, the time-of-flight detector, the electromagnetic barrel and endcap calorimeters, and the barrel and endcap muon chambers. For this analysis, trigger signals were required from either the jet chamber or the electromagnetic calorimeter to accept the event.

The jet chamber trigger provides the central trigger processor with information on the number of hits in three regions of the detector (two rings of 12 adjacent wires near the inner radius and one ring near the outer radius), as well as the number of tracks that could

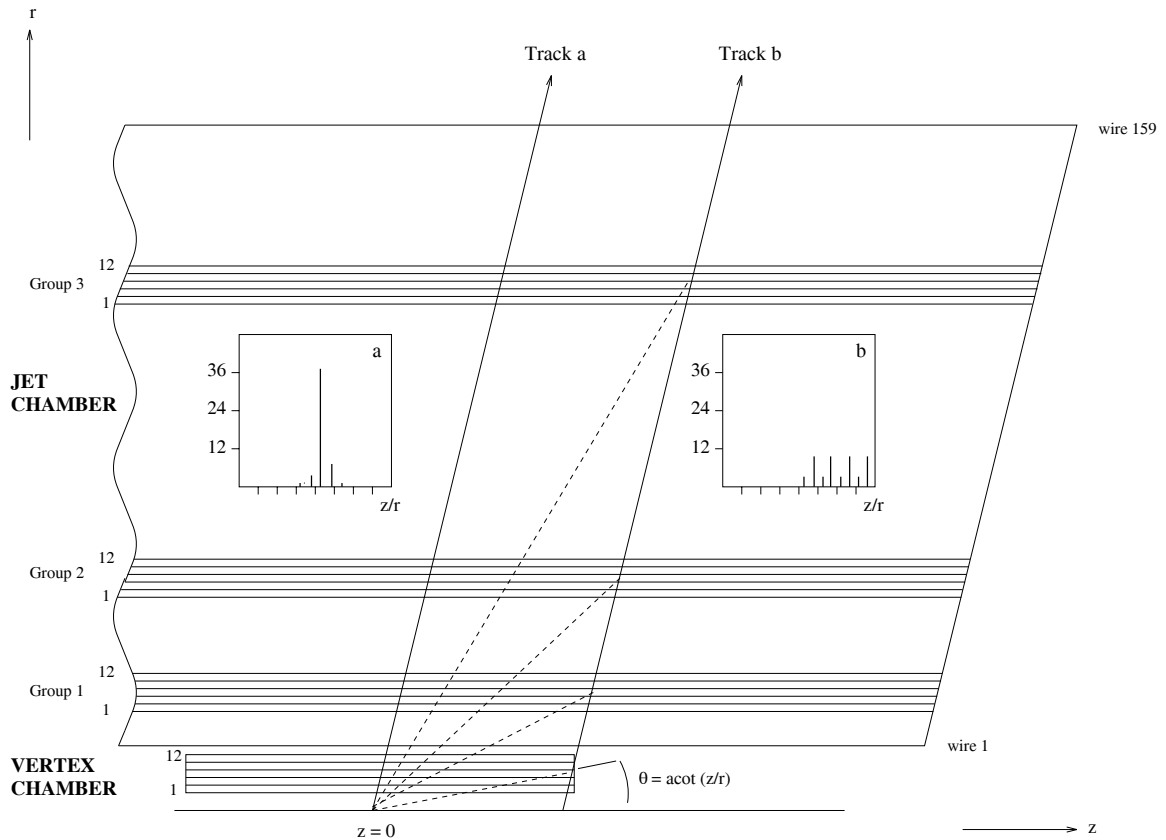


Figure 3.8: This figure shows the principle of the track finding in the  $r$ - $z$  plane of the jet chamber. Histogram (a) shows the variable  $z/r$  would look like for a track originating at the origin. Histogram (b) shows this variable for a track not originating at the origin. The values of  $z/r$  at each jet chamber ring would be different for this track.

be identified in the detector. Charged tracks are identified by looking for tracks with a relatively constant  $\theta$  value. A peak is identified in a histogram of hits in  $z/r$  and adjacent  $\theta$  and  $\phi$  bins are summed to allow for curvature of the track due to the magnetic field. A track is identified if a coincident peak is found in all three rings of the jet chamber. This is shown in figure 3.8 where the track on the left shows coincidences in  $z/r$  on all three rings of the jet chamber while the track on the right does not. Within the barrel region, the track identification trigger rate was approximately 0.4 Hz with 98.5 % efficiency (as measured from  $e^+e^- \rightarrow \mu^+\mu^-$  events triggered independently of the track trigger).

The electromagnetic calorimeter trigger is based on comparing analogue sums of

energy in different regions of the calorimeter against a ‘low’ and a ‘high’ energy threshold. The thresholds for the total energy in the barrel detector are 4 GeV and 7 GeV. For each of the endcap detectors, the total energy thresholds are 4 GeV and 6 GeV. In addition, thresholds of 1 GeV and 2.6 GeV are set for each of the  $\theta$ - $\phi$  cells in the barrel region, and 1 GeV and 3.0 GeV for the cells in the endcap regions. The trigger rate from the barrel trigger was about 0.1 Hz for the high threshold events and about 10 Hz for the low threshold events with essentially 100 % efficiency.

### 3.2.6 Filtering and Online Data Processing

Once the trigger logic has identified an event with potentially interesting physics, the data are read out from each of the subdetectors and transferred to an *event builder* where the full event record is assembled. The event is then passed to a filter processor which performs a fast analysis to provide preliminary event type classification ( $q\bar{q}$  pair, lepton pair, background, etc.) for online monitoring of the data quality. The filter processor writes out the events into 20 MB files which are then released to the online data reconstruction system. The filter processor is also used to reject events which have been classified as background events (ie. those events which are not physically interesting), which accounts for approximately 90% of the data selected by the trigger logic.

The events are processed immediately by the online data reconstruction system. The data reconstruction program consists of several subprocessors, one for each subdetector plus others to perform matching between the subdetectors. The quantities measured in the detector are converted into calibrated energies and vector momenta. The events are then ready to be used for analyses.

# Chapter 4

## Data Selection

In this chapter we discuss the selection of the events used in this analysis. The first section contains a description of the OPAL data and the Monte Carlo simulated data samples that were used to estimate efficiencies and backgrounds in the data sample. The second section briefly describes the selection of tau pair decays of the  $Z^0$  from the full data set. The third section describes in detail the final selection of the  $\tau^- \rightarrow \rho^- \nu_\tau$  events from the tau pair sample.

### 4.1 Event Samples

This section briefly discusses the two types of event samples used in this analysis: events collected by the OPAL detector and simulated (Monte Carlo) events.

#### 4.1.1 OPAL Event Sample

The data used in this analysis were taken during the 1991 and 1992 running periods of the OPAL detector. The integrated luminosity collected by the OPAL detector was approximately  $14 \text{ pb}^{-1}$  [37] in 1991 and  $25 \text{ pb}^{-1}$  [38] in 1992, with about 93% of the data taken on the  $Z^0$  peak ( $E_{\text{CM}} = 91.2 \text{ GeV}$ ) and the rest taken at 1 GeV increments between 88.2 GeV and 94.2 GeV.

It is important that only reliably measured quantities be used for the selection criteria. The subdetectors used to make the measurements are required to be in good running order during the data taking period, and the detectors used in the trigger logic must be in an

	CV	CJ	TB	PB	EB	EE	HB	MB
Detector	3	3	3	3	3	3	3	3
Trigger	-	2	-	-	2	3	-	-

Table 4.1: Detector and trigger status levels required for the tau selection. Appropriate levels were developed by the working groups responsible for each detector subsystem.

Event type	Generator	Events Generated
$e^+e^- \rightarrow \tau^+\tau^-$	KORALZ3.8 [39]	293000
$e^+e^- \rightarrow q\bar{q}$	JETSET [40]	993599
$e^+e^- \rightarrow e^+e^-$	BABAMC [41]	100000
$e^+e^- \rightarrow \mu^+\mu^-$	KORALZ3.8 [39]	200000
$e^+e^- \rightarrow e^+e^- X$	Two-photon generator [42]	100000

Table 4.2: This table shows the generators used to generate the Monte Carlo event samples.

appropriate state to trigger on the types of events desired. There are four status levels defined for each subdetector: 0 indicates that the status of the subdetector is unknown, 1 indicates that it is off, 2 means that the detector is partially on (in case of a hardware problem or low voltage, for example), and 3 means that the detector is fully on. Table 4.1 shows the levels required for each detector used in the analysis.

### 4.1.2 Monte Carlo Event Samples

Four sets of simulated (Monte Carlo) data were used to estimate efficiencies and backgrounds for the analysis. Table 4.2 lists the generator used and number of events generated for each event type. For each event type, a set of four-vector quantities was generated to describe the  $e^+e^- \rightarrow f\bar{f}$  reaction, including the primary decays, initial and final state radiation, and decay radiation. The four-vectors were processed by the OPAL detector simulation program, GOPAL [43], which uses GEANT [44] to track the particles through the volume of the OPAL detector. GOPAL produces output in an identical format (with the addition of the initial four-vector information) to the data that is extracted from the OPAL detector. Each of the Monte Carlo samples is then passed through the same selection

procedure (described in the next section) as the real data.

The primary Monte Carlo event sample consisted of 293000 tau pair events used for estimating the  $\rho^-$  selection efficiency and the non- $\rho^-$  background in the final sample. These events were generated using KORALZ3.8 [39], which is designed to simulate tau pair decays at the  $Z^0$  centre-of-mass energy, taking into account effects from

1. multiple QED hard bremsstrahlung from the initial state  $e^\pm$  and single-photon bremsstrahlung from the final state fermion;
2.  $\mathcal{O}(\alpha)$  radiative corrections from the standard electroweak model;
3. spin polarization effects in  $\tau$  decay process (except for the multi-pion decays);
4. single bremsstrahlung in the most important  $\tau$  decay modes:  $\bar{\nu}\nu e^\pm$ ,  $\bar{\nu}\nu\mu^\pm$ ,  $\nu\pi^\pm$ ,  $\nu\rho^\pm$ ,  $\nu K^\pm$ ,  $\nu K^{*\pm}$  (in the leading logarithmic approximation).

The program can also be used to simulate other fermion-antifermion final states including  $\mu^+\mu^-$ . The decays of the taus produced by KORALZ3.8 are simulated using the TAUOLA1.5 [45] program. Other subprograms used in KORALZ3.8 are YFS [46] for initial and final state radiation, PHOTOS [47] for tau decay radiative corrections, and DIZET [48] for electroweak corrections.

The input branching ratios ( $\text{BR}_{\text{MC}}$ ) for the simulated tau pair events are given in Table 4.3 along with the world average branching ratios ( $\text{BR}_{\text{WA}}$ ). In the text and in this table,  $h^-$  represents either a  $\pi^-$  or  $K^-$ . The  $\text{BR}_{\text{MC}}$  set were the best estimate of the branching ratios at the time the Monte Carlo was produced. However, many new measurements with better precision have been made and we use these branching ratios in the analysis. For the  $\tau^- \rightarrow h^- \geq 2\pi^0\nu_\tau$  decays, the branching ratios are taken from recent results from CLEO [49] and the  $\tau^- \rightarrow \rho^-\nu_\tau$  branching ratio is determined in this analysis (see Appendix A). The remaining branching ratios are taken from the 1992 Review of Particle Properties [50]. They were adjusted to sum to exactly 100% and then used to define weight factors for each Monte Carlo decay type. The weights factors are defined as the ratio of the world average branching ratios to the Monte Carlo input branching ratios and are used to correct the estimated background ratios in the data.

Decay mode	BR <sub>MC</sub>	BR <sub>WA</sub>
$\tau^- \rightarrow \rho^- \nu_\tau$	24.7	$26.0 \pm 0.6$
$\tau^- \rightarrow e^- \bar{\nu}_e \nu_\tau$	18.3	$17.93 \pm 0.26$
$\tau^- \rightarrow \mu^- \bar{\nu}_\mu \nu_\tau$	17.8	$17.58 \pm 0.27$
$\tau^- \rightarrow h^+ h^- h^- \geq 0\pi^0 \nu_\tau$	14.4	$14.06 \pm 0.25$
$\tau^- \rightarrow h^- \nu_\tau$	12.6	$12.7 \pm 0.4$
$\tau^- \rightarrow h^- 2\pi^0 \nu_\tau$	9.6	$8.42 \pm 0.47$
$\tau^- \rightarrow h^- \geq 3\pi^0 \nu_\tau$	1.2	$1.00 \pm 0.14$
$\tau^- \rightarrow K^{*-} \nu_\tau$	1.8	$1.42 \pm 0.18$
$\tau^- \rightarrow 2h^+ 2h^- h^- \geq 0\pi^0 \nu_\tau$	0.2	$0.111 \pm 0.024$
Total	100.0	99.221

Table 4.3: This table shows the branching ratios that were used as input to the Monte Carlo tau pair simulation and the current world average branching ratios. The symbol  $h^-$  represents  $\pi^-$ 's and  $K^-$ 's.

## 4.2 Tau Selection Criteria

This section begins with a brief description of the topology we look for when selecting tau pair events. This is followed by an outline of the procedure used to reduce the full event sample to events containing tau pairs produced in  $Z^0$  decays. Complete details of the tau pair selection criteria can be found in refs. [52, 53].

The decay  $e^+e^- \rightarrow Z^0 \rightarrow \tau^+\tau^-$  is characterized by two nearly back-to-back ‘jets’ with one or more charged particles in each jet. Leptonic final states of the  $\tau^-$  have only one charged particle (either an electron or a muon) and two unobserved neutrinos. Hadronic final states have only a few (typically 1, 3 or 5) charged particles in the final state, possibly accompanied by neutral hadrons.

The decay of the  $Z^0$  into other final states, such as quark-antiquark ( $q\bar{q}$ ),  $e^+e^-$ , or  $\mu^+\mu^-$ , could also give signals similar to the one described above. Interactions not involving the production and decay of a  $Z^0$  can also give rise to signals of this kind.

When the  $Z^0$  decays into a quark-antiquark pair, free quarks are not observed. Instead, when the  $q\bar{q}$  pair separate, a collimated jet of hadrons is created through a process called fragmentation. Jets have, on average, twenty one light mesons (typically pions) [54]. We

expect far fewer charged particles than this in a lepton pair final state, so most of the decays of the  $Z^0$  to  $q\bar{q}$  pairs can be removed by limiting the numbers of charged tracks and electromagnetic clusters.

In OPAL, an acceptable track is defined by

$$\begin{aligned} N_{\text{hits}}(CJ) &\geq 20\text{hits} \\ p_T &\geq 0.1 \text{ GeV} \\ |d_0| &\leq 2 \text{ cm} \\ |z_0| &\leq 75 \text{ cm} \\ R_{\text{min}} &\leq 75 \text{ cm}, \end{aligned}$$

where  $N_{\text{hits}}(CJ)$  is the number of hits in the jet chamber,  $p_T$  is the momentum transverse to the beam direction,  $|d_0|$  is the point of closest approach of the track to the interaction point in the  $x$ - $y$  plane,  $|z_0|$  is the point of closest approach of the track to the interaction point in the  $z$  direction, and  $R_{\text{min}}$  is the radius of the first jet chamber hit.

An acceptable electromagnetic cluster in the barrel region ( $|\cos\theta| \leq 0.7$ ) is defined by

$$\begin{aligned} N_{\text{blk}} &\geq 1 \\ E_{\text{clst}} &\geq 0.1 \text{ GeV}, \end{aligned}$$

where  $N_{\text{blk}}$  is the number of calorimeter blocks in the cluster and  $E_{\text{clst}}$  is the total energy in the cluster. The  $q\bar{q}$  background is then reduced by requiring

$$\begin{aligned} 1 &\leq N_{\text{track}} \leq 6 \\ N_{\text{clst}} &\leq 10. \end{aligned}$$

The requirements on the track and cluster multiplicities are supplemented by requiring two well defined jets in the event. A jet is defined in terms of the tracks and clusters in the event [55]. The highest energy track defines the initial jet axis. The track with the next highest energy within a 35 degree half-angle cone about this axis is combined with the first track, with the vector sum of the momenta defining a new jet axis. This process

continues until all tracks and clusters within 35 degrees of the jet axis have been included. The process is repeated until all tracks in the event have been associated to a jet. An event is accepted if the event satisfies:

$$\begin{aligned} P_{\text{jet}} &\geq 0.01 E_{\text{beam}} \\ N_{\text{jet}} &= 2 \\ \langle |\cos \theta| \rangle &< 0.68, \end{aligned}$$

where  $P_{\text{jet}}$  is the total track and cluster energy in the jet,  $N_{\text{jet}}$  is the number of jets satisfying the  $P_{\text{jet}}$  requirement, and  $\langle |\cos \theta| \rangle$  is the average value of  $\cos \theta$  for the two jets. The fiducial requirement, necessary to avoid regions of non-uniform calorimeter response between the barrel and endcap detectors, reduces the detector acceptance to 59%.

Electron pair final states of the  $Z^0$  can be removed by requiring

$$\begin{aligned} \sum E_{\text{clst}} &\leq 0.8 E_{\text{CM}} \\ \text{or } \sum E_{\text{clst}} + 0.3 \sum E_{\text{trk}} &\leq E_{\text{CM}}. \end{aligned}$$

Muon pair final states of the  $Z^0$  can be removed by accepting only events for which both jets are identified as muons (described below) and requiring

$$\sum_{\text{jets}} E_{\text{clst}}^{\text{total}} + E_{\text{trk}}^{\text{total}} \leq 0.6 E_{\text{CM}}.$$

A jet is identified as a muon if at least one of the following three conditions is true:

(a)

$$N_{\text{layers}}^{\text{MUON}} \geq 2$$

where  $N_{\text{layers}}^{\text{MUON}}$  is the total number of layers in the barrel or endcap muon detector with signals associated to the track;

(b)

$$\begin{aligned} N_{\text{layers}}^{\text{HCAL}} &\geq 4, \\ N_{\text{outer 3 layers}}^{\text{HCAL}} &\geq 1, \\ \text{and } N_{\text{hits/layer}}^{\text{HCAL}} &< 2; \end{aligned}$$

where  $N_{\text{layers}}^{\text{HCAL}}$  is the number of hadron calorimeter layers with signals associated to the track,  $N_{\text{outer 3 layers}}^{\text{HCAL}}$  is the number of signals in the outer three layers, and  $N_{\text{hits/layer}}^{\text{HCAL}}$  is the total number of calorimeter signals assigned to the jet divided by  $N_{\text{layers}}^{\text{HCAL}}$ ,

(c) or

$$E_{\text{clst}} < 2\text{GeV}$$

where  $E_{\text{clst}}$  is the energy of the electromagnetic cluster associated to the track.

Cosmic rays are rejected by requirements on the tracks and the time-of-flight signals. Tracks must satisfy

$$\begin{aligned} |d_0|_{\text{min}} &\leq 0.5 \text{ cm} \\ |z_0|_{\text{min}} &\leq 20 \text{ cm} \\ |z_{0\text{ave}}| &\leq 20 \text{ cm}, \end{aligned}$$

where  $|d_0|_{\text{min}}$  is the minimum  $d_0$  for all tracks in the event,  $|z_0|_{\text{min}}$  is the minimum  $|z_0|$  for all tracks in the event, and  $|z_{0\text{ave}}|$  is the absolute value of the average  $z_0$  for all tracks in the event. At least one time-of-flight counter must satisfy

$$|t_{\text{meas}} - t_{\text{exp}}| \leq 10 \text{ ns},$$

where  $t_{\text{meas}}$  and  $t_{\text{exp}}$  are the measured and expected times of flight assuming the event is created at the origin. An event is rejected if all time-of-flight counter pairs  $i$  and  $j$  with  $|\phi_i - \phi_j| \geq 165^\circ$  have

$$|t_i - t_j| \geq 10 \text{ ns}.$$

Two-photon events,  $e^+e^- \rightarrow e^+e^-X$ , can be removed by requiring

$$\begin{aligned} \theta_{\text{acol}} &\leq 15^\circ \\ E_{\text{vis}} &\equiv \sum_{\text{jets}} \text{Max}(\sum E_{\text{clst}}, \sum E_{\text{trk}}) \geq 0.03 E_{\text{CM}}, \end{aligned}$$

Background	Contamination (%)
$e^+e^- \rightarrow q\bar{q}$	$0.42 \pm 0.18$
$e^+e^- \rightarrow e^+e^-$	$0.22 \pm 0.08$
$e^+e^- \rightarrow \mu^+\mu^-$	$0.91 \pm 0.46$
$e^+e^- \rightarrow e^+e^-e^+e^-$	$0.09 \pm 0.02$
$e^+e^- \rightarrow e^+e^-\mu^+\mu^-$	$0.07 \pm 0.02$
Total	$1.71 \pm 0.50$

Table 4.4: This table shows the non-tau background contributions after the tau pair selection requirements are applied.

where  $\theta_{\text{acol}}$  is the acollinearity in the transverse plane between the two jets. If  $E_{\text{vis}} \leq 0.20E_{\text{CM}}$ , the transverse component of the vector sum of the track momenta or cluster energies must satisfy at least one of

$$P_T(\text{clst}) > 2.0 \text{ GeV}$$

$$P_T(\text{trk}) > 2.0 \text{ GeV}$$

in order to keep the event.

### 4.2.1 Final Tau Pair Sample

A total of 27353 tau pairs were selected from the 1991 and 1992 data. The efficiency of this selection is estimated from the tau pair Monte Carlo sample to be 92.7% within the fiducial acceptance defined for the jets, for an overall tau pair selection efficiency of  $54.7 \pm 0.7\%$ . The background contamination is estimated [51] from the Monte Carlo event samples to be  $1.71 \pm 0.50\%$ , with the individual contributions detailed in Table 4.4.

## 4.3 $\tau^- \rightarrow \rho^- \nu_\tau$ Selection

This section presents the criteria used to select  $\tau^- \rightarrow \rho^- \nu_\tau$  jets. We begin with a brief description of a refined algorithm [51] which is used to define the electromagnetic clusters. The details of the  $\tau^- \rightarrow \rho^- \nu_\tau$  selection procedure are then presented.

### 4.3.1 Cluster definition

The algorithm used to define the electromagnetic clusters for this analysis [51] attempts to maximize the efficiency for resolving both photons produced from the decay of a high energy  $\pi^0$ . It was developed specifically for analyzing tau pair final states. In the low multiplicity environment of a tau decay, it is possible to accurately measure the positions of showers in the electromagnetic calorimeter that are separated by angles as small as  $\approx 20$  mrad. The clustering algorithm uses the observation that on average 99% of the energy deposited by an electron (and 95% of the energy deposited by a charged pion) is contained within a  $2 \times 2$  array of blocks in the electromagnetic calorimeter. An enhancement of at least 30% in the identified  $\pi^0$  signal over the standard OPAL clusters is observed, due primarily to the increase in efficiency for separating the two photons produced in a high energy  $\pi^0$  decay.

### 4.3.2 $\tau^- \rightarrow \rho^- \nu_\tau$ Selection Criteria

The  $\rho^-$  decays into  $\pi^- \pi^0$  and subsequently the  $\pi^0$  decays into two photons before reaching the detector. Thus, the events to be analyzed are characterized by a single charged track ( $\pi^-$ ) and energy clusters in the electromagnetic calorimeter ( $\gamma\gamma$ ) that are not associated to the track. This analysis only considers the case where the  $\pi^0$  decay photons enter the electromagnetic calorimeter sufficiently separated from the extrapolated track position to form distinct clusters of energy. The case where the two photons from the  $\pi^0$  decay *overlap* each other is accepted, however, implying that there will be either one or two clusters of energy not associated to the charged track. The major sources of background come from  $\tau^- \rightarrow h^- 2\pi^0 \nu_\tau$ , where one of the  $\pi^0$ 's is not seen, and from  $\tau^- \rightarrow K^{*-} \nu_\tau$ , where  $K^{*-} \rightarrow K^- \pi^0$ . Other tau decays, such as  $\tau^- \rightarrow \pi^- \nu_\tau$ , can contribute to the background when radiative photons are emitted from the decay product or when a hadron deposits energy over a large area forming *fake* clusters.

The two jets in the tau pair event are identified separately. The  $\tau$ 's from  $Z^0 \rightarrow \tau^+ \tau^-$  are very energetic ( $\gamma \approx 25$ ). Consequently, the  $\tau^- \rightarrow \rho^- \nu_\tau$  decay is highly collimated and tracks and clusters are accepted only if they fall within a 0.3 radian half-angle cone

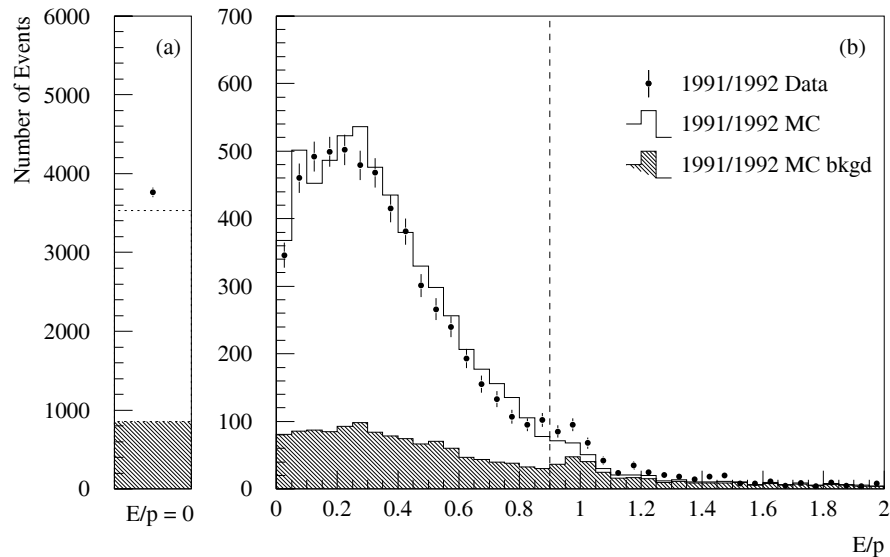


Figure 4.1: This figure shows the distribution of events in  $E/p$  after all other selection requirements are applied. The  $E/p = 0$  bin has been plotted separately with a different scale.

defined around the jet axis. Tracks or clusters outside this cone are ignored.

Only one good track is allowed within this cone. If there is an electromagnetic calorimeter cluster associated to the track, we require

$$E/p < 0.9,$$

where  $E$  is the energy of the cluster and  $p$  is the track momentum, to reduce backgrounds from  $\tau^- \rightarrow e^- \bar{\nu}_e \nu_\tau$  and  $\tau^- \rightarrow h^- \geq 2\pi^0 \nu_\tau$ . Figure 4.1 shows the distribution of events in  $E/p$  after all other selection requirements are applied, with the rejected events to the right of the dashed line. The  $\tau^- \rightarrow e^- \bar{\nu}_e \nu_\tau$  decays have  $E/p \approx 1$ , since all of the energy is absorbed in the calorimeter, and the  $\tau^- \rightarrow h^- \geq 2\pi^0 \nu_\tau$  decays typically have  $E/p > 0.9$  because one or both of the  $\pi^0$ 's enters the calorimeter so close to the track that they cannot be distinguished from each other.

Low energy muons may range out and deposit all of their energy in the electromagnetic calorimeter. Additionally, hadronic showers from low energy pions can produce many

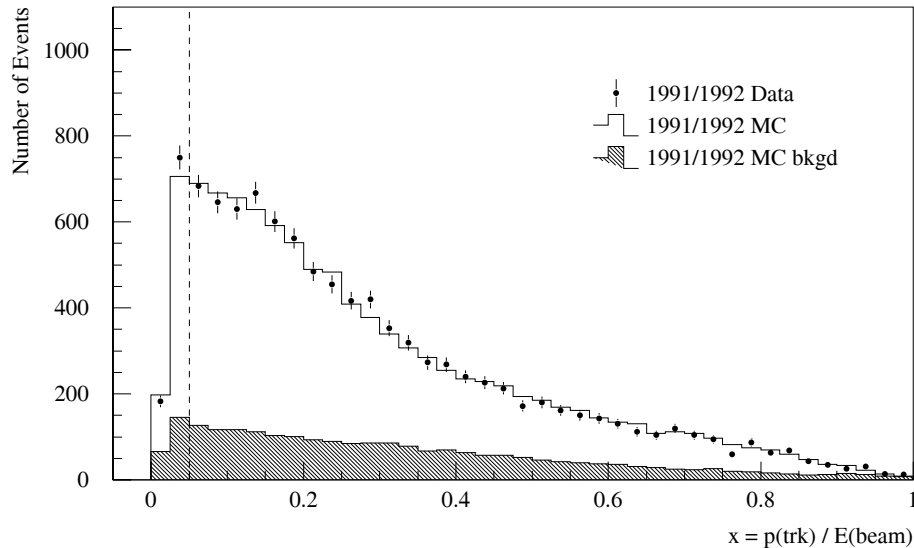


Figure 4.2: This figure shows  $x \equiv p_{\text{trk}}/E_{\text{beam}}$  after all other selection requirements are applied.

small clusters of energy in the ECAL. For these reasons, we require

$$x \equiv p_{\text{trk}}/E_{\text{beam}} > 0.05.$$

Figure 4.2 shows good agreement between data and Monte Carlo for the distribution of events in  $x$  after all other selection criteria are applied. Events to the left of the dashed line are rejected.

A threshold of 1.2 GeV is used for the electromagnetic clusters. This lets us accept lower energy  $\pi^0$ 's, which are more likely to decay into two well separated photons, while reducing the background from hadronic showers. When the two photons are well separated, the mass measurement, and hence the measurement of the polarization, is more accurate. Only events with either one or two clusters which are not associated to the track and which pass the energy threshold and cone restrictions are accepted.

When an event has two neutral clusters, the invariant mass of these clusters,  $m_{\gamma\gamma}$ , is compared with the  $\pi^0$  mass. The event is accepted if

$$m_{\gamma\gamma} < 280 \text{ MeV}.$$

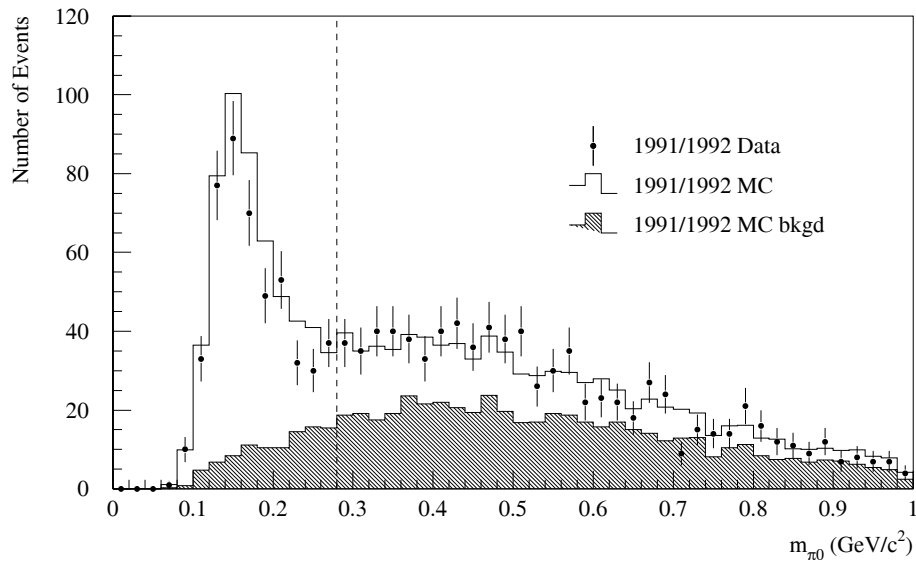


Figure 4.3: This figure shows the reconstructed mass of the neutral clusters in events which contain two neutral clusters, after applying all selection requirements other than the two cluster mass requirement.

The energies of the two clusters are summed and the  $\pi^0$  momentum calculated assuming the invariant mass is exactly the mass of the  $\pi^0$ . Figure 4.3 shows the distribution of the reconstructed mass of the neutral clusters in events which have two neutral clusters.

Finally, the invariant mass of the jet,  $m_{\text{jet}}$ , is determined from the momentum of the charged track and the energy and momentum of the neutral cluster(s). The event is accepted if

$$0.5 < m_{\text{jet}} < 2.0 \text{ GeV}/c^2,$$

as shown in figure 4.4. The lower limit reduces background from from the decay  $\tau^- \rightarrow h^- \nu_\tau$  where the ‘neutral energy’ comes from fake clusters as described earlier. The upper limit reflects the physical upper limit set by the mass of the tau lepton. The  $\rho^-$  and  $K^{*-}$  decay channels are both included within the selection window.

This selection criteria is also used to calculate the  $\tau^- \rightarrow \rho^- \nu_\tau$  branching ratio. This work is reported in Appendix A. The agreement between the branching ratio measured here and other recently measured branching ratios makes us confident that the selection

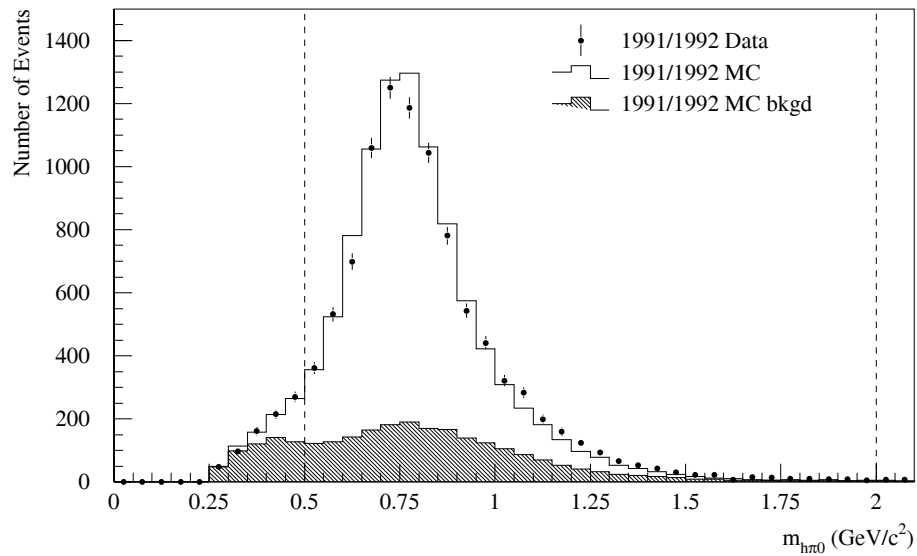


Figure 4.4: This figure shows the distribution of the reconstructed mass of the events after all other selection criteria are applied. The data and the Monte Carlo are in good agreement.

is well understood. The branching ratio calculation includes the contribution from  $K^{*-}$ , and is therefore more correctly reported as the  $\tau^- \rightarrow h^- \pi^0 \nu_\tau$  channel.

# Chapter 5

## Polarization Analysis

This chapter describes the measurement of the average tau polarization asymmetry and the forward-backward tau polarization asymmetry. The first section outlines the method used to extract the polarization information and the second section presents the results.

### 5.1 Polarization as a Function of $\cos \theta$

This section describes the measurement of  $P_\tau$  as a function of  $\cos \theta$ . The first three subsections detail the procedure for determining the polarization at the centre of each of the  $\cos \theta$  bins, and the final subsection presents the values.

The data are divided into five equal bins between  $\cos \theta = -0.68$  and  $\cos \theta = +0.68$ , where  $\theta$  is the angle between the  $e^-$  direction and the  $\tau^-$  direction. In each  $\cos \theta$  bin, the data and theoretical distributions are projected into two-dimensional histograms in  $\cos \theta^*$ - $\cos \psi$ . The theoretical distribution is modified to include detector resolution effects, non- $\rho^-$  backgrounds, and selection efficiencies. Fitting the data with the corrected distribution gives the polarization,  $P_\tau$ , in each  $\cos \theta$  bin. The average tau polarization,  $\langle P_\tau \rangle$ , and the forward-backward tau polarization asymmetry,  $A_{\text{FB}}^{\text{Pol}}$ , are then determined by fitting the angular variation in the tau polarization over the five  $\cos \theta$  bins.

#### 5.1.1 Data and Theoretical Distributions

The  $\cos \theta^*$ - $\cos \psi$  distribution is approximated by a two-dimensional histogram of  $5 \times 5$  equally spaced bins over  $-1 \leq \cos \theta^* \leq 1$  and  $-1 \leq \cos \psi \leq 1$ . The values of  $\cos \theta^*$  and

$\cos \psi$  are calculated using equations 2.40 and 2.41 for each event in the selected sample and an entry is made into the corresponding histogram bin. The number of events in bin  $ij$  of the two-dimensional histogram<sup>1</sup> is given by  $N_{ij}^{\text{data}}$ , and the fraction of events in bin  $ij$  is given by

$$f_{ij}^{\text{data}} = \frac{N_{ij}^{\text{data}}}{N_{\text{tot}}^{\text{data}}}, \quad (5.1)$$

where  $N_{\text{tot}}^{\text{data}} = \sum_{ij} N_{ij}^{\text{data}}$ . Due to the finite resolution of the measured energies and momenta, some of the reconstructed values of  $\cos \theta^*$  will be outside of the physical region,  $|\cos \theta^*| < 1$ . No events will have  $|\cos \psi| > 1$ , due to the form of the function used to define this quantity (see equation 2.41). These events are entered into the nearest  $\cos \theta^*$  bin of the distribution, and the effect will be corrected later with the Monte Carlo. The polarization,  $P_\tau(\cos \theta)$ , is determined by comparing the  $f_{ij}^{\text{data}}$  with a theoretical distribution.

The theoretical distribution given in equation 2.43 is a tree level approximation and does not include radiative corrections that are required to describe the data. The radiatively corrected theoretical distribution is thus determined from a Monte Carlo simulation. A large sample (1000000  $\tau^+\tau^-$  events) of four-vector Monte Carlo  $\tau^- \rightarrow \rho^- \nu_\tau$  decays (ie. without the full detector reconstruction) was generated using KORALZ4.0 [56] to provide the parent theoretical distribution. This sample was divided into two sets of events:  $T^+$ , with positive helicity state events ( $-qh > 0$ , where  $q$  is the charge of the  $\tau$  lepton, and  $h$  is the helicity), and  $T^-$ , with negative helicity state events ( $-qh < 0$ ). These two sets were entered into the histograms,  $T_{ij}^\pm$ , with identical  $\cos \theta^*$ - $\cos \psi$  bin definitions as the data. Using these two sets, any average polarization can be constructed by the linear combination,

$$f_{ij}^{\text{model}} = \frac{1}{2} \left[ (1 + P_\tau) I_{ij}^+ + (1 - P_\tau) I_{ij}^- \right], \quad (5.2)$$

where

$$I_{ij}^\pm = \frac{T_{ij}^\pm}{T^\pm} \quad (5.3)$$

and  $T^\pm = \sum_{ij} T_{ij}^\pm$ . Note that  $\sum_{ij} I_{ij}^\pm = 1$ .

---

<sup>1</sup>Index  $i$  refers to bins in  $\cos \theta^*$  and index  $j$  refers to bins in  $\cos \psi$ .

### 5.1.2 Corrections to the Theoretical Distributions

The five  $\cos \theta^*$ - $\cos \psi$  distributions measured in the final data sample are not the same as the parent distributions of the underlying events because of detector resolution, non- $\rho^-$  background contamination, and selection efficiencies. This section will describe how the size of these effects on the data can be estimated from the sample of 293000 fully reconstructed Monte Carlo events (see Chapter 4).

The resolution  $R_{ij}$ , the selection efficiency  $\epsilon_{ij}$ , and the fraction of background events  $f_{(\text{bg}) ij}$  can be estimated for each  $\cos \theta^*$ - $\cos \psi$  bin by examining the parent four-vector quantities and the final reconstructed quantities. The expected number of  $\tau^- \rightarrow \rho^- \nu_\tau$  decays in each bin is determined by subtracting the background, dividing by the efficiency, and correcting for the resolution,

$$N_{(\text{parent}) ij} = \frac{(1 - f_{(\text{bg}) ij})}{\epsilon_{ij} R_{ij}} N_{(\text{sel}) ij}, \quad (5.4)$$

where

$$f_{(\text{bg}) ij} = \frac{N_{(\text{bg}) ij}}{N_{(\text{sel}) ij}}, \quad (5.5)$$

$N_{(\text{bg}) ij}$  is the number of background events and  $N_{(\text{sel}) ij}$  is the total number of selected events in each bin. We do not correct the measured histogram contents, but instead modify the parent distribution to yield the expected number of measured events. The equation is then written

$$N_{(\text{sel}) ij} = \frac{\epsilon_{ij} R_{ij}}{(1 - f_{(\text{bg}) ij})} N_{(\text{parent}) ij} \equiv C_{ij} N_{(\text{parent}) ij}. \quad (5.6)$$

The fully reconstructed Monte Carlo sample is divided into positive and negative helicity state events which are entered into separate  $\cos \theta^*$ - $\cos \psi$  histograms. Two sets of histograms are made: in the first set, the values of  $\cos \theta^*$  and  $\cos \psi$  are determined from the reconstructed quantities, and in the second set, the four-vector quantities are used. Separate positive and negative helicity state correction factors  $R_{ij}^\pm$ ,  $f_{(\text{bg}) ij}^\pm$ , and  $\epsilon_{ij}^\pm$  are then calculated from the two sets of histograms as described below.

The detector resolution modifies the measured  $\cos \theta^*$  and  $\cos \psi$  values for each event

from the parent values. The resolution factors are approximated by the ratio

$$R_{ij}^{\pm} = \frac{N_{(\rho)ij}^{\pm}}{\mathcal{N}_{(\rho)ij}^{\pm}}, \quad (5.7)$$

where  $\mathcal{N}_{(\rho)ij}^{\pm}$  is the number of true  $\tau^{-} \rightarrow \rho^{-} \nu_{\tau}$  events in bin  $ij$  after the  $\rho^{-}$  selection, with  $\cos \theta^{*} - \cos \psi$  for each event determined from four-vector quantities, and  $N_{(\rho)ij}^{\pm}$  is the number of true  $\tau^{-} \rightarrow \rho^{-} \nu_{\tau}$  events in bin  $ij$  after the  $\rho^{-}$  selection, with  $\cos \theta^{*} - \cos \psi$  for each event determined from reconstructed quantities<sup>2</sup>. The detector resolution correction factors are shown graphically in figure 5.1.

The fraction of background events in the final sample is given by

$$f_{(\text{bg})ij}^{\pm} = \frac{N_{(\text{bg})ij}^{\pm}}{N_{(\text{sel})ij}^{\pm}}, \quad (5.8)$$

where  $N_{(\text{bg})ij}^{\pm}$  is the number of non- $\rho$  events in the  $\rho^{-}$  selected sample, and  $N_{(\text{sel})ij}^{\pm}$  is the number of selected events in the  $\rho^{-}$  selected sample, satisfying

$$N_{(\text{sel})ij}^{\pm} = N_{(\rho)ij}^{\pm} + N_{(\text{bg})ij}^{\pm}. \quad (5.9)$$

Note that both the numerator and the denominator of  $f_{(\text{bg})ij}^{\pm}$  are determined using reconstructed values of  $\cos \theta^{*}$  and  $\cos \psi$ . The background contamination correction factors are shown graphically in figure 5.2. As discussed in Chapter 4, the fully reconstructed Monte Carlo was generated using the best estimates of the  $\tau^{-}$  branching ratios that were available at the time. In this analysis we used more recent measurements, and adjusted the event counts in the Monte Carlo accordingly. Therefore, each Monte Carlo event was entered into the  $\cos \theta^{*} - \cos \psi$  histogram with a weight different from unity. The weight for each event was determined by first adjusting the world average branching ratios to sum to one, and then taking the ratio of the adjusted  $\text{BR}_{\text{WA}}$  to the Monte Carlo input  $\text{BR}_{\text{MC}}$  (see Table 4.3). This ratio was used as the weight for each decay channel.

The selection efficiencies can be conceptually divided into two sets:  $\tau$  pair selection efficiencies and  $\rho^{-}$  selection efficiencies. The  $\tau$  pair selection efficiency is defined as the ratio of the remaining number of true  $\tau^{-} \rightarrow \rho^{-} \nu_{\tau}$  events after the  $\tau$  pair selection ( $\mathcal{N}_{(\rho)ij}^{(\tau)\pm}$ )

---

<sup>2</sup>Script letters refer to four-vector quantities and Roman letters refer to reconstructed quantities.

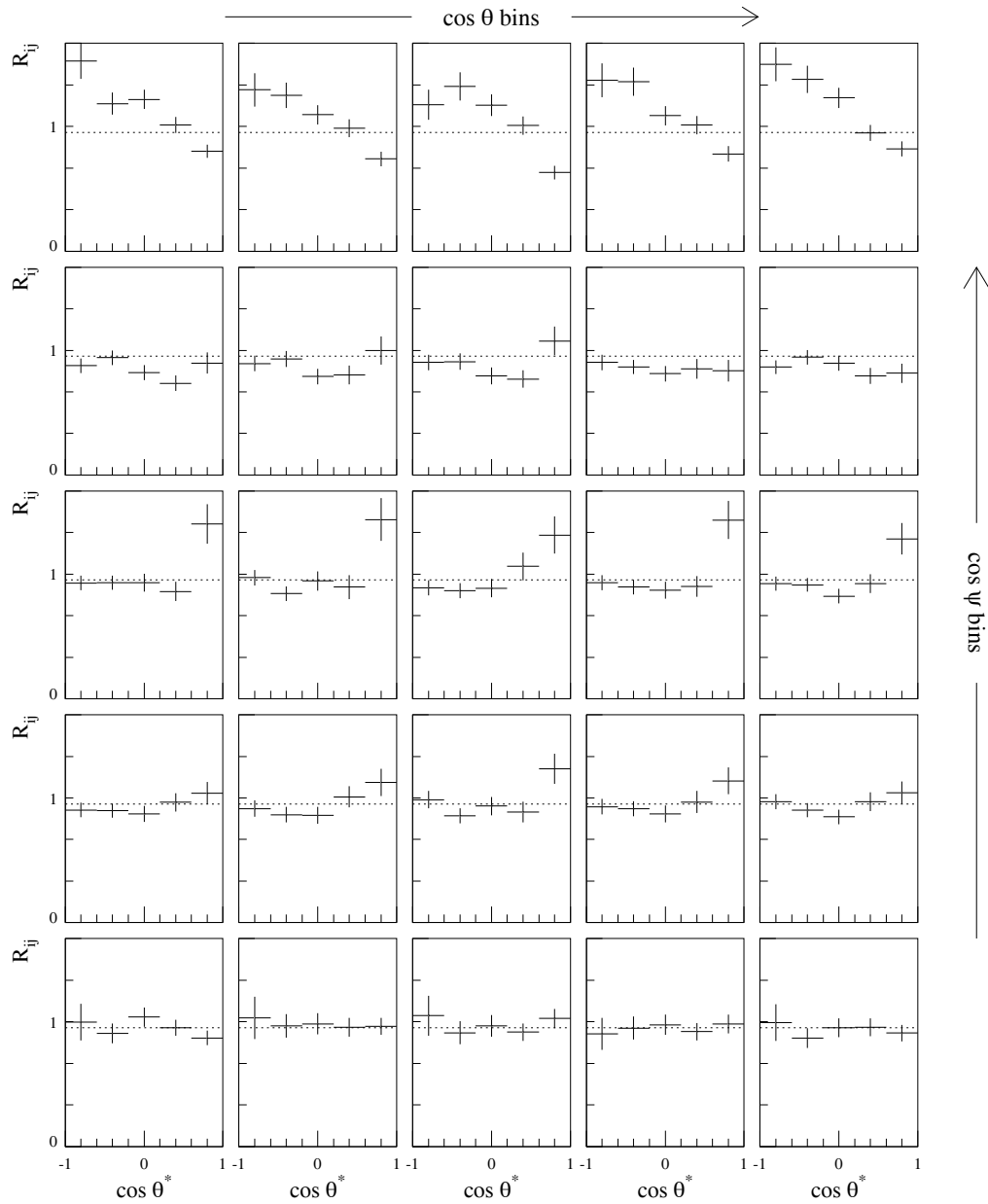


Figure 5.1: This figure shows the detector resolution correction factors, where the positive and negative helicity states have been averaged together. Each plot shows the variation of  $R_{ij}$  with  $\cos \theta^*$ . The plots are arranged in increasing  $\cos \theta$  (from  $-0.68$  to  $+0.68$ ) across the page, and increasing  $\cos \psi$  (from  $-1$  to  $+1$ ) up the page. The dotted line in each plot shows the value 1, for which the reconstructed  $\cos \theta^*$ - $\cos \psi$  bin contents would equal the four-vector bin contents.

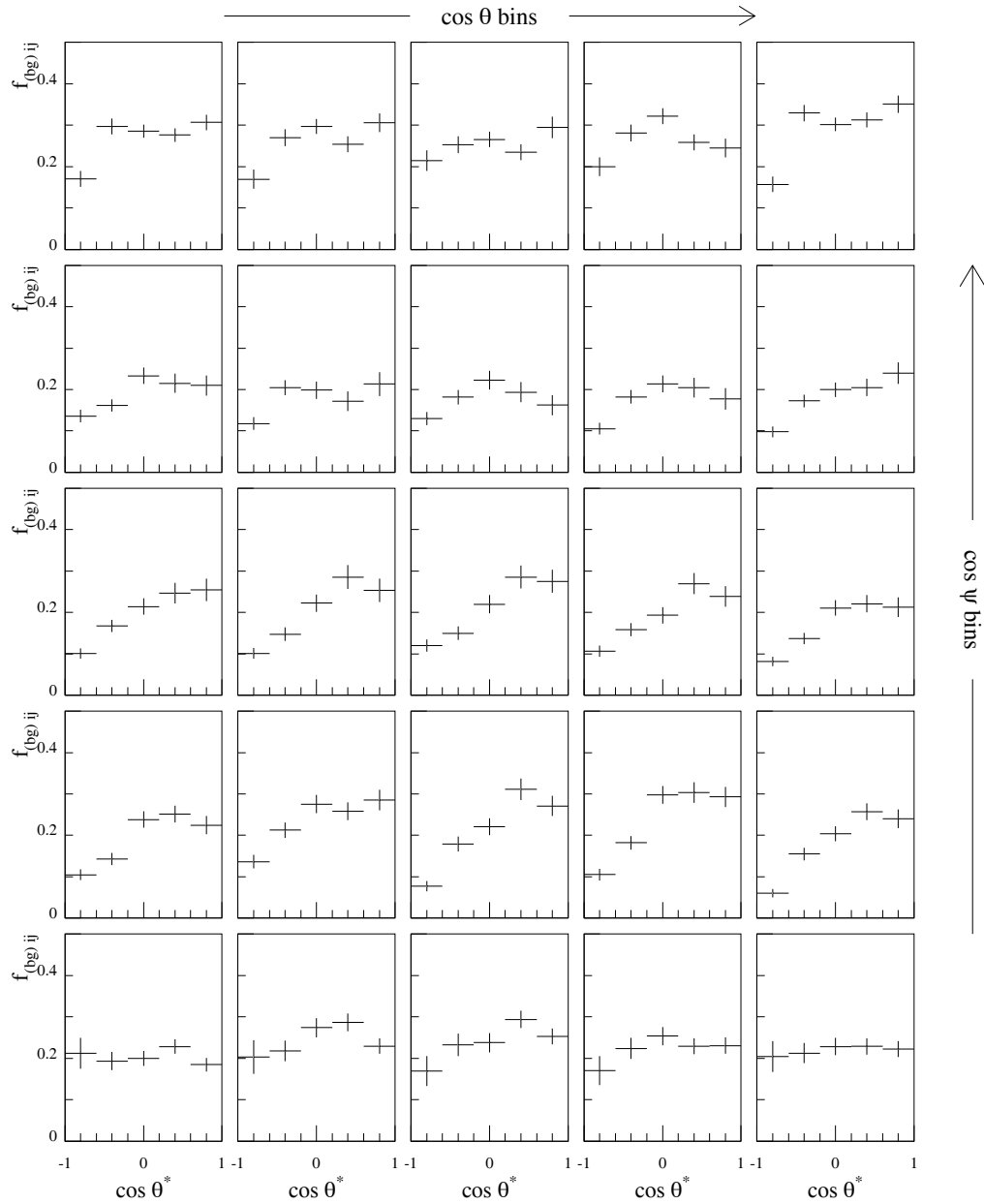


Figure 5.2: This figure shows the correction factors for the backgrounds, where the positive and negative helicity states have been averaged together. Each plot shows the variation of  $f_{(bg)ij}$  with  $\cos \theta^*$ . The plots are arranged in increasing  $\cos \theta$  (from  $-0.68$  to  $+0.68$ ) across the page, and increasing  $\cos \psi$  (from  $-1$  to  $+1$ ) up the page.

over the original number of true  $\tau^- \rightarrow \rho^- \nu_\tau$  events before any selection is applied to the Monte Carlo ( $\mathcal{N}_{(\rho) ij}^{(\text{all}) \pm}$ ), where four-vector values for  $\cos \theta^*$  and  $\cos \psi$  have been used for each event. The efficiency factor can be written as

$$\epsilon_{ij}^{(\tau) \pm} = \frac{\mathcal{N}_{(\rho) ij}^{(\tau) \pm}}{\mathcal{N}_{(\rho) ij}^{(\text{all}) \pm}}. \quad (5.10)$$

Note that the efficiency in each bin is approximately equal to 1. The larger efficiency correction arises from the  $\rho^-$  selection which is the focus of this thesis. The  $\rho^-$  selection efficiency is defined as the ratio of the number of true  $\tau^- \rightarrow \rho^- \nu_\tau$  events after the  $\rho^-$  selection ( $\mathcal{N}_{(\rho) ij}^{\pm}$ ) over the number of true  $\tau^- \rightarrow \rho^- \nu_\tau$  events after the  $\tau$  pair selection ( $\mathcal{N}_{(\rho) ij}^{(\tau) \pm}$ ). This can be written as

$$\epsilon_{ij}^{(\rho) \pm} = \frac{\mathcal{N}_{(\rho) ij}^{\pm}}{\mathcal{N}_{(\rho) ij}^{(\tau) \pm}}. \quad (5.11)$$

The overall efficiency for events passing the  $\tau^- \rightarrow \rho^- \nu_\tau$  selection is the product of these two quantities, and is given by

$$\epsilon_{ij}^{\pm} = \frac{\mathcal{N}_{(\rho) ij}^{\pm}}{\mathcal{N}_{(\rho) ij}^{(\text{all}) \pm}}. \quad (5.12)$$

The selection efficiency correction factors are shown graphically in figure 5.3.

The three correction factors (5.7, 5.8, and 5.10) can be substituted into equation 5.6 to give an overall bin-by-bin correction factor for each helicity state which can be written as

$$C_{ij}^{\pm} = \frac{N_{(\text{sel}) ij}^{\pm}}{\mathcal{N}_{(\rho) ij}^{(\text{all}) \pm}}. \quad (5.13)$$

The model to be compared with the final data sample is given by (See Appendix B for a full derivation of this equation)

$$f_{ij}^{\text{fit}} = \frac{(1 + P_\tau) C_{ij}^+ I_{ij}^+ + (1 - P_\tau) C_{ij}^- I_{ij}^-}{(1 + P_\tau) \sum_{lm} C_{lm}^+ I_{lm}^+ + (1 - P_\tau) \sum_{lm} C_{lm}^- I_{lm}^-}, \quad (5.14)$$

Note that if  $C_{ij}^{\pm} = 1$ , this reduces to equation 5.2.

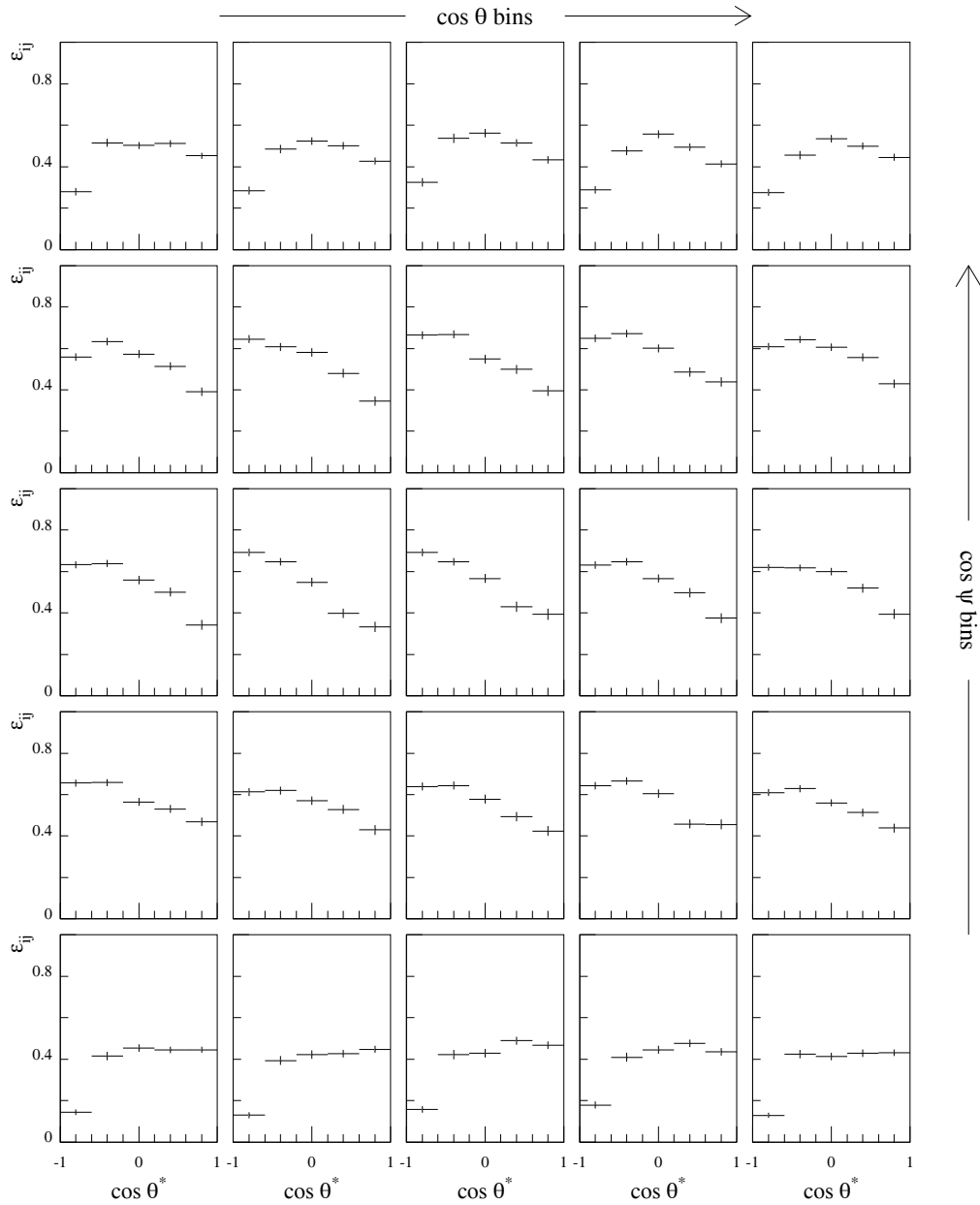


Figure 5.3: This figure shows the selection efficiency correction factors, where the positive and negative helicity states have been averaged together. Each plot shows the variation of  $\epsilon_{ij}$  with  $\cos \theta^*$ , and the plots are arranged in increasing  $\cos \theta$  (from  $-0.68$  to  $+0.68$ ) across the page, and increasing  $\cos \psi$  (from  $-1$  to  $+1$ ) up the page.

### 5.1.3 Fit for Polarization in each $\cos \theta$ Bin

The polarization,  $P_\tau$ , is determined at the centre of each  $\cos \theta$  bin by minimizing the modified  $\chi^2$  statistic given by

$$\chi_{\cos \theta}^2(P_\tau) = \sum_{i=1, j=1}^{5,5} \frac{(f_{ij}^{\text{data}} - f_{ij}^{\text{fit}})^2}{(\sigma_{ij}^{\text{data}})^2 + (\sigma_{ij}^{\text{fit}})^2} \quad (5.15)$$

where  $\sigma_{ij}^{\text{data}}$  is the binomial error from the data,

$$(\sigma_{ij}^{\text{data}})^2 = \frac{f_{ij}^{\text{data}}(1 - f_{ij}^{\text{data}})}{N_{\text{tot}}^{\text{data}}}, \quad (5.16)$$

and  $\sigma_{ij}^{\text{fit}}$  is the Monte Carlo statistical error given by (see Appendix B for a full derivation of this equation)

$$\begin{aligned} (\sigma_{ij}^{\text{fit}})^2 &= \left( \frac{1 - f_{ij}^{\text{fit}}}{(1 + P_\tau) \sum_{lm} C_{lm}^+ I_{lm}^+ + (1 - P_\tau) \sum_{lm} C_{lm}^- I_{lm}^-} \right)^2 \\ &\times \sum_{+,-} (1 \pm P_\tau)^2 \left[ \sigma_{C_{ij}^\pm}^2 (I_{ij}^\pm)^2 + (C_{ij}^\pm)^2 \sigma_{I_{ij}^\pm}^2 \right] \end{aligned} \quad (5.17)$$

where the summation,  $\sum_{+,-}$ , is over the positive and negative helicity terms. The minimization procedure, performed using MINUIT [57], returns the central value of  $P_\tau$  as well as positive and negative errors which are defined by the amount of change in  $P_\tau$  which causes  $\chi_{\cos \theta}^2$  to increase by 1.

Equation 5.15 is not a true  $\chi^2$  statistic, since it includes the additional term,  $\sigma_{ij}^{\text{fit}}$ , in the denominator. This equation does, however, give the best estimate of the value of  $P_\tau$ , since the  $f_{ij}^{\text{fit}}$  are determined using Monte Carlo event counts which have statistical fluctuations. The uncertainty in  $P_\tau$  due only to the data statistics can be evaluated by removing  $\sigma_{ij}^{\text{fit}}$  from the denominator of  $\chi_{\cos \theta}^2$  and performing the minimization again. Table 5.1 lists, for each  $\cos \theta$  bin, the values of  $P_\tau$ , the uncertainties, and  $\chi_{\cos \theta}^2$ , for these two separate fitting procedures. The effect of including or excluding  $\sigma_{ij}^{\text{fit}}$  from the definition of  $\chi_{\cos \theta}^2$  will be discussed as a systematic error on the measured asymmetries.

$\cos \theta$	$N_{\text{events}}$	$P_\tau$ (incl. $\sigma_{ij}^{\text{fit}}$ )	$\chi^2$ (24 DOF)	$P_\tau$ (excl. $\sigma_{ij}^{\text{fit}}$ )	$\chi^2$ (24 DOF)
-0.544	1979	$-0.096 \pm 0.066$	26.4	$-0.095 \pm 0.060$	30.5
-0.272	1648	$-0.049 \pm 0.071$	17.5	$-0.050 \pm 0.065$	20.2
0.000	1488	$-0.173 \pm 0.078$	24.0	$-0.177 \pm 0.073$	27.8
0.272	1713	$-0.254 \pm 0.072$	18.8	$-0.265 \pm 0.066$	22.1
0.544	2054	$-0.207 \pm 0.062$	23.8	$-0.208 \pm 0.057$	28.0

Table 5.1: This table shows the values of the tau polarization as a function of the central values of the  $\cos \theta$  bins. The third and fourth column present  $P_\tau$  and  $\chi^2_{\cos \theta}$  for the fits which include the Monte Carlo statistical uncertainty,  $\sigma_{ij}^{\text{fit}}$ , in the definition of  $\chi^2_{\cos \theta}$ . These  $P_\tau$  values will be used to determine the values of  $\langle P_\tau \rangle$  and  $A_{\text{FB}}^{\text{Pol}}$ . The last two columns list  $P_\tau$  and  $\chi^2_{\cos \theta}$  for the fits which do not include  $\sigma_{ij}^{\text{fit}}$ , and these values of  $P_\tau$  will be used to determine the statistical uncertainty on  $\langle P_\tau \rangle$  and  $A_{\text{FB}}^{\text{Pol}}$ .

## 5.2 Average Tau Polarization and Forward-Backward Tau Polarization Asymmetry

This section describes how the average tau polarization,  $\langle P_\tau \rangle$ , and the forward-backward tau polarization asymmetry,  $A_{\text{FB}}^{\text{Pol}}$ , are determined from the five measured values of  $P_\tau$ . The results are then presented and the systematic errors are described.

### 5.2.1 Fit to $P_\tau$ vs. $\cos \theta$

The five values of  $P_\tau$  can be fit with or without the assumption of lepton universality. When lepton universality is not assumed, we determine the average tau polarization and the forward-backward tau polarization asymmetry using the equation (see Section 2.2.1)

$$P_\tau(\cos \theta) = \frac{\langle P_\tau \rangle (1 + \cos^2 \theta) + \frac{8}{3} A_{\text{FB}}^{\text{Pol}} \cos \theta}{(1 + \cos^2 \theta) + \frac{8}{3} A_{\text{FB}} \cos \theta}. \quad (5.18)$$

to model the data in table 5.1. The central values of  $\langle P_\tau \rangle$  and  $A_{\text{FB}}^{\text{Pol}}$  are determined by fitting the quantities in the third row of this table, and the statistical errors on these two parameters determined by fitting the values in the fifth column. The value of  $A_{\text{FB}}$  has been previously determined from OPAL data [37] to be

$$A_{\text{FB}} = 0.0165 \pm 0.0082 \quad (5.19)$$

on the  $Z^0$  resonance. If we assume lepton universality,

$$\begin{aligned} A_{e\tau} &\equiv -\langle P_\tau \rangle = -\frac{4}{3}A_{\text{FB}}^{\text{Pol}} \\ A_{\text{FB}} &= \frac{3}{4}A_{e\tau}^2, \end{aligned} \quad (5.20)$$

where  $A_{e\tau}$  is the lepton asymmetry, equation 5.18 becomes

$$P_\tau(\cos\theta) = -\frac{A_{e\tau}(1 + \cos\theta)^2}{(1 + \cos^2\theta) + 2A_{e\tau}^2 \cos\theta}. \quad (5.21)$$

In the case of both fits, the  $\chi^2$  statistic between the data and the model is minimized, and the uncertainty in each of the variable parameters of the model ( $\langle P_\tau \rangle$ ,  $A_{\text{FB}}^{\text{Pol}}$ ,  $A_{e\tau}$ ) is defined by the amount of change in the parameter that causes the  $\chi^2$  to increase by 1.

## 5.2.2 Polarization and Asymmetry Results

The values in table 5.1 are shown graphically in figure 5.4 along with the results of least-squares fits to equations 5.18 (dotted line - no lepton universality) and 5.21 (solid line - assume lepton universality). If lepton-universality is not demanded, the average tau polarization is

$$\langle P_\tau \rangle = -0.155 \pm 0.028(\text{stat}) \pm 0.014(\text{syst}) \quad (5.22)$$

and the forward-backward tau polarization asymmetry is

$$A_{\text{FB}}^{\text{Pol}} = -0.076 \pm 0.033(\text{stat}) \pm 0.015(\text{syst}), \quad (5.23)$$

with  $\chi^2 = 1.5$  with 3 degrees of freedom. Under the assumption of lepton universality, we find

$$A_{e\tau} = 0.139 \pm 0.024(\text{stat}) \pm 0.012(\text{syst}) \quad (5.24)$$

with  $\chi^2 = 2.4$  with 4 degrees of freedom. As discussed in the previous section, the central values of  $\langle P_\tau \rangle$ ,  $A_{\text{FB}}^{\text{Pol}}$ , and  $A_{e\tau}$  are determined with the term  $\sigma_{ij}^{\text{fit}}$  in the denominator of the  $\chi_{\cos\theta}^2$  functions. The ‘(stat)’ errors on these quantities are from the data statistics only, and are the errors returned when the values in the fifth column of table 5.1 are fit to equations 5.18 and 5.21. The quoted systematic errors are determined from the quadratic sum of the individual contributions listed in table 5.2.

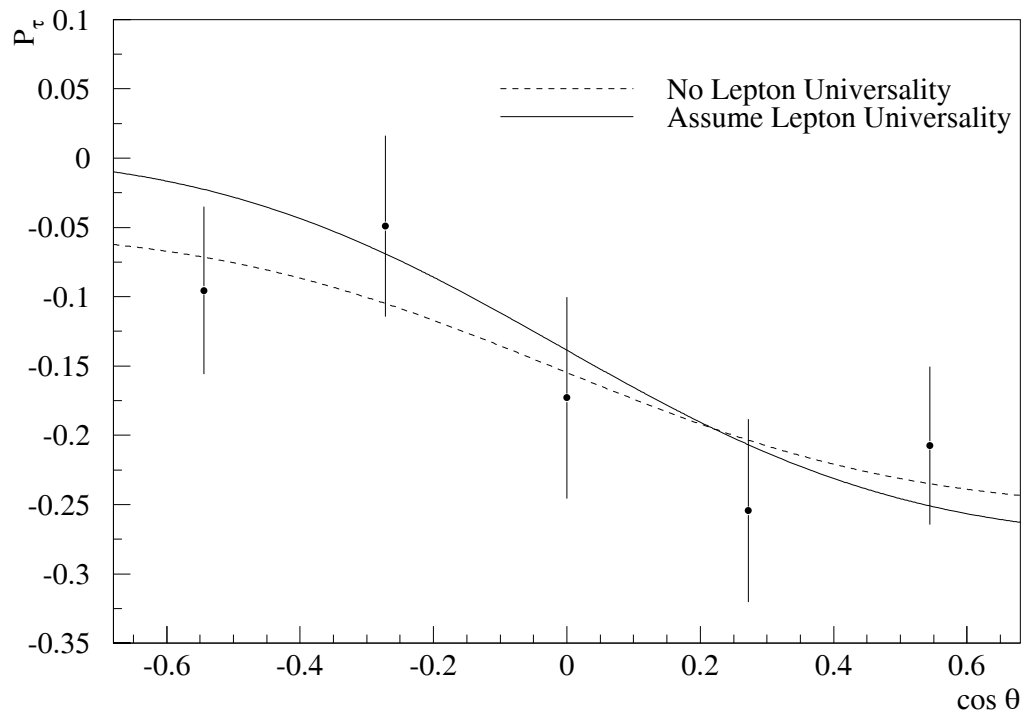


Figure 5.4: This figure shows the measured polarization as a function of  $\cos \theta$ . The data points are the values determined with  $\sigma_{ij}^{\text{fit}}$  included in the definition of  $\chi_{\cos \theta}^2$ . The error bars are the data statistical errors only. The dotted curve represents the fitted theoretical model without assuming lepton universality, and the solid curve represents the fitted model assuming lepton universality.

Source of uncertainty	$\delta A_{\text{FB}}^{\text{Pol}^-}$ (%)	$\delta A_{\text{FB}}^{\text{Pol}^+}$ (%)	$\delta \langle P_\tau \rangle^-$ (%)	$\delta \langle P_\tau \rangle^+$ (%)	$\delta A_{e\tau}^-$ (%)	$\delta A_{e\tau}^+$ (%)
MC statistics	1.40	1.40	1.21	1.21	1.03	1.03
Energy scale	0.07	0.10	0.37	0.29	0.23	0.19
Energy resolution	0.00	0.12	0.36	0.00	0.21	0.00
Momentum resolution	0.44	0.26	0.29	0.00	0.38	0.00
Decay radiation effect	0.00	0.01	0.38	0.00	0.27	0.00
$\rho$ BR error	0.01	0.01	0.24	0.23	0.18	0.17
non- $\rho$ BR errors	0.02	0.02	0.37	0.37	0.27	0.27
$a_1$ shape	0.09	0.07	0.10	0.14	0.05	0.07
$A_{\text{FB}}$ error	0.13	0.13	0.05	0.05	0.00	0.00
Total systematic	1.48	1.44	1.47	1.32	1.22	1.10

Table 5.2: This table lists the contributions to the systematic errors on the quantities measured in this analysis. The average  $\tau$  polarization,  $\langle P_\tau \rangle$ , and the forward-backward tau polarization asymmetry,  $A_{\text{FB}}^{\text{Pol}}$ , do not assume lepton universality. The lepton asymmetry,  $A_{e\tau}$ , is determined assuming lepton universality.

Contributor	$\delta A_{\text{FB}}^{\text{Pol}}$ (%)	$\delta \langle P_\tau \rangle$ (%)	$\delta A_{e\tau}$ (%)
$C_{ij}^\pm$	1.387	1.195	1.015
$I_{ij}^\pm$	0.174	0.146	0.129
Total	1.399	1.206	1.026

Table 5.3: Contributions to the Monte Carlo statistical error from the correction factors,  $C_{ij}^\pm$ , and the Monte Carlo generated theoretical function,  $I_{ij}^\pm$ .

The Monte Carlo statistic error is determined by taking the quadratic difference between the errors returned from the fit with and without the term  $\sigma_{ij}^{\text{fit}}$  in the denominator of  $\chi_{\cos\theta}^2$ . The individual  $I$  contributions to this term from  $C_{ij}^\pm$  and  $I_{ij}^\pm$  are given in table 5.3.

There are two systematic errors associated with the measurement of the energy in the electromagnetic calorimeter: the energy scale and the energy resolution.

The measured energy distributions in the Monte Carlo are affected by how well the amount of material in front of the electromagnetic calorimeter has been measured. To estimate the size of the uncertainty due to this effect, the measured Monte Carlo cluster energies were varied by  $\pm 0.3\%$  and the subsequent variation in the results defined as the

systematic error. In addition, below 12 GeV, the cluster energy in the Monte Carlo was found to be slightly higher than in the data. A systematic error was assigned for this effect by scaling the energy of the Monte Carlo clusters from  $-2\%$  at 2 GeV to  $0\%$  at 12 GeV, and the change in the results added in quadrature to the energy variation error described above, giving the total energy scale systematic error.

The energy resolution in the electromagnetic calorimeter is also affected by the slight uncertainties in the amount of material in front of the calorimeter. The energies measured in the Monte Carlo have been corrected by smearing the energy resolution with a Gaussian distribution with width [58]

$$\sigma_{\text{smear}}^2 = \left( 6.25 + \frac{80}{\sqrt{E}} \right) \times 10^{-4}. \quad (5.25)$$

The values of  $\langle P_\tau \rangle$  and  $A_{\text{FB}}^{\text{Pol}}$  given above include this additional smearing. To evaluate the size of the effect due to this resolution inaccuracy, the additional smearing is removed and the resulting changes in  $\langle P_\tau \rangle$  and  $A_{\text{FB}}^{\text{Pol}}$  defined as the systematic errors.

The momentum resolution in the Monte Carlo does not exactly model the resolution in the data, and so a systematic error is assigned for this effect. The transverse momentum,  $p_T$ , of each track in the Monte Carlo was smeared using a triple gaussian weighted by a factor  $\sqrt{x_T^4 + 0.3x_T^2 + 0.01x_T}$  [59], where  $x_T = p_T/E_{\text{beam}}$ , to approximate the fully-reconstructed track momentum. The width of the dominant gaussian in this smearing function was varied and the change in the asymmetries taken as the systematic uncertainty due to the momentum resolution uncertainty.

It is important to know the initial kinematics of the tau decay products so that the values of  $\cos \theta^*$  and  $\cos \psi$  can be accurately determined. Initial and final state radiation, and radiation from the decay products of the tau can all result in incorrect energy measurements as well as misidentification of the tau decay products. The initial state and final state radiation is modeled very well in the Monte Carlo, but the QED  $\mathcal{O}(\alpha)$  corrections to the tau decays are included only in the leading logarithm approximation. To evaluate a systematic error for this effect, the fully reconstructed Monte Carlo sample is analyzed in an identical manner as the data. The Monte Carlo is analyzed a second time, excluding

Decay Channel	$\delta A_{\text{FB}}^{\text{Pol}^-}$ (%)	$\delta A_{\text{FB}}^{\text{Pol}^+}$ (%)	$\delta \langle P_\tau \rangle^-$ (%)	$\delta \langle P_\tau \rangle^+$ (%)	$\delta A_{e\tau^-}$ (%)	$\delta A_{e\tau^+}$ (%)
$\tau^- \rightarrow e^- \bar{\nu}_e \nu_\tau$	0.001	0.001	0.008	0.008	0.005	0.005
$\tau^- \rightarrow \mu^- \bar{\nu}_\mu \nu_\tau$	0.001	0.001	0.007	0.007	0.004	0.005
$\tau^- \rightarrow h^+ h^- h^- \geq 0\pi^0 \nu_\tau$	0.000	0.000	0.003	0.002	0.002	0.001
$\tau^- \rightarrow h^- \nu_\tau$	0.011	0.012	0.356	0.356	0.257	0.262
$\tau^- \rightarrow h^- 2\pi^0 \nu_\tau$	0.006	0.005	0.007	0.010	0.003	0.005
$\tau^- \rightarrow h^- \geq 3\pi^0 \nu_\tau$	0.009	0.010	0.055	0.055	0.043	0.044
$\tau^- \rightarrow K^{*-} \nu_\tau$	0.011	0.011	0.092	0.090	0.070	0.069
Total	0.019	0.020	0.372	0.372	0.270	0.275

Table 5.4: Individual systematic error contributions from uncertainties in the measured branching ratios of the background channels.

events with decay radiation. Following reference [61], the systematic error is defined as the product of  $1/\ln(m_\tau/m_\rho)$  and the difference in the results with and without decay radiation.

Uncertainties in the branching ratios of the tau decay channels can affect the final results. A systematic error is assigned to the results due to the uncertainty on each of the tau decay channels. For the background channels, the total uncertainty is the quadratic sum of the individual uncertainties. Table 5.4 lists the individual background systematic errors. The largest error contribution to the average tau polarization is from  $\tau^- \rightarrow h^- \nu_\tau$ .

The largest background in the sample comes from  $\tau \rightarrow a_1 \nu_\tau$  decays where the  $a_1$  decays via  $a_1 \rightarrow h 2\pi^0$ . A systematic error is assigned to reflect the poor knowledge of the shape of the  $a_1$  resonance. Five different mass distributions were generated using KORALZ3.8 to produce 10000  $a_1$  decays for the values:

- $m_{a_1} = 1251 \text{ MeV}/c^2$  and  $\Gamma_{a_1} = 599 \text{ GeV}/c^2$  [60];
- $m_{a_1} = 1226 \text{ MeV}/c^2$  and  $\Gamma_{a_1} = 599 \text{ GeV}/c^2$ ;
- $m_{a_1} = 1276 \text{ MeV}/c^2$  and  $\Gamma_{a_1} = 599 \text{ GeV}/c^2$ ;
- $m_{a_1} = 1251 \text{ MeV}/c^2$  and  $\Gamma_{a_1} = 500 \text{ GeV}/c^2$ ;
- $m_{a_1} = 1251 \text{ MeV}/c^2$  and  $\Gamma_{a_1} = 700 \text{ GeV}/c^2$ .

Variation	$\delta A_{\text{FB}}^{\text{Pol}^-}$ (%)	$\delta A_{\text{FB}}^{\text{Pol}^+}$ (%)	$\delta \langle P_\tau \rangle^-$ (%)	$\delta \langle P_\tau \rangle^+$ (%)	$\delta A_{e\tau^-}$ (%)	$\delta A_{e\tau^+}$ (%)
$m_{a_1} = 1226$	0.049			0.104		0.055
$m_{a_1} = 1276$		0.005	0.069		0.048	
$\Gamma_{a_1} = 500$		0.065	0.073		0.026	
$\Gamma_{a_1} = 700$	0.070			0.095		0.041
Total	0.088	0.066	0.100	0.141	0.054	0.069

Table 5.5: Details of the systematic error due to uncertainty in the  $a_1$  resonance shape.

Each of the five distributions was divided into 40 four-vector mass bins between 0 and 2 GeV/c<sup>2</sup>. Weight factors for the four distributions with a non-nominal parameter were defined by the ratio of the number of events in each bin to the number of events in each bin in the nominal mass distribution. These weight factors were applied to each event of the fully reconstructed Monte Carlo as the events were entered into the  $\cos \theta^* - \cos \psi$  histograms. The resulting change in the  $\cos \theta^* - \cos \psi$  distribution alters the measured values of  $P_\tau(\cos \theta)$  and hence changes the asymmetries. The systematic uncertainty in the asymmetries due to the  $a_1$  mass distribution uncertainty is defined as the quadratic sum of the changes in the asymmetries when the mass and width are changed. These changes are shown in table 5.5.

Finally, a systematic error is assigned for the uncertainty in  $A_{\text{FB}} = 0.0165 \pm 0.0082$  [37] used in equation 2.30. The error on this quantity represents the combined statistical and systematic errors on  $A_{\text{FB}}$ . This is evaluated by varying  $A_{\text{FB}}$  by its uncertainty and observing the changes in the asymmetries.

### 5.2.3 Additional Checks on the Fitting Method

The reliability of the results is related not only to the accuracy of the model used, but also to the method of fitting the data to the model. Several cross-checks were performed to test whether the fitting method described above gave results that could be trusted.

The Monte Carlo described in Chapter 4 has been generated with  $\langle P_\tau \rangle = -0.136$  and  $A_{\text{FB}}^{\text{Pol}} = -0.102$ . We analyzed the Monte Carlo as if it were data to see if the analysis

would return the same values after the fit. The fitted values were  $\langle P_\tau \rangle = -0.141 \pm 0.012$  and  $A_{\text{FB}}^{\text{Pol}} = -0.102 \pm 0.014$ , showing no significant bias between the input and the fitted results. A further test was performed to check for possible biases for positive or negative helicity events by analyzing the positive and negative helicity events in the Monte Carlo separately. The measured values for  $\langle P_\tau \rangle$  were  $0.981 \pm 0.018$  and  $-0.996 \pm 0.012$ , showing no bias for either helicity state.

An alternate method of fitting was also used to test the results. Instead of using the high statistics four-vector Monte Carlo sample for the theoretical distributions, the fully reconstructed Monte Carlo sample in each  $\cos \theta$  bin was used to describe the theoretical shape. The results with this model are consistent with the nominal fit values.

# Chapter 6

## Discussion

In this chapter, we review the asymmetry results and compare them with previous measurements. We also discuss how these results can be used to place limits on the mass of the top quark. We then use the relationships discussed in Chapter 2 to derive a value for  $\sin^2 \hat{\theta}_W^\ell$  from these asymmetries. This result is compared to previous LEP measurements using alternate techniques.

### 6.1 Asymmetry Results

The average tau polarization asymmetry and the forward-backward tau polarization asymmetry have been measured, without assuming lepton universality, to be

$$\begin{aligned}\langle P_\tau \rangle &= (-15.5 \pm 2.8 \pm 1.4)\% \\ A_{\text{FB}}^{\text{Pol}} &= (-7.6 \pm 3.3 \pm 1.5)\% \end{aligned} \tag{6.1}$$

where the first uncertainty is statistical and the second is systematic. The lepton asymmetries  $A_\tau$  and  $A_e$  (see equations 2.21 and 2.24) are thus

$$\begin{aligned}A_\tau &= 0.155 \pm 0.028 \pm 0.014 \\ A_e &= 0.101 \pm 0.043 \pm 0.019. \end{aligned} \tag{6.2}$$

These results are consistent with the hypothesis of  $e$ - $\tau$  universality. If we fit the data under the assumption of  $e$ - $\tau$  universality, we obtain the  $e$ - $\tau$  polarization asymmetry,

$$A_{e\tau} = 0.139 \pm 0.024 \pm 0.012. \tag{6.3}$$

The four LEP experiments have published results for  $\langle P_\tau \rangle$  using the  $\tau^- \rightarrow e^- \bar{\nu}_e \nu_\tau$ ,  $\tau^- \rightarrow \mu^- \bar{\nu}_\mu \nu_\tau$ ,  $\tau^- \rightarrow \pi^- \nu_\tau$ , and  $\tau^- \rightarrow \rho^- \nu_\tau$  decay channels [62, 63, 64, 65]. ALEPH and L3 have also analyzed the  $\tau^- \rightarrow a_1^- \nu_\tau$  decay channel [62, 64]. Figure 6.1(a) shows the value measured in this analysis compared against the values quoted by the LEP experiments for the  $\tau^- \rightarrow \rho^- \nu_\tau$  channel. The OPAL result is a weighted average of the results presented in this thesis, using 1991 and 1992 data and the results of an independent analysis of OPAL data which includes 1990 data. Approximately 50% of the events are common between these two selections. We see from the figure that the results from this analysis are in excellent agreement with the LEP results.

We can also compare the polarization measured in this analysis with the results determined using other tau decay channels. Figure 6.1(b) compares the results in the  $\tau^- \rightarrow \rho^- \nu_\tau$  channel with the other decay channels for the published OPAL results [65]. Again, the OPAL  $\tau^- \rightarrow \rho^- \nu_\tau$  polarization measurement includes the results of this analysis averaged with the results from an independent analysis of OPAL data. We can see that in the  $\tau^- \rightarrow \rho^- \nu_\tau$  channel, the combination of high statistics (due to the large branching ratio) and high sensitivity to the polarization provides the lowest uncertainties compared to the other  $\tau^-$  decay channels.

The asymmetries evaluated in this analysis measure the effective couplings in the Improved Born Approximation. The weak radiative corrections included in these effective couplings are sensitive to the mass of the top quark (see Section 2.2). Thus, the measured values of the asymmetries can be used to place loose limits on the mass of the top quark. Figure 6.2 shows the variation of the lepton asymmetries  $A_\tau$ ,  $A_e$ , and  $A_\ell \equiv A_{e\tau}$  with  $m_{\text{top}}$ , and indicates the values for these asymmetries measured in this analysis. These results alone are not sufficient to place significant restrictions on allowed values of  $m_{\text{top}}$ , but are important input parameters in a global top quark mass evaluation.

## 6.2 The Effective Electroweak Mixing Angle

The tau polarization asymmetries are related to the ratio of the vector to axial-vector effective coupling strengths,  $\hat{v}/\hat{a}$ , and hence to the effective weak mixing angle for leptons,

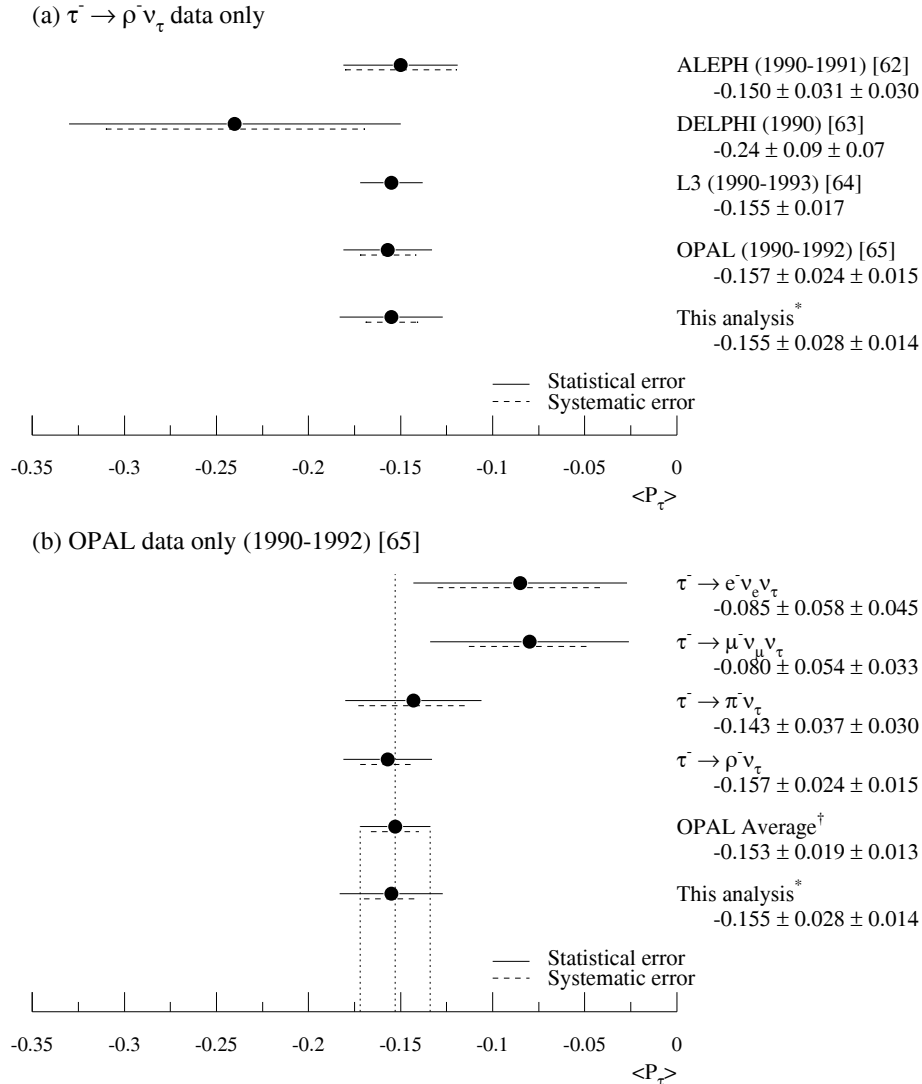


Figure 6.1: Figure (a) shows the value of  $\langle P_\tau \rangle$  measured in this thesis compared against the LEP measurements using only the  $\tau^- \rightarrow \rho^- \nu_\tau$  decay channel. The L3 result only shows the statistical error, since they do a global fit to all measured channels before evaluating systematic uncertainties. Figure (b) shows the value of  $\langle P_\tau \rangle$  measured in this thesis compared against OPAL results for the dominant  $\tau^-$  decay channels.

\*The result presented in this thesis is included in the OPAL result, as discussed in the text.

†The OPAL average has been corrected for the effects of photon propagator, photon- $Z^0$  interference, and photonic radiative corrections using ZFITTER [22].

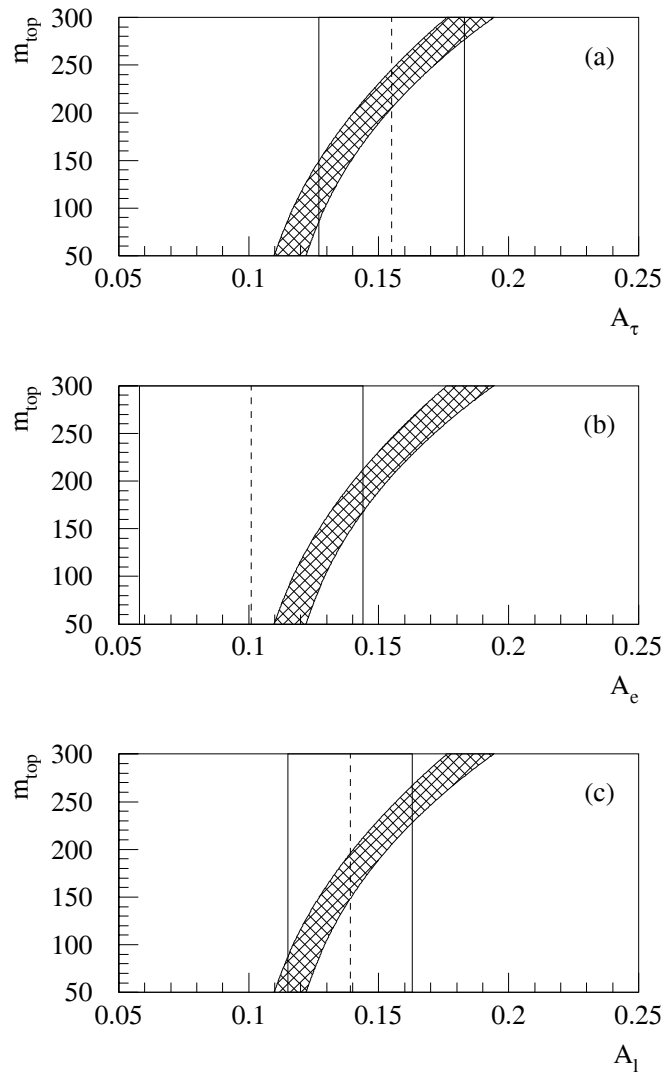


Figure 6.2: This figure shows the variation of (a)  $A_\tau$ , (b)  $A_e$ , and (c)  $A_l \equiv A_{e\tau}$  as a function of the mass of the top quark. The hatched area shows the variation of the Standard Model prediction for Higgs masses between  $50 \text{ GeV}/c^2$  and  $1000 \text{ GeV}/c^2$ . The vertical bands represent the measurements made in this analysis.

$\sin^2 \hat{\theta}_W^\ell$ , through the expressions

$$A_\ell = \frac{2\hat{v}_\ell/\hat{a}_\ell}{1 + (\hat{v}_\ell/\hat{a}_\ell)^2} \quad (6.4)$$

and

$$\frac{\hat{v}_\ell}{\hat{a}_\ell} = 1 - 4 \sin^2 \hat{\theta}_W^\ell \quad (6.5)$$

(see Chapter 2). The average tau polarization measures the coupling of the  $Z^0$  to the  $\tau^+\tau^-$  system, and gives

$$\frac{\hat{v}_\tau}{\hat{a}_\tau} = 0.078 \pm 0.014 \pm 0.007 \quad (6.6)$$

which leads to

$$\sin^2 \hat{\theta}_W^\tau = 0.2305 \pm 0.0036 \pm 0.0018. \quad (6.7)$$

Similarly, the forward-backward tau polarization asymmetry measures the coupling of the incident  $e^+e^-$  pair to the  $Z^0$ , and gives

$$\frac{\hat{v}_e}{\hat{a}_e} = 0.050 \pm 0.022 \pm 0.010 \quad (6.8)$$

leading to

$$\sin^2 \hat{\theta}_W^e = 0.2374 \pm 0.0055 \pm 0.0024. \quad (6.9)$$

The ratio of the electron and  $\tau^-$  coupling strengths is a measure of lepton universality. The values determined here give

$$R_{e\tau} \equiv \frac{(\hat{v}_e/\hat{a}_e)}{(\hat{v}_\tau/\hat{a}_\tau)} = 0.65 \pm 0.31(\text{stat}), \quad (6.10)$$

which is consistent with lepton universality. When the data is fit with the assumption of lepton universality, the lepton asymmetry,  $A_\ell$ , gives

$$\frac{\hat{v}_\ell}{\hat{a}_\ell} = 0.070 \pm 0.012 \pm 0.006, \quad (6.11)$$

leading to the value for the effective weak mixing angle for leptons of

$$\sin^2 \hat{\theta}_W^\ell = 0.2326 \pm 0.0031 \pm 0.0015. \quad (6.12)$$

The four LEP collaborations have measured the effective weak mixing angle by measuring  $\langle P_\tau \rangle$ , as discussed in the previous section, and measuring the forward-backward asymmetries,  $A_{\text{FB}}^{f\bar{f}}$ , of leptons and quarks, which are related to  $\sin^2 \hat{\theta}_W^\ell$  via

$$A_{\text{FB}}^{f\bar{f}} = \frac{3}{4} \frac{2(\hat{v}_e/\hat{a}_e)}{1 + (\hat{v}_e/\hat{a}_e)^2} \frac{2(\hat{v}_f/\hat{a}_f)}{1 + (\hat{v}_f/\hat{a}_f)^2}, \quad (6.13)$$

and

$$\frac{\hat{v}_f}{\hat{a}_f} = 1 - \frac{2 Q_f}{T_3^f} \sin^2 \hat{\theta}_W^\ell \quad (6.14)$$

(see equation 2.8). These measurements are briefly discussed below.

The  $\tau^-$  polarization measurements presented in the previous section are used to determine values of  $\sin^2 \hat{\theta}_W^\ell$  in the same manner as shown above. Figure 6.3(a) shows the results quoted by the four experiments. Again, we see that the measurement made in this thesis compares very favourably with the other LEP results. The additional  $\tau^-$  decay channels used in the LEP results reduce the uncertainties, but the  $\tau^- \rightarrow \rho^- \nu_\tau$  channel still dominates the results.

The lepton forward-backward asymmetry,  $A_{\text{FB}}^\ell$ , has been measured by the four LEP collaborations [66]-[69] using a fit to the shape of the  $Z^0$  mass resonance and the cross-sections of  $Z^0 \rightarrow \ell^+ \ell^-$  with the assumption of lepton universality. The quark forward-backward asymmetries,  $A_{\text{FB}}^{q\bar{q}}$ , are also measured by the LEP collaborations and are related to  $\sin^2 \hat{\theta}_W^\ell$ . In general, it is difficult to measure these asymmetries directly, particularly for the light quark flavours  $u$ ,  $d$ , and  $s$ . For this reason, the forward-backward charge asymmetry for all available quark flavours,  $\langle Q_{\text{FB}} \rangle$ , was measured [70]-[72]. This quantity is defined by

$$\langle Q_{\text{FB}} \rangle = \sum_{f=(u,d,s,c,b)} 2 Q_f A_{\text{FB}}^{f\bar{f}} \frac{\Gamma_{f\bar{f}}}{\Gamma_{\text{had}}}, \quad (6.15)$$

and so can be used to extract  $\sin^2 \hat{\theta}_W^\ell$  in a global fit to all available quark flavours. The dominant systematic uncertainty in this method comes from uncertainties in modeling the quark fragmentation process. More recently, the forward-backward asymmetries of the heavier  $c$  and  $b$  quarks have been successfully measured by the LEP collaborations [73]-[79] using several different techniques to identify the flavour of the primary  $q\bar{q}$  pair. Finally,

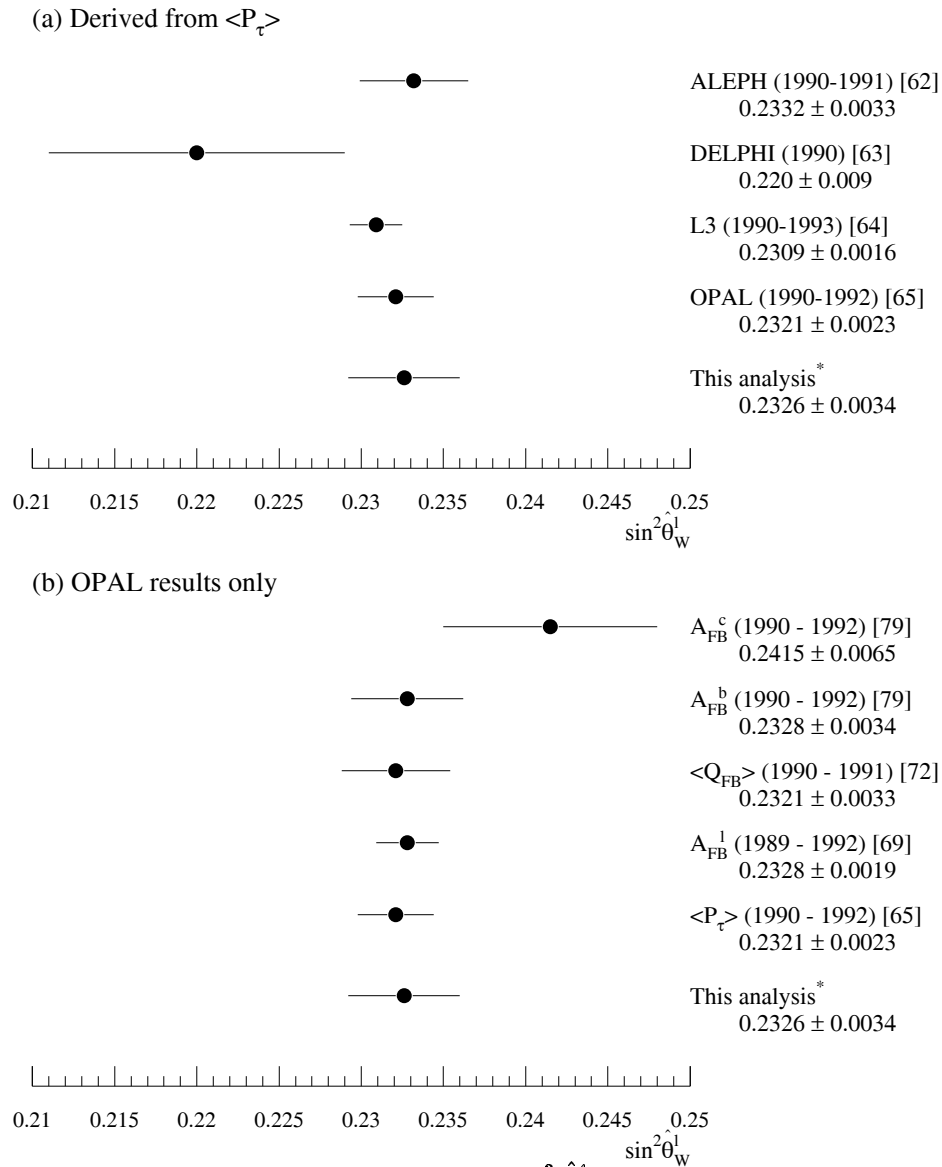


Figure 6.3: Figure (a) shows the values of  $\sin^2 \hat{\theta}_W^l$  derived from  $\langle P_\tau \rangle$  by the LEP collaborations. Figure (b) shows the OPAL results for  $\sin^2 \hat{\theta}_W^l$  derived using several different methods.

\*The result presented in this thesis is included in the OPAL result.

Measurement	Collaboration	$\sin^2 \hat{\theta}_W^\ell$	Data used	
$\langle P_\tau \rangle$	This thesis	$0.2326 \pm 0.0034$	1990-1992	
	ALEPH [62]	$0.2332 \pm 0.0022$	1990-1991	
	DELPHI [63]	$0.220 \pm 0.009$	1990	
	L3 [64]	$0.2309 \pm 0.0016$	1990-1993	
	OPAL [65]	$0.2321 \pm 0.0023$	1990-1992	
$A_{\text{FB}}^\ell$	ALEPH [66]	$0.2310 \pm 0.0019$	1989-1992	
	DELPHI [67]	$0.2306 \pm 0.0020$	1990-1992	
	L3 [68]	$0.2312 \pm 0.0022$	1990-1992	
	OPAL [69]	$0.2328 \pm 0.0019$	1989-1992	
$\langle Q_{\text{FB}} \rangle$	ALEPH [70]	$0.2300 \pm 0.0052$	1989-1990	
	DELPHI [71]	$0.2345 \pm 0.0040$	1990-1991	
	OPAL [72]	$0.2321 \pm 0.0033$	1990-1991	
$A_{\text{FB}}^{bb}$	lepton tag	ALEPH [73]	$0.2340 \pm 0.0023$	1990-1991
	lifetime tag	ALEPH [74]	$0.2315 \pm 0.0018$	1991-1993
	lepton tag + lifetime tag	DELPHI [76]	$0.2294 \pm 0.0021$	1991-1992
	lepton tag	L3 [78]	$0.2335 \pm 0.0021$	1990-1992
	lepton tag + charmed mesons	OPAL [79]	$0.2328 \pm 0.0034$	1990-1992
$A_{\text{FB}}^{c\bar{c}}$	lepton tag	ALEPH [73]	$0.2232 \pm 0.0062$	1990-1991
	charmed mesons	ALEPH [75]	$0.231 \pm 0.010$	1989-1991
	charmed mesons	DELPHI [77]	$0.2307 \pm 0.0067$	1991-1992
	lepton tag + charmed mesons	OPAL [79]	$0.2415 \pm 0.0065$	1990-1992
$A_{\text{FB}}^{s\bar{s}}$	DELPHI [80]	$0.2273 \pm 0.0050$	1992	
$A_{\text{LR}}$	SLD [80]	$0.2294 \pm 0.0010$	1992-1993	

Table 6.1: This table lists the values of  $\sin^2 \hat{\theta}_W^\ell$  derived from several measurements by the four LEP experiments, and a recent measurement of the left-right asymmetry,  $A_{\text{LR}}$ , by the SLD collaboration at SLAC.

DELPHI [80] has published the first measurement of the forward-backward asymmetry of the  $s$  quark.

Figure 6.3(b) shows the values of  $\sin^2 \hat{\theta}_W^\ell$  derived from OPAL measurements of each of these asymmetries. We can see that the tau polarization measurement provides one of the best determinations of  $\sin^2 \hat{\theta}_W^\ell$ . Table 6.1 summarizes the results quoted by the LEP experiments for each of these measurements. Again, we note that measuring  $\langle P_\tau \rangle$  is one of the most precise methods of determining the value of  $\sin^2 \hat{\theta}_W^\ell$ . This is because, even though fewer events are used to measure  $\langle P_\tau \rangle$  than are used for the other asymmetries, the

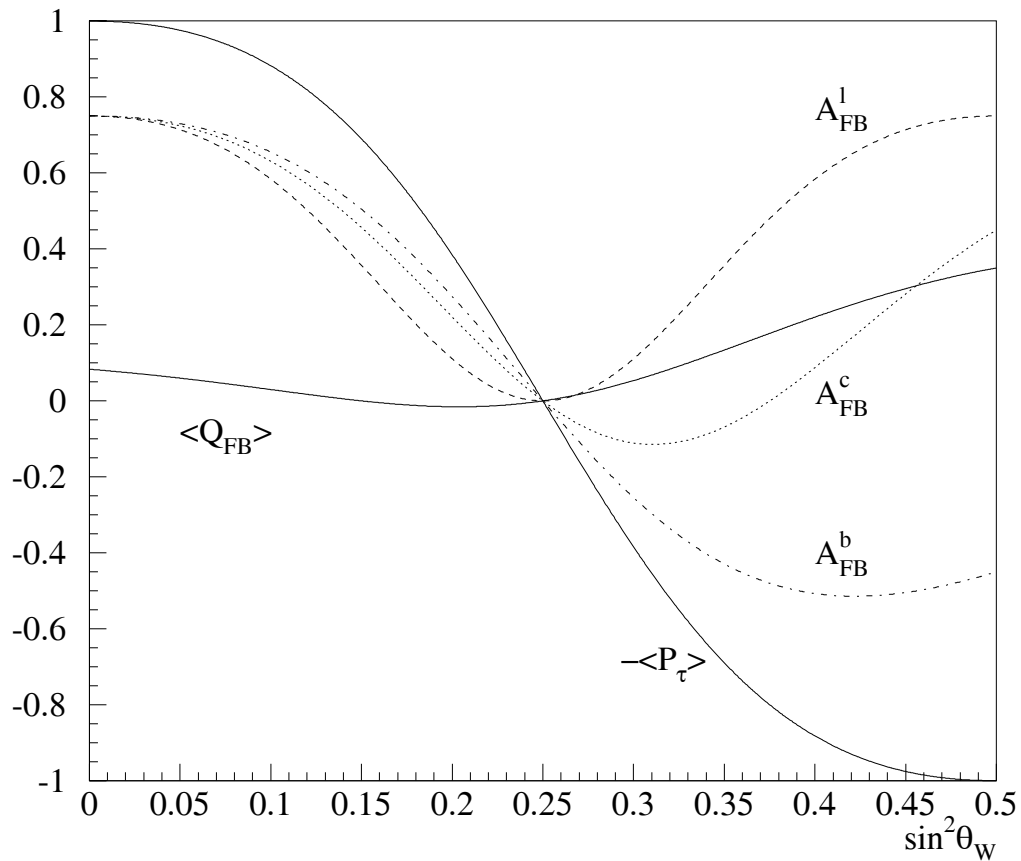


Figure 6.4: This figure shows the variations, at the Born level, of the asymmetries measured by the LEP collaborations as a function of  $\sin^2 \theta_W$ . The sign of  $\langle P_\tau \rangle$  has been changed so that a direct comparison of the slopes of the functions can be made. The tau polarization asymmetry,  $\langle P_\tau \rangle$ , is the most sensitive quantity to the value of  $\sin^2 \theta_W$ .

sensitivity of  $\langle P_\tau \rangle$  to  $\sin^2 \hat{\theta}_W^\ell$  is much higher. Figure 6.4 shows the variation at the Born level of each of the asymmetries discussed above as a function of  $\sin^2 \theta_W$ . We can see that the slope of the curve for  $\langle P_\tau \rangle$  is larger than for the other asymmetries in the region around  $\sin^2 \hat{\theta}_W^\ell \approx 0.23$ , and thus that  $\langle P_\tau \rangle$  is indeed more sensitive in this region.

# Chapter 7

## Conclusion

This thesis has described a precision test of neutral weak interactions in the Standard Model. We have measured the average tau polarization asymmetry and the forward-backward tau polarization asymmetry, which have been used to confirm the presence of parity violation in neutral weak interactions and to test the hypothesis of lepton universality. Both properties have been verified. The relative sign between the effective vector and axial-vector couplings is positive.

The ratio of the effective electron coupling strength,  $\hat{v}_e/\hat{a}_e$ , to the effective  $\tau^-$  coupling strength,  $\hat{v}_\tau/\hat{a}_\tau$ , has been measured to be

$$R_{e\tau} \equiv \frac{(\hat{v}_e/\hat{a}_e)}{(\hat{v}_\tau/\hat{a}_\tau)} = 0.65 \pm 0.31(\text{stat}). \quad (7.1)$$

This is consistent with the hypothesis of lepton universality, and is an important part of a global measurement of lepton universality.

Under the assumption of lepton universality, the effective electroweak mixing angle for leptons has been measured to be

$$\sin^2 \hat{\theta}_W^\ell = 0.2326 \pm 0.0031 \pm 0.0015, \quad (7.2)$$

in good agreement with other recent measurements of this parameter. This result is a strong contributor to the overall average of the current measurements.

This measurement can be used to place limits on the mass of the top quark. Figure 7.1 shows the variation of  $\sin^2 \hat{\theta}_W$  with  $m_{\text{top}}$  and  $m_{\text{Higgs}}$ , and displays the value of  $\sin^2 \hat{\theta}_W$  measured in this analysis. This result is not sufficient by itself to place significant

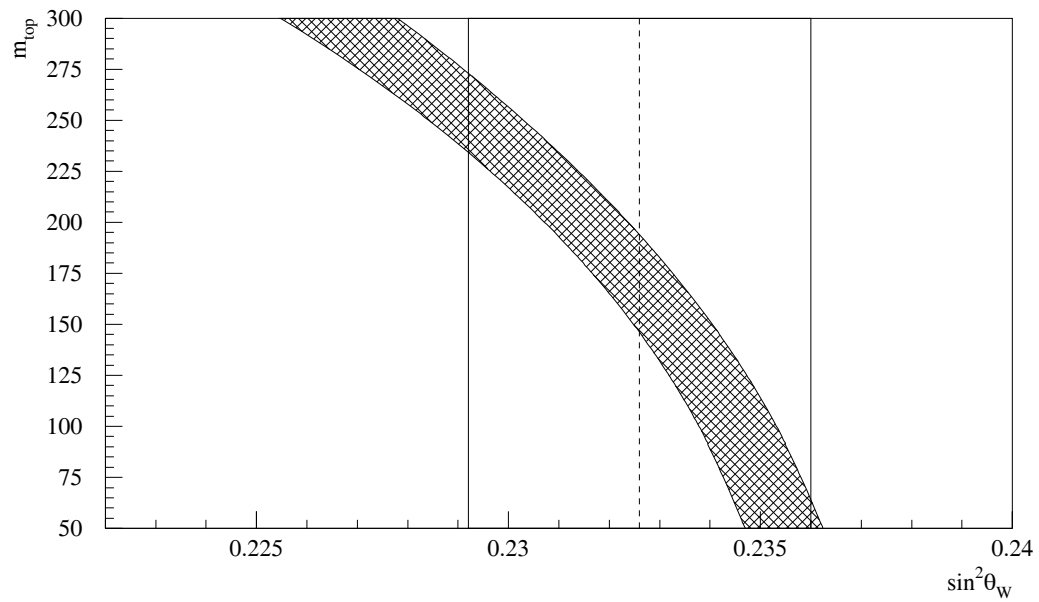


Figure 7.1: This figure shows the variation of  $\sin^2 \hat{\theta}_W$  as a function of the mass of the top quark. The hatched area shows the variation of the Standard Model prediction for Higgs masses between 50 GeV/c<sup>2</sup> and 1000 GeV/c<sup>2</sup>. The vertical band represents the value measured in this analysis.

restrictions on allowed values of  $m_{\text{top}}$ , but provides important input into a global top quark mass measurement.

# Appendix A

## $\tau^- \rightarrow h^- \pi^0 \nu_\tau$ Branching Ratio

This appendix describes the measurement of the  $\tau^- \rightarrow h^- \pi^0 \nu_\tau$  branching ratio. This measurement is compared against recent, high precision measurements to show that the selection presented in this thesis is well understood. The data and Monte Carlo event samples and the selection requirements that are used for this measurement are the same as were used for the asymmetry measurements (see Chapter 4). The only exception is that the electromagnetic cluster energy threshold is 1.4 GeV instead of 1.2 GeV to reduce the contamination from  $\tau^- \rightarrow h^- 2\pi^0 \nu_\tau$  events.

Note that we are not measuring the  $\tau^- \rightarrow \rho^- \nu_\tau$  branching ratio. The  $\tau^- \rightarrow h^- \pi^0 \nu_\tau$  branching ratio includes contributions from the  $\tau^- \rightarrow \rho^- \nu_\tau$  branching ratio and from the  $\tau^- \rightarrow K^{*-} \nu_\tau$  branching ratio, where the  $K^{*-}$  decays via  $K^{*-} \rightarrow K^- \pi^0$ . The  $\pi^- \pi^0$  and  $K^- \pi^0$  final states are difficult to separate, and so to make an accurate branching ratio measurement we determine the value for the total branching ratio  $\tau^- \rightarrow h^- \pi^0 \nu_\tau$ , where  $h^-$  represents either the  $\pi^-$  or the  $K^-$ .

The first section of this appendix outlines the procedure that is used to determine the  $\tau^- \rightarrow h^- \pi^0 \nu_\tau$  branching ratio and the second section presents the final result and a description of the systematic uncertainties. The third section compares this result with previous measurements.

## A.1 Branching Ratio Determination

The branching ratio  $B(\tau^- \rightarrow h^- \pi^0 \nu_\tau)$  is approximated by the number of  $\tau^- \rightarrow h^- \pi^0 \nu_\tau$  decays,  $N_{h\pi^0}$ , divided by the number of  $\tau^-$  decays in the data,  $N_\tau$ , and can be written as

$$B(\tau^- \rightarrow h^- \pi^0 \nu_\tau) = \frac{N_{h\pi^0}}{N_\tau}. \quad (\text{A.1})$$

The following discussion describes how this simple ratio is modified by the selection requirements.

The data sample consists of  $Z^0$  decays into any lepton pair or quark pair final state from which we select the tau pair events using the same tau pair selection as was used for the asymmetry measurements. This selection may still allow a small fraction of non-tau decays,  $f_{\text{non-}\tau}$ , into the selected tau pair sample,  $N_\tau^{\text{sel}}$ . Hence, the number of  $\tau^-$  decays in the sample is written as

$$N_\tau = (1 - f_{\text{non-}\tau}) N_\tau^{\text{sel}} \quad (\text{A.2})$$

The fraction,  $f_{\text{non-}\tau}$ , has been determined by applying the tau pair selection criteria to the non-tau pair Monte Carlo data sets described in Chapter 4, and was found to be  $(1.71 \pm 0.50)\%$  [51] (see table 4.4 for individual contributions).

The selection of  $\tau^- \rightarrow h^- \pi^0 \nu_\tau$  candidates from the tau pair sample will remove some of the  $\tau^- \rightarrow h^- \pi^0 \nu_\tau$  events from the sample, and will also allow some non- $h\pi^0$  (ie. background) events into the final event sample. The true number of  $\tau^- \rightarrow h^- \pi^0 \nu_\tau$  events in the selected tau pair sample,  $N_{h\pi^0}$ , will thus be given by the number of selected  $\tau^- \rightarrow h^- \pi^0 \nu_\tau$  candidates,  $N_{h\pi^0}^{\text{sel}}$ , corrected for the background contamination,  $f_{\text{non-}h\pi^0}$ , and the selection efficiency,  $\epsilon_{h\pi^0}$ . This gives

$$N_{h\pi^0} = \frac{(1 - f_{\text{non-}h\pi^0})}{\epsilon_{h\pi^0}} N_{h\pi^0}^{\text{sel}}, \quad (\text{A.3})$$

The selection efficiency is determined by observing the fraction of true  $\tau^- \rightarrow h^- \pi^0 \nu_\tau$  events that are removed when the  $\tau^- \rightarrow h^- \pi^0 \nu_\tau$  selection requirements are applied to the tau pair Monte Carlo.

The background contamination in the  $\tau^- \rightarrow h^- \pi^0 \nu_\tau$  sample,  $f_{\text{non-}h\pi^0}$ , depends on the branching ratios of each of the background tau decay channels. The branching ratios

used to generate the Monte Carlo were the best estimates available at that time, but many new measurements with better precision have since been made. We use these new measurements in the analysis by writing the background contamination fraction as

$$f_{\text{non-}h\pi^0} = \frac{\sum_{i \neq h\pi^0} \epsilon_i B_i}{\sum_i \epsilon_i B_i} \quad (\text{A.4})$$

where  $i$  is an index over all tau decay channels,  $\epsilon_i$  is the efficiency for selecting the decay channel  $i$  using the  $\tau^- \rightarrow h^- \pi^0 \nu_\tau$  selection requirements, and  $B_i$  is the measured branching ratio for the decay channel  $i$ . Note that this equation includes the  $\tau^- \rightarrow h^- \pi^0 \nu_\tau$  branching ratio in the denominator.

Finally, the tau pair selection requirements may preferentially remove certain event topologies, altering the apparent branching ratios in the selected tau sample. The measured branching ratio must be corrected for the selection bias,  $F_{h\pi^0}^{\text{bias}}$ , in order to determine the true branching ratio. This quantity has been estimated by applying the tau pair selection requirements to the tau pair Monte Carlo and observing the ratio of the fraction of  $\tau^- \rightarrow h^- \pi^0 \nu_\tau$  events before the selection to the fraction after the selection. This ratio is  $F_{h\pi^0}^{\text{bias}} = 1.0167 \pm 0.0028$  [82].

The  $\tau^- \rightarrow h^- \pi^0 \nu_\tau$  branching ratio is then determined by combining equations A.1, A.2, and A.3, and correcting for the tau pair selection bias, giving

$$B(\tau^- \rightarrow h^- \pi^0 \nu_\tau) = \frac{N_{h\pi^0}}{N_\tau} \frac{(1 - f_{\text{non-}h\pi^0})}{(1 - f_{\text{non-}\tau})} \frac{1}{\epsilon^{h\pi^0}} \frac{1}{F_{h\pi^0}^{\text{bias}}}. \quad (\text{A.5})$$

We substitute  $f_{\text{non-}\tau}$  from equation A.4, and observe that the resulting equation contains the  $\tau^- \rightarrow h^- \pi^0 \nu_\tau$  branching ratio on both sides of the equality. Solving for  $B(\tau^- \rightarrow h^- \pi^0 \nu_\tau)$  gives the result

$$B(\tau^- \rightarrow h^- \pi^0 \nu_\tau) = \frac{1}{\epsilon^{h\pi^0}} \left\{ K_{h\pi^0} - \sum_{i \neq h\pi^0} \epsilon_i B_i \right\} \quad (\text{A.6})$$

where

$$K_{h\pi^0} = \frac{N_{h\pi^0}}{N_\tau} \frac{1}{(1 - f_{\text{non-}\tau})} \frac{1}{F_{h\pi^0}^{\text{bias}}}. \quad (\text{A.7})$$

$N_{h\pi^0}^{\text{data}}$	10480	
$N_{\tau}^{\text{data}}$	54706	
$f_{\text{non-}\tau}$	$(1.71 \pm 0.5) \%$	
$F_{h\pi^0}^{\text{bias}}$	$1.0167 \pm 0.0028$	
Decay Channel	Selection Efficiency (%)	Branching Ratio (%)
$\tau^- \rightarrow h^- \pi^0 \nu_{\tau}$	$57.19 \pm 0.18$	(to be measured)
$\tau^- \rightarrow e^- \bar{\nu}_e \nu_{\tau}$	$0.59 \pm 0.03$	$17.93 \pm 0.26$
$\tau^- \rightarrow \mu^- \bar{\nu}_{\mu} \nu_{\tau}$	$1.09 \pm 0.04$	$17.58 \pm 0.27$
$\tau^- \rightarrow h^+ h^- h^- \geq 0\pi^0 \nu_{\tau}$	$0.16 \pm 0.02$	$14.06 \pm 0.25$
$\tau^- \rightarrow h^- \nu_{\tau}$	$6.72 \pm 0.13$	$12.6 \pm 0.4$
$\tau^- \rightarrow h^- 2\pi^0 \nu_{\tau}$	$29.65 \pm 0.25$	$8.42 \pm 0.47$
$\tau^- \rightarrow h^- \geq 3\pi^0 \nu_{\tau}$	$23.17 \pm 0.70$	$1.00 \pm 0.14$
$\tau^- \rightarrow \pi^- K^0 \nu_{\tau}$	$13.50 \pm 0.62$	$0.95 \pm 0.15$

Table A.1: This table lists the values used to determine the  $\tau^- \rightarrow h^- \pi^0 \nu_{\tau}$  branching ratio.

## A.2 Branching Ratio Results

Table A.1 lists the values that are used in equation A.6 to measure the  $\tau^- \rightarrow h^- \pi^0 \nu_{\tau}$  branching fraction and table A.2 lists the relative background contaminations in the selected sample. The measured  $\tau^- \rightarrow h^- \pi^0 \nu_{\tau}$  branching ratio is

$$B(\tau^- \rightarrow h^- \pi^0 \nu_{\tau}) = (26.37 \pm 0.30(\text{stat}) \pm 0.46(\text{syst}))\%. \quad (\text{A.8})$$

The statistical error on this measurement is determined by propagating the binomial error on the number of selected events in the final sample through equation A.6. The systematic error is determined from the quadratic sum of the individual systematic errors listed in table A.3.

The systematic errors can be divided into two types: those that arise due to uncertainty in the detector response and those that arise due to uncertainty in the input parameters of the model. These two types are discussed below.

The photons produced via  $\pi^0 \rightarrow \gamma\gamma$  can produce  $e^+e^-$  pairs in a process called photon conversion. These electrons appear as extra charged tracks, and so these events will be removed from the  $\tau^- \rightarrow h^- \pi^0 \nu_{\tau}$  sample by the single charged track requirement. The

Decay	Fraction of selected events (%)
$\tau^- \rightarrow e^- \bar{\nu}_e \nu_\tau$	$0.55 \pm 0.03$
$\tau^- \rightarrow \mu^- \bar{\nu}_\mu \nu_\tau$	$1.00 \pm 0.04$
$\tau^- \rightarrow h^+ h^- h^- \geq 0 \pi^0 \nu_\tau$	$0.12 \pm 0.01$
$\tau^- \rightarrow h^- \nu_\tau$	$4.45 \pm 0.16$
$\tau^- \rightarrow h^- 2\pi^0 \nu_\tau$	$13.38 \pm 0.65$
$\tau^- \rightarrow h^- \geq 3\pi^0 \nu_\tau$	$1.21 \pm 0.17$
$\tau^- \rightarrow \pi^- K^0 \nu_\tau$	$0.67 \pm 0.11$
Total	$21.37 \pm 0.71$

Table A.2: Relative backgrounds in the final sample as estimated from the Monte Carlo.

Source of uncertainty	$\delta B^-$ (%)	$\delta B^+$ (%)
Detector response:		
Photon conversions	0.264	0.264
Energy scale	0.003	0.000
Energy resolution	0.048	0.000
Energy correction	0.019	0.039
$z$ -detector requirement	0.117	0.000
$x_{\min}$	0.000	0.111
Model uncertainties:		
$\epsilon_{h\pi^0}$	0.084	0.084
$F_{h\pi^0}^{\text{bias}}$	0.092	0.092
$f_{\text{non-}\tau}$	0.171	0.171
$f_{\text{non-}h\pi^0}$	0.269	0.269
$B(\tau^- \rightarrow K^{*-} \nu_\tau)$	0.000	0.133
$B(\tau^- \rightarrow h^- 4\pi^0 \nu_\tau)$	0.158	0.158
$B(\tau^- \rightarrow \pi^- \eta \pi^0 \nu_\tau)$	0.066	0.066
$B(\tau^- \rightarrow \pi^- \omega \nu_\tau)$	0.139	0.139
Total systematic	0.501	0.516

Table A.3: Contributions to the systematic error of the  $\tau^- \rightarrow h^- \pi^0 \nu_\tau$  branching ratio.

$\pi^0$  can also decay via  $\pi^0 \rightarrow e^+e^-\gamma$ , and these events will also be removed from the final event sample. Approximately 10% of the true  $\tau^- \rightarrow h^-\pi^0\nu_\tau$  events in the Monte Carlo have more than one charged track. Studies indicate [51] that the data and Monte Carlo agree to about 10% on photon conversions, and so the uncertainty in the  $\tau^- \rightarrow h^-\pi^0\nu_\tau$  selection efficiency is estimated to be 1%. The Monte Carlo appears to model the  $\pi^0 \rightarrow e^+e^-\gamma$  decay properly, so no additional uncertainty is assigned for this decay. The uncertainty in the branching ratio is thus defined as 1% of  $B(\tau^- \rightarrow h^-\pi^0\nu_\tau)$ .

The uncertainties in the Monte Carlo energy scale and resolution are evaluated in the same manner as for the asymmetry measurement. In addition, a systematic error is assigned to uncertainties in the energy calibration of the electromagnetic calorimeter. The raw energy measured in the calorimeter is adjusted to compensate for early electromagnetic showers in the material in front of the calorimeter. The corrections used in previous OPAL analyses have used the approximation that energy in the electromagnetic calorimeter is deposited by an electron showering in the magnetic coil. In this analysis, we assume that the energy is deposited by a photon and thus requires a different correction. Since photons have a lower probability of interacting before reaching the calorimeter than electrons do, the correction factor is reduced to one third of the equivalent electron correction factor. To estimate the effect of choosing this particular fraction, the analysis was performed with fractions from one fifth to one half of the electron correction factor, and the change in the result taken as the systematic error.

The  $z$ -chambers are designed to help determine the  $z$ -coordinates of the charged track endpoints. The analysis presented here only uses information from the  $z$ -chambers to help determine the momenta of charged tracks. This detector is not fully efficient, however, and so not all measured track momenta will include  $z$ -chamber information, resulting in a bias in the measurement of the branching ratio. A systematic uncertainty was assigned to this effect by measuring the branching ratio using only events with  $z$ -chamber information for the charged tracks. The change in the branching ratio with this additional requirement was quoted as the  $z$ -detector systematic uncertainty.

The last detector-related systematic arises from the application of the selection re-

quirement on the quantity  $x \equiv p_{\text{trk}}/E_{\text{CM}} > 0.05$ . Low energy muons and pions can range out in the electromagnetic calorimeter and the energy which they deposit can mimic the signature of  $\tau^- \rightarrow h^- \pi^0 \nu_\tau$  decays. The effect of this requirement on the branching ratio was estimated by removing the requirement and observing the resulting change in the branching ratio. This change was recorded as a systematic uncertainty on the branching ratio.

The second type of systematic errors arises from uncertainties in the input parameters to the Monte Carlo model. These include the uncertainties in  $\epsilon_{h\pi^0}$ ,  $f_{\text{non-}h\pi^0}$ ,  $f_{\text{non-}\tau}$ , and  $F_{h\pi^0}^{\text{bias}}$ , and uncertainties due to  $\tau^-$  decay channels that are not modeled in the Monte Carlo.

The uncertainties in the  $\tau^- \rightarrow h^- \pi^0 \nu_\tau$  branching ratio due to uncertainties in the  $\tau^- \rightarrow h^- \pi^0 \nu_\tau$  efficiency, the bias correction, and the non- $\tau$  background systematic errors are determined by propagating the uncertainty on each of these parameters through equation A.6. The non- $h\pi^0$  background uncertainty is determined by summing the uncertainties for each background  $\tau^-$  decay channel in quadrature. Each background decay channel has an uncertainty due to the statistical uncertainty on the selection efficiency and an uncertainty due to the quoted uncertainty on the branching ratio measurement (see table A.1). These two uncertainties are propagated through equation A.6 and summed in quadrature to give the  $\tau^- \rightarrow h^- \pi^0 \nu_\tau$  branching ratio uncertainty for each background channel. The uncertainty for each channel is then summed in quadrature to give the total non- $h\pi^0$  background uncertainty on  $B(\tau^- \rightarrow h^- \pi^0 \nu_\tau)$ .

The selection efficiencies for the  $\pi^- \pi^0$  and  $K^- \pi^0$  final states may not be equal, and so may affect the  $\tau^- \rightarrow h^- \pi^0 \nu_\tau$  selection efficiency. The uncertainty in  $\epsilon_{h\pi^0}$  from this effect is estimated by varying the  $\tau^- \rightarrow K^{*-} \nu_\tau$  branching ratio by  $\pm 100\%$  of its quoted value (see table 4.3). This has the effect of altering the relative contribution of the  $K^- \pi^0$  final state in the selected events. The resulting change in the  $\tau^- \rightarrow h^- \pi^0 \nu_\tau$  branching ratio is defined as the systematic uncertainty due to this effect.

Finally, there are decays of the tau lepton which are not included in the KORALZ3.8 event generator, such as  $\tau^- \rightarrow h^- 4\pi^0 \nu_\tau$ ,  $\tau^- \rightarrow \pi^- \eta \pi^0 \nu_\tau$  and  $\tau^- \rightarrow \pi^- \omega \nu_\tau$ . To estimate the uncertainty on the  $\tau^- \rightarrow h^- \pi^0 \nu_\tau$  branching ratio from the exclusion of these

decays, 100% of the measured branching ratio for each decay is quoted as the systematic uncertainty in the  $\tau^- \rightarrow h^- \pi^0 \nu_\tau$  branching ratio.

CLEO has published a result [49] for the branching ratio of  $\tau^- \rightarrow h^- 4\pi^0 \nu_\tau$  relative to the branching ratio for  $\tau^- \rightarrow h^- \pi^0 \nu_\tau$ . Using the  $B(\tau^- \rightarrow h^- \pi^0 \nu_\tau)$  determined in this analysis, a value of 0.16% is found for the  $\tau^- \rightarrow h^- 4\pi^0 \nu_\tau$  branching ratio.

CLEO has also observed the decay  $\tau^- \rightarrow \pi^- \eta \pi^0 \nu_\tau$  [83], with a branching ratio of  $(0.17 \pm 0.02 \pm 0.02)\%$ . The charged decay modes of the  $\eta$  will give multiple charged tracks in the final state of the tau decay, and so will not have an effect on the  $\tau^- \rightarrow h^- \pi^0 \nu_\tau$  branching ratio. The neutral decay modes of the  $\eta$  account for about 71% of the  $\eta$  decays, with 39%  $\eta \rightarrow 2\gamma$  and 32%  $\eta \rightarrow 3\pi^0$ . The  $3\pi^0$  decay is included in the earlier CLEO measurement of  $\tau^- \rightarrow h^- 4\pi^0 \nu_\tau$  and so should not be included as an additional systematic. The two photon decay of the  $\eta$  is, however, included as a 0.07% uncertainty on the  $\tau^- \rightarrow h^- \pi^0 \nu_\tau$  branching ratio.

The  $\tau^- \rightarrow \pi^- \omega \nu_\tau$  branching ratio has been measured by CLEO [84] to be  $(1.60 \pm 0.27 \pm 0.41)\%$  and by ARGUS [85] to be  $(1.65 \pm 0.3 \pm 0.2)\%$ . Since the  $\omega$  decays into a  $\pi^0 \gamma$  final state about 8.5% of the time, this could contribute to the  $h\pi^0$  signal. A systematic error of 0.14% is quoted for this decay.

### A.3 Discussion

The branching ratio for  $\tau^- \rightarrow h^- \pi^0 \nu_\tau$  measured here is  $(26.37 \pm 0.30 \pm 0.50)\%$ . Figure A.1 shows this value in comparison with previous measurements of the branching ratio. Some of the published branching ratios are for  $\tau^- \rightarrow \pi^- \pi^0 \nu_\tau$  instead of  $\tau^- \rightarrow h^- \pi^0 \nu_\tau$ . The figure shows these values adjusted for the  $K^- \pi^0$  contribution by adding 0.5% to the quoted branching ratio.

The measured  $\tau^- \rightarrow h^- \pi^0 \nu_\tau$  branching ratio is strongly dependent on the branching ratios of the background decay channels. The dominant background in the  $\tau^- \rightarrow h^- \pi^0 \nu_\tau$  channel is the decay  $\tau^- \rightarrow h^- \geq 2\pi^0 \nu_\tau$ , for which the measured branching ratio has varied significantly in the literature. The  $\tau^- \rightarrow h^- \geq 2\pi^0 \nu_\tau$  branching ratios for this analysis are taken from the most recent results available from CLEO [49] which are somewhat

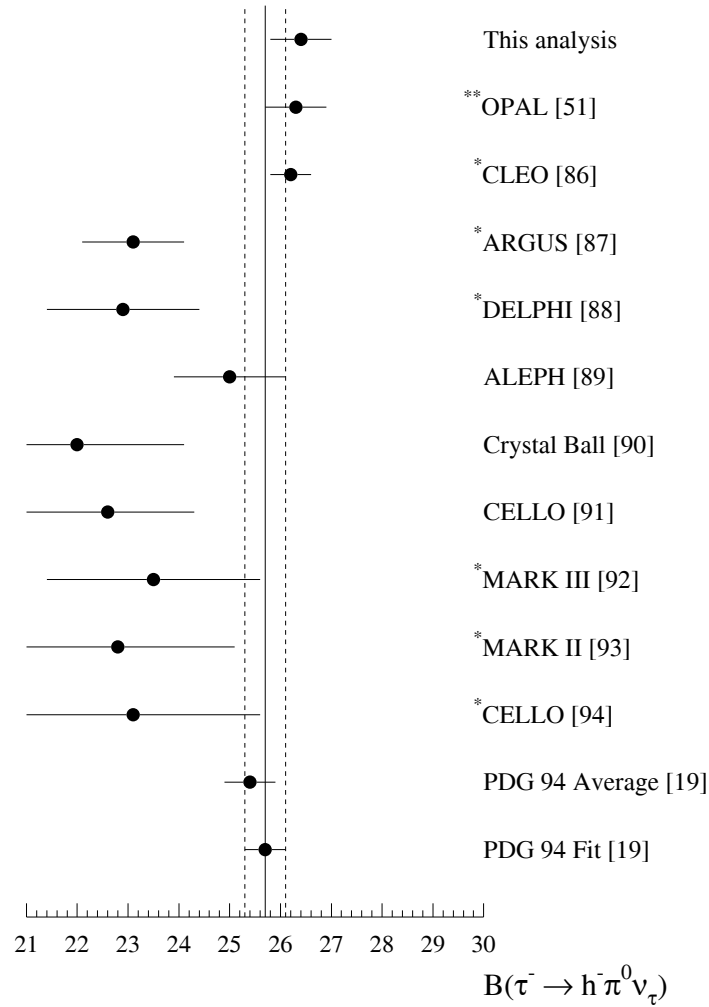


Figure A.1: This figure shows the branching ratio measured in this analysis in comparison with previous measurements. The Particle Data Group (PDG) results are evaluated using the results referenced in this diagram (excluding the Mark II and Mark III results).

\*These values have been published as  $B(\tau^- \rightarrow \rho^- \nu_\tau)$  or  $B(\tau^- \rightarrow \pi^- \pi^0 \nu_\tau)$ , and have been adjusted for  $K^- \pi^0$  contributions.

\*\*The OPAL results determined from a coupled analysis using the  $\tau^- \rightarrow h^- \pi^0 \nu_\tau$  selection presented in this thesis and a separate  $\tau^- \rightarrow h^- \geq 2\pi^0 \nu_\tau$  selection.

lower than some other measurements. This results in a slightly higher branching ratio for the  $\tau^- \rightarrow h^- \pi^0 \nu_\tau$  decay. A coupled analysis [51] has been performed using the selection requirements presented here and a separate set of selection requirements for  $\tau^- \rightarrow h^- \geq 2\pi^0 \nu_\tau$  events, with both selections using OPAL data. The results from the coupled analysis are

$$B(\tau^- \rightarrow h^- \pi^0 \nu_\tau) = (26.25 \pm 0.36 \pm 0.52)\%$$

$$B(\tau^- \rightarrow h^- \geq 2\pi^0 \nu_\tau) = (9.89 \pm 0.34 \pm 0.55)\%,$$

which is in excellent agreement with the result presented here.

# Appendix B

## Derivation of $\chi^2_{\cos\theta}(P_\tau)$ Fit Parameters

This appendix presents the derivation of the Monte Carlo dependent quantities in the  $\chi^2$  equation used to fit  $P_\tau(\cos\theta)$  (see equation 5.15),

$$\chi^2_{\cos\theta}(P_\tau) = \sum_{i=1, j=1}^{5,5} \frac{(f_{ij}^{\text{data}} - f_{ij}^{\text{fit}})^2}{(\sigma_{ij}^{\text{data}})^2 + (\sigma_{ij}^{\text{fit}})^2}. \quad (\text{B.1})$$

The first section shows the derivation of the function,  $f_{ij}^{\text{fit}}$ , which is used to model the data, and the second section shows the derivation of the Monte Carlo statistical error,  $\sigma_{ij}^{\text{fit}}$ .

### B.1 Derivation of Fit Function

This section presents the derivation of the function,  $f_{ij}^{\text{fit}}$ , used to model the data (see equation 5.14). This function, which varies with  $P_\tau$ , describes the fraction of events that we expect to measure in each  $\cos\theta^*$ - $\cos\psi$  bin after the detector resolution effects and data selection requirements have been applied to the data.

We begin with a pure sample of Monte Carlo generated  $\tau^- \rightarrow \rho^- \nu_\tau$  events, for which we know the helicity of each  $\tau^-$ . We approximate the effects of the detector resolution and the data selection requirements on this sample by applying the correction factors defined in Chapter 5. This determines the approximate number of events (including background events) we would expect to find in each  $\cos\theta^*$ - $\cos\psi$  bin after the selection. We divide this quantity by the total number of events to get the fraction that we desire.

The high-statistics Monte Carlo described in Chapter 5 can be divided into positive and negative helicity states, with  $T^\pm = \sum_{ij} T_{ij}^\pm$ . The polarization of the events in this distribution is given by

$$P_\tau = \frac{T^+ - T^-}{T^+ + T^-}. \quad (\text{B.2})$$

We can approximate the effects of the selection criteria on  $T^\pm$  by applying the correction factors,  $C_{ij}^\pm$ , as defined in Chapter 5 to the contents of each bin,  $T_{ij}^\pm$ . This gives

$$T_{(\text{sel}) ij}^\pm = C_{ij}^\pm T_{ij}^\pm, \quad (\text{B.3})$$

The total number of positive and negative helicity state events after selection is then approximated by

$$T_{(\text{sel})}^\pm = \left( \sum_{lm} C_{lm}^\pm I_{lm}^\pm \right) T^\pm \equiv C^\pm T^\pm, \quad (\text{B.4})$$

where  $I_{ij}^\pm = T_{ij}^\pm / T^\pm$ . If we solve this equation for  $T^\pm$  and substitute into equation B.2 we get

$$P_\tau = \frac{T_{(\text{sel})}^+ / C^+ - T_{(\text{sel})}^- / C^-}{T_{(\text{sel})}^+ / C^+ + T_{(\text{sel})}^- / C^-} \quad (\text{B.5})$$

which can be solved for  $T_{(\text{sel})}^-$  giving

$$T_{(\text{sel})}^- = \frac{(1 - P_\tau)C^-}{(1 + P_\tau)C^+} T_{(\text{sel})}^+. \quad (\text{B.6})$$

By definition,

$$T_{(\text{sel})} \equiv T_{(\text{sel})}^+ + T_{(\text{sel})}^-, \quad (\text{B.7})$$

from which, substituting for  $T_{(\text{sel})}^-$  from equation B.6 and solving for  $T_{(\text{sel})}^+$ , we get

$$T_{(\text{sel})}^+ = \frac{(1 + P_\tau)C^+ T_{(\text{sel})}}{(1 + P_\tau)C^+ + (1 - P_\tau)C^-}. \quad (\text{B.8})$$

A similar expression for  $T_{(\text{sel})}^-$  can be obtained by solving equation B.5 for  $T_{(\text{sel})}^+$  and substituting into equation B.7. This gives

$$T_{(\text{sel})}^- = \frac{(1 - P_\tau)C^- T_{(\text{sel})}}{(1 + P_\tau)C^+ + (1 - P_\tau)C^-}. \quad (\text{B.9})$$

Equation B.7 is also valid in each  $\cos \theta^* - \cos \psi$  bin, ie.

$$T_{(\text{sel}) ij} = T_{(\text{sel}) ij}^+ + T_{(\text{sel}) ij}^-. \quad (\text{B.10})$$

This can be rewritten as

$$T_{(\text{sel}) ij} = T_{(\text{sel})}^+ \left( \frac{T_{(\text{sel}) ij}^+}{T_{(\text{sel})}^+} \right) + T_{(\text{sel})}^- \left( \frac{T_{(\text{sel}) ij}^-}{T_{(\text{sel})}^-} \right). \quad (\text{B.11})$$

Substituting equations B.8 and B.9 for  $T_{(\text{sel})}^\pm$  in the numerator, equation B.4 in the denominator, and equation B.3 for  $T_{(\text{sel}) ij}^\pm$ , we get

$$\begin{aligned} T_{(\text{sel}) ij} &= \frac{(1 + P_\tau)C^+T_{(\text{sel})}}{(1 + P_\tau)C^+ + (1 - P_\tau)C^-} \left( \frac{C_{ij}^+T_{ij}^+}{C^+T^+} \right) \\ &+ \frac{(1 - P_\tau)C^-T_{(\text{sel})}}{(1 + P_\tau)C^+ + (1 - P_\tau)C^-} \left( \frac{C_{ij}^-T_{ij}^-}{C^-T^-} \right). \end{aligned} \quad (\text{B.12})$$

We divide both sides of this equation by  $T_{(\text{sel})}$ , giving the fraction of events in bin  $ij$ ,

$$f_{ij}^{\text{fit}} = \frac{(1 + P_\tau)C_{ij}^+I_{ij}^+ + (1 - P_\tau)C_{ij}^-I_{ij}^-}{(1 + P_\tau)\sum_{lm} C_{lm}^+I_{lm}^+ + (1 - P_\tau)\sum_{lm} C_{lm}^-I_{lm}^-}. \quad (\text{B.13})$$

This is the equation which is used to model the data.

## B.2 Monte Carlo Statistical Errors

The Monte Carlo statistical errors are determined from

$$(\sigma_{ij}^{\text{fit}})^2 = \left( \frac{\partial f_{ij}^{\text{fit}}}{\partial C_{ij}^\pm} \right)^2 \sigma_{C_{ij}^\pm}^2 + \left( \frac{\partial f_{ij}^{\text{fit}}}{\partial I_{ij}^\pm} \right)^2 \sigma_{I_{ij}^\pm}^2. \quad (\text{B.14})$$

The derivatives are given by

$$\frac{\partial f_{ij}^{\text{fit}}}{\partial C_{ij}^\pm} = \frac{(1 \pm P_\tau)(1 - f_{ij}^{\text{fit}})I_{ij}^\pm}{(1 + P_\tau)\sum_{lm} C_{lm}^+I_{lm}^+ + (1 - P_\tau)\sum_{lm} C_{lm}^-I_{lm}^-} \quad (\text{B.15})$$

and

$$\frac{\partial f_{ij}^{\text{fit}}}{\partial I_{ij}^\pm} = \frac{(1 \pm P_\tau)(1 - f_{ij}^{\text{fit}})C_{ij}^\pm}{(1 + P_\tau)\sum_{lm} C_{lm}^+I_{lm}^+ + (1 - P_\tau)\sum_{lm} C_{lm}^-I_{lm}^-}. \quad (\text{B.16})$$

The statistical errors from the high statistics four-vector Monte Carlo are the binomial errors on  $I_{ij}^\pm$ ,

$$\sigma_{I_{ij}^\pm}^2 = \frac{I_{ij}^\pm(1 - I_{ij}^\pm)}{T^\pm}. \quad (\text{B.17})$$

The statistical errors on  $C_{ij}^\pm$  are composed of a binomial error and a Poisson error. The correction factors are given by (see equation 5.13)

$$C_{ij}^\pm = \frac{N_{(\text{sel}) ij}^\pm}{\mathcal{N}_{(\rho) ij}^\pm}. \quad (\text{B.18})$$

The numerator can be divided into two parts,

$$N_{(\text{sel}) ij}^{\pm} = N_{(\text{nonmigrated}) ij}^{\pm} + N_{(\text{migrated}) ij}^{\pm}, \quad (\text{B.19})$$

where  $N_{(\text{nonmigrated}) ij}^{\pm}$  represents the number of true  $\tau^- \rightarrow \rho^- \nu_{\tau}$  events in the final selection for which the bin number is the same for the four-vector  $\cos \theta^* - \cos \psi$  as for the reconstructed  $\cos \theta^* - \cos \psi$  (ie. the detector resolution has not ‘migrated’ the events out of the four-vector bin  $ij$ ). This quantity is a subset of  $\mathcal{N}_{(\rho) ij}^{(\text{all}) \pm}$ , so the error due to this term must be treated as a binomial error.  $N_{(\text{migrated}) ij}^{\pm}$  represents the rest of the events in bin  $ij$  in the final sample. These include background events for which four-vector  $\cos \theta^* - \cos \psi$  values do not exist, and  $\tau^- \rightarrow \rho^- \nu_{\tau}$  events for which the reconstructed  $\cos \theta^* - \cos \psi$  place the event in bin  $ij$ , even though the four-vector  $\cos \theta^* - \cos \psi$  values are within a different bin. This quantity is unrelated to the denominator of  $C_{ij}^{\pm}$ , and so is treated as a Poisson error. The errors on the bin-by-bin correction factors are given by

$$\begin{aligned} \sigma_{C_{ij}^{\pm}}^2 &= \frac{N_{(\text{nonmigrated}) ij}^{\pm} (\mathcal{N}_{(\rho) ij}^{(\text{all}) \pm} - N_{(\text{nonmigrated}) ij}^{\pm})}{(\mathcal{N}_{(\rho) ij}^{(\text{all}) \pm})^3} \\ &+ \left[ \frac{N_{(\text{migrated}) ij}^{\pm}}{\mathcal{N}_{(\rho) ij}^{(\text{all}) \pm}} \right]^2 \left( \frac{1}{N_{(\text{migrated}) ij}^{\pm}} + \frac{1}{\mathcal{N}_{(\rho) ij}^{(\text{all}) \pm}} \right) \end{aligned} \quad (\text{B.20})$$

Combining equations B.14, B.15, and B.16, and using the relationships in equations B.20 and B.17, we find the Monte Carlo statistical error to be

$$\begin{aligned} (\sigma_{ij}^{\text{fit}})^2 &= \left( \frac{1 - f_{ij}^{\text{fit}}}{(1 + P_{\tau}) \sum_{lm} C_{lm}^+ I_{lm}^+ + (1 - P_{\tau}) \sum_{lm} C_{lm}^- I_{lm}^-} \right)^2 \\ &\times \sum_{+,-} (1 \pm P_{\tau})^2 \left[ \sigma_{C_{ij}^{\pm}}^2 (I_{ij}^{\pm})^2 + (C_{ij}^{\pm})^2 \sigma_{I_{ij}^{\pm}}^2 \right] \end{aligned} \quad (\text{B.21})$$

where the summation,  $\sum_{+,-}$ , is over the positive and negative helicity terms.

# Bibliography

- [1] C.D. Ellis and W.A. Wooster, *Proc. Roy. Soc. (London)* **A117** (1927) 109.
- [2] F. Reines and C.L. Cowan, Jr., *Phys. Rev.* **92** (1953) 830.
- [3] T.D. Lee and C.N. Yang, *Phys. Rev.* **104** (1956) 254.
- [4] C.S. Wu, E. Ambler, R.W. Hayward, D.D. Hoppes, and R.P. Hudson, *Phys. Rev.* **105** (1957) 1413.
- [5] E. Ambler, R.W. Hayward, D.D. Hoppes, R.P. Hudson, and C.S. Wu, *Phys. Rev.* **106** (1957) 1361.
- [6] F. Boehm and A.H. Wapstra, *Phys. Rev.* **109** (1958) 456.
- [7] M. Goldhaber, L. Grodzins, and A.W. Sunyar, *Phys. Rev.* **109** (1958) 1015.
- [8] S.L. Glashow, *Nucl. Phys.* **B 22** (1961) 579;  
S. Weinberg, *Phys. Rev. Lett.*, **19** (1967) 1264;  
A. Salam, in: *Elementary Particle Theory, Proc. of the 8th Nobel Symp.*, ed. N. Svartholm (Almqvist and Wiksell, Stockholm, 1968), p. 367.
- [9] D.C. Cundy, *et al.*, *Phys. Lett.* **31B** (1970) 478.
- [10] F.J. Hasert, *et al.*, *Phys. Lett.* **46B** (1973) 121;  
F.J. Hasert, *et al.*, *Nucl. Phys.* **B73** (1974) 1.
- [11] G. Arnison, *et al.*, *Phys. Lett.* **122B** (1983) 103.
- [12] M. Banner, *et al.*, *Phys. Lett.* **122B** (1983) 476.

- [13] CDF Collaboration, F.Abe, *et al.*, FERMILAB-PUB-94/116-E, May 1994.
- [14] I.J.R. Aitchison and A.J.G. Hey, *Gauge Theories in Particle Physics* - 2nd ed., Adam Hilger, Bristol and Philadelphia, 1989.
- [15] F. Halzen and A.D. Martin, *Quarks and Leptons: An Introductory Course in Modern Particle Physics*, John Wiley & Sons, New York, 1984.
- [16] S. Jadach and Z Wąs, *Z Physics at LEP I*, ed. G. Altarelli, R. Kleiss, and C. Verzegnassi, CERN 89-08, Vol 1 (1989) 235.
- [17] H. Burkhardt, F. Jegerlehner, G. Penso, C. Verzegnassi, *Z. Phys. C* **43** (1989) 497.
- [18] G. Altarelli, R. Barbieri, S. Jadach, *Nucl. Phys.* **B369** (1992) 3.
- [19] Particle Data Group, L. Montanet, *et al.* *Phys. Rev.* **D50** (1994) 1.
- [20] M. Consoli and W. Hollik, *Z Physics at LEP I*, ed. G. Altarelli, R. Kleiss, and C. Verzegnassi, CERN 89-08, Vol 1, p. 7
- [21] D. Schaile, *Fortsch. Phys.* **42** (1994) 429.
- [22] D. Bardin, *et al.*, CERN-TH. 6443/92 (1992) (ZFITTER).
- [23] "Tau decays as polarization analyzers," André Rougé, Invited talk given at the Workshop on Tau Lepton Physics, Orsay, France (1990).
- [24] M.L. Perl, *High Energy Hadron Physics*, John Wiley & Sons, New York, 1974.
- [25] The LEP Injector Study Group, LEP design report, Vol. I, CERN LEP-TH/83-29 (1983).
- [26] The LEP Study Group, LEP design report, Vol. II, CERN LEP-TH/84-01 (1984).
- [27] W. Kalbreier, *et al.*, CERN-SL-92-33-DI-C, July 1992;  
*Int. J. Mod. Phys. A, Proc. Suppl.* 2A (1993) 401.
- [28] OPAL Collaboration, K. Ahmet, *et al.*, *Nucl. Inst. and Meth.* **A305** (1991) 275.

- [29] J.R. Carter, *et al.*, Nucl. Inst. and Meth. **A286** (1990) 99.
- [30] H.M. Fischer, *et al.*, Nucl. Inst. and Meth. **A283** (1989) 492.
- [31] H. Mes, *et al.*, Nucl. Inst. and Meth. **A265** (1988) 445.
- [32] O. Biebel, *et al.*, Nucl. Inst. and Meth. **A323** (1992) 169.
- [33] A. Ji-Gang, *et al.*, Nucl. Inst. and Meth. **A267** (1988) 386,  
A. Ji-Gang, *et al.*, Nucl. Inst. and Meth. **A267** (1988) 396.
- [34] M. Sasaki, Ph. D. thesis, UT-ICEPP-91-08 (December, 1991).
- [35] S. Kluth and D.R. Ward, Private Communication.
- [36] OPAL Collaboration, M. Arignon, *et al.*, Nucl. Inst. and Meth. **A313** (1992) 103.
- [37] OPAL Collaboration, P. Acton, *et al.*, Z. Phys. **C58** (1993) 219.
- [38] OPAL Collaboration, R. Akers, *et al.*, Z. Phys. **C61** (1994) 19.
- [39] S. Jadach, B.F.L. Ward, Z. Wąs, Comp. Phys. Comm. **66** (1991) 276.
- [40] T. Sjöstrand, Comp. Phys. Comm. **39** (1986) 347;  
M. Bengtsson and T. Sjöstrand, Comp. Phys. Comm. **43** (1987) 367;  
M. Bengtsson and T. Sjöstrand, Nucl. Phys. **B289** (1987) 810.
- [41] M. Böhm, A. Denner, and W. Hollik, Nucl. Phys. **B304** (1988) 687;  
F.A. Berends, R. Kleiss, and W. Hollik, Nucl. Phys. **B304** (1988) 712.
- [42] R. Battacharya, J. Smith, and G. Grammer, Phys. Rev. **D15** (1977) 3267;  
J. Smith, J.A.M. Vermaseren, and G. Grammer, Phys. Rev. **D15** (1977) 3280.
- [43] J. Allison, *et al.*, Nucl. Inst. and Meth. **A317** (1992) 47.
- [44] R. Brun, F. Bruyant, M. Maire, A.C. McPherson, and P. Zancarini, *GEANT3*, CERN-DD/EE/84-1 (1987).

- [45] S. Jadach, J.H. Kühn, Z. Wąs, *Comp. Phys. Comm.* **64** (1991) 275.
- [46] S. Jadach and B.F.I. Ward, *Comp. Phys. Comm.* **56** (1990) 351.
- [47] E. Barberio, B. van Eijk, and Z. Wąs, *Comp. Phys. Comm.* **66** (1991) 115.
- [48] D. Yu. Bardin, *et al.*, *Comp. Phys. Comm.* **59** (1990) 303.
- [49] CLEO Collaboration, M. Procaro, *et al.*, *Phys. Rev. Lett.* **70** (1993) 1207.
- [50] Particle Data Group, K. Hikasa, *et al.*, *Phys. Rev.* **D45** (1992) 1.
- [51] OPAL Collaboration, R. Akers, *et al.*, *Phys. Lett.* **B328** (1994) 207.
- [52] OPAL Collaboration, G. Alexander, *et al.*, *Phys. Lett.* **B266** (1991) 201.
- [53] OPAL Collaboration, P. Acton, *et al.*, *Phys. Lett.* **B288** (1992) 373.
- [54] OPAL Collaboration, P. Acton, *et al.*, *Z. Phys.* **C53** (1992) 539.
- [55] OPAL Collaboration, G. Alexander, *et al.*, *Z. Phys.* **C52** (1991) 175.
- [56] S. Jadach, B.F.L. Ward, Z. Wąs, *Comp. Phys. Comm.* **79** (1994) 503.
- [57] F. James, M. Roos, *Comp. Phys. Comm.* **10** (1975) 343.
- [58] R.J. Sobie, Private communication.
- [59] G. Bella, Private communication.
- [60] J. M. Roney, Private communication.
- [61] E. Barberio, B. van Eijk, and Z. Wąs, *Comp. Phys. Comm.* **66** (1991) 115.
- [62] ALEPH Collaboration, D. Buskulic, *et al.*, *Z. Phys.* **C59** (1993) 369.
- [63] DELPHI Collaboration, P. Abreu, *et al.*, *Z. Phys.* **C55** (1992) 555.
- [64] L3 Collaboration, M. Acciarri, *et al.*, *Phys. Lett.* **B341** (1994) 245.

- [65] OPAL Collaboration, R. Akers, *et al.*, CERN-PPE/94-120.
- [66] ALEPH Collaboration, D. Buskulic, *et al.*, *Z. Phys.* **C62** (1994) 539.
- [67] DELPHI Collaboration, P. Abreu, *et al.*, *Nucl. Phys.* **B418** (1994) 403.
- [68] L3 Collaboration, M. Acciarri, *et al.*, *Z. Phys.* **C62** (1994) 551.
- [69] OPAL Collaboration, R. Akers, *et al.*, *Z. Phys.* **C61** (1994) 19.
- [70] ALEPH Collaboration, D. Decamp, *et al.*, *Phys. Lett.* **B259** (1991) 377.
- [71] DELPHI Collaboration, P. Abreu, *et al.*, *Phys. Lett.* **B277** (1992) 371.
- [72] OPAL Collaboration, P.D. Acton, *et al.*, *Phys. Lett.* **B294** (1992) 436.
- [73] ALEPH Collaboration, D. Buskulic, *et al.*, *Z. Phys.* **C62** (1994) 179.
- [74] ALEPH Collaboration, D. Buskulic, *et al.*, *Phys. Lett.* **B335** (1994) 99.
- [75] ALEPH Collaboration, D. Buskulic, *et al.*, *Z. Phys.* **C62** (1994) 1.
- [76] DELPHI Collaboration, P. Abreu, *et al.*, CERN-PPE/94-161,
- [77] DELPHI Collaboration, P. Abreu, *et al.*, CERN-PPE/94-193,
- [78] L3 Collaboration, M. Acciarri, *et al.*, *Phys. Lett.* **B335** (1994) 542.
- [79] OPAL Collaboration, R. Akers, *et al.*, *Z. Phys.* **C60** (1993) 601.
- [80] DELPHI Collaboration, P. Abreu, *et al.*, CERN-PPE/94-219.
- [81] SLD Collaboration, K. Abe, *et al.*, *Phys. Rev. Lett.* **73** (1994) 25.
- [82] J.M. Roney, Private communication.
- [83] CLEO Collaboration, M. Artuso, *et al.*, *Phys. Rev. Lett.* **69** (1992) 3278.
- [84] CLEO Collaboration, P. Baringer, *et al.*, *Phys. Rev. Lett.* **59** (1987) 1993.

- [85] ARGUS Collaboration, H. Albrecht, *et al.*, *Z. Phys.* **C41** (1988) 405.
- [86] CLEO Collaboration, M. Artuso, *et al.*, *Phys. Rev. Lett.* **72** (1994) 3762.
- [87] ARGUS Collaboration, H. Albrecht, *et al.*, *Z. Phys.* **C56** (1992) 339.
- [88] DELPHI Collaboration, P. Abreu, *et al.*, *Z. Phys.* **C55** (1992) 555.
- [89] ALEPH Collaboration, D. Decamp, *et al.*, *Z. Phys.* **C54** (1992) 211.
- [90] Crystal Ball Collaboration, D. Antreasyan, *et al.*, *Phys. Lett.* **259** (1991) 216.
- [91] CELLO Collaboration, H.J. Behrend, *et al.*, *Z. Phys.* **C46** (1990) 537.
- [92] Mark III Collaboration, J. Adler, *et al.*, *Phys. Rev. Lett.* **59** (1987) 1527.
- [93] Mark II Collaboration, J.M. Yelton, *et al.*, *Phys. Rev. Lett.* **56** (1986) 812.
- [94] CELLO Collaboration, H.J. Behrend, *et al.*, *Z. Phys.* **C23** (1984) 103.



## PARTIAL COPYRIGHT LICENSE

I hereby grant the right to lend my dissertation to users of the University of Victoria Library, and to make single copies only for such users or in response to a request from the Library of any other university, or similar institution, on its behalf or for one of its users. I further agree that permission for extensive copying of this thesis for scholarly purposes may be granted by me or a member of the University designated by me. It is understood that copying or publication of this thesis for financial gain shall not be allowed without my written permission.

Title of Dissertation:

Measurement of the Neutral Current in the Standard Model Using the Tau Polarization Asymmetries Determined from the Decay  $\tau^- \rightarrow \rho^- \nu_\tau$

Author: \_\_\_\_\_  
MYRON R. ROSVICK  
July 19, 1995